UNIVERSITY OF LEEDS

# Designing Patient Specific Magnetically Actuated Tentacle Robots for Minimally Invasive Surgery

Peter Lloyd

Submitted in accordance with the requirements for the
degree of Doctorate of Philosophy in Robotics

The University of Leeds

Faculty of Engineering

School of Electronic and Electrical Engineering

December 2022

# Abstract

Currently, we are limited in the tools available to reach deep inside the human body in a non-invasive manner, patients therefore may not have the option to be assessed or treated for life-threatening diseases. The long-term vision of this work is to provide surgeons with the capability to administer care with the aid of soft magnetic manipulators. The operator, needing minimally invasive access to a specific site via a complex winding pathway will be able to design personalized manipulators and fabricate them on demand. Magnetic control will allow the manipulators to be extremely soft and thin. Controlling the position of multiple anchor points along the length of the manipulator will allow shape forming for tortuous curvilinear trajectories without exerting significant pressure on surrounding tissues. Full-body control will also provide the ability to stiffen part of the manipulator to accomplish specific surgical tasks that need structural rigidity.

In this thesis, this vision has been taken and soft, shape forming, magnetic manipulators have been developed. Novel modeling, simulation, optimization and fabrication techniques have been established as well as the introduction and demonstration of the concept of material reinforcement for magnetic actuation. Tentacles down to 2 mm diameter have been produced which are currently capable of semi-autonomous, low contact navigation into tortuous, soft phantoms of the digestive and respiratory anatomy - areas of the body which cannot easily be accessed using traditional minimally invasive methods.

Whilst there remain many developments to be made, significant and meaningful progress has been demonstrated here on the journey towards autonomous follow-the-leader navigation. It is hoped that this work and any which develop onwards from it will continue to enable miniaturized magnetic endoluminal navigation and thus contribute to the continued progress of medical diagnostics and treatment.

# Acknowledgments

I would like to thank Pietro for taking a chance and offering me an unlikely opportunity. I would like to think it paid off. Thanks also to James, Giovanni, Ali and Onaizah for their experience, to Tomas and Zaneta for their collaborations, to the whole STORM lab in one way or another. Thanks also to my mum for doing the proofreading and making the cups of tea.

This thesis is dedicated to my dad who would probably have been the only person to read it “properly”.

# Contents

# Chapter 1

# Introduction

The work presented in this thesis is a subset of the past four years' of a larger team effort, developing soft continuum manipulator technology. The high level objective of both the wider project, supported by the European Research Council, and of this thesis specifically, is to develop materially soft, lengthwise shape forming, magnetically actuated surgical catheters, henceforth referred to as "tentacles". The motives for this being to reduce patient trauma, both pain and damage, and to access currently inoperable regions of the human anatomy during follow-the-leader navigations for minimally invasive surgical procedures.

Current, manual, catheterization technology entails a physically skilled task with human error and training time to be considered [1] [2]. Automation of this process can reduce this human reliance but most automated catheters still rely on anatomical interaction forces to shape form during navigation [3]. In order that we achieve our first stated objective of trauma reduction we look towards follow-the-leader motion. Here a catheter would shape-form to assume the profile of the anatomy through which it navigates without relying on contact forces. The historic drawback with this approach is the inverse relationship between dexterity and manipulator diameter [4]. Any attempt to incorporate multi-point control will inevitably add some form of energy transfer connections (e.g. wires or pipes) and thus increase manipulator diameter. The exception being magnetic actuation with its characteristic force at a distance [5]. Offboard power supply associated with magnetic actuation, coupled with material softness, also enables the second of our stated objectives, namely to reach currently inaccessible locations in a minimally invasive manner. These locations may be inaccessible due to tissue sensitivity and path tortuousness such as in the brain vasculature, due to size restrictions as we see in the extremities of the bronchial tree or, in some cases all of the above, such as in the pancreas. Fig. 1.1 illustrates the immediate, visible consequence of the absence of follow-the-leader catheterization in a cardiac navigation.

Based on the above, the three key behaviors any tentacle design must therefore display are (a) material softness, (b) length-wise shape forming capability and, (c) miniaturizability. These can be expanded upon as follows.

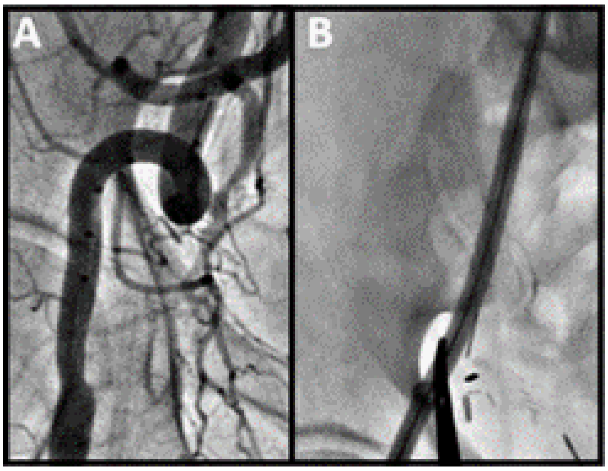

Figure 1.1: An example of a catheter flexibility problem for a cardiovascular intervention: (A) Tortuosity of the relaxed external iliac artery. (B) Straightening under catheterization [10].

Material softness is a difficult and slightly ambiguous concept with various definitions existing dependent on application and scientific specialism. On a purely practical level, some threshold maximum elastic modulus could be defined (10 MPa in [6]), alternatively the requirement for an amorphous atomic structure resulting in non-linear elastic behaviour offers a more fundamental description [7]. The following definition from [8] gives a useful and relevant baseline: “Matter which undergoes deformations of similar or greater magnitude than the deformation of its environment”. In the case of surgical robotics the biological matter through which we will pass is likely to range from around 100 Pa in the softest areas of the brain up to around 100,000 Pa for cartilage [9]. These bulk material elasticities are comparable to the silicone based elastomers with which we habitually fabricate. The important point here is that Nitinol, Steel and NdFeB with elastic moduli in the gigapascal range can be arranged in a manner which is *flexible* but can never be considered *soft* in comparison to biological tissue.

Length-wise shape forming represents probably the most significant separation between this project and other soft magnetic manipulator (SMM) studies where actuation is typically focused at the tip, such as [11] [12] [13] [14] [15]. Exploiting the capability of tentacles to exhibit a continuous or multi-point and non-uniform magnetization profile along their lengths, thus generating spatially resolved deformations [16], we can theoretically produce contact free navigation. Whilst there have been recent developments in the state of the art towards multi-point magnetic control [17] our group has been the first to demonstrate length-wise shape forming SMMs capable of minimal contact, follow-the-leader motion [18] [3].

The nature of magnetic actuation permits almost unlimited miniaturization. As the fundamental electro-magnetic force (the Lorentz force) operates at range and through living tissue, actuation is performed off-board and a permanent magnet can be encoded with some level of intelligence with no need for cables, pipes, valves etc. The recent proliferation of untethered sub-millimetre scale magnetic devices evidences this point abundantly [19] [20] but in the case of the continuum manipulator we employ a tether to functionalize the tool [21] [22]. As such the lower limit of miniaturization is imposed by functional purpose as opposed to actuation technique.

In summary, the ambition was (and remains) to design tentacles which can reach deeper into the body, and which cause less patient trauma than is currently possible. The approach to this problem is to use soft materials and length-wise shape forming to enable low contact, follow-the-leader motion, both of these features will reduce tissue trauma. Furthermore, we use magnetic actuation in order that our designs will be as miniaturizeable as possible. This being a very innovative topic, allowed me the chance to publish several papers in the course of my PhD, as such this is a thesis by publication, the main body (Chapters 2 - 6) are reformatted but otherwise verbatim reproductions of the four published contributions - three journal papers and a conference paper (Chapter 3), and one further journal paper still under review as of December 2022 (Chapter 6).

The contributions of this PhD thesis are as follows:

Chapter 2, The First Shape Forming Magnetic Catheter [23] - where I introduced the concept of the magnetic tentacle, this was the first appearance of a catheter-like shape fabricated from magnetically hard elastomeric material as well as the first use of a neural network to invert the force balance of a soft robot model.

Chapter 3, A Follow-the-Leader Shape Forming Algorithm [24] - where I develop an algorithm which balances magnetic torque against elastic torque in a rigid link model across four insertion time steps. Using this solution, in a simulated environment, I demonstrate follow-the-leader navigation under magnetic actuation for the first time.

Chapters 4 and 5, Actuation Instability and Material Reinforcement [25] [18] - where I identify the twisting instability unique to non-axially magnetized catheters. In these two papers I offer different solutions to this newly identified problem, the first embedding helical fibre reinforcing and the second embedding commercial braiding. The relative merits of these alternative methods are discussed and ultimately a successful follow-the-leader navigation into a soft phantom of the pancreatic duct is demonstrated.

Chapter 6 presents a jointly first authored paper [26], under review as of December 2022, in which miniaturizable functionalization is demonstrated. An initial feasibility study of leveraging variable stiffness in order to grasp and release objects under closed loop control is presented.

The low contact navigation shown in Chapter 5 demonstrates the culmination of the previous work thus creating a narrative arc through the thesis. With these contributions to my PhD thesis as well as a feasibility demonstration of functionalization we are well positioned to embark on a wide array of future research directions as detailed in Chapter 7.

## 1.1 The First Shape Forming Magnetic Catheter

The history of magnetically assisted medical procedures starts hundreds of years ago but with very specific and limited applications such as the removal of ferrous shrapnel from an eyeball [27]. The first example of a guided magnetic catheter appears in 1951 [28] then, nearly six decades later, the magnetically steered catheter was successfully commercialized, first by Stereotaxis [29], shortly followed by Magnatecs [30]. Up to this point the materials involved were flexible but hard and the catheters were exclusively tip driven. These two features are significant as reducing the diameter of a steel wire will allow abundant flexibility but, under tip driven actuation, also increase the likelihood of a corner cutting tear or “cheese-wiring” which in, for example, a neurological intervention could be catastrophic [31].

Magnetically hard material is defined as that which allows retention of residual magnetic flux density after the removal of a saturating magnetic field [33]. In 2014 the first mechanically soft, magnetically hard materials entered robotics [32]. This technology is yet to penetrate into the commercial world but has had a profound influence within the soft robotics research community. The novel concept of a continuously magnetizable, elastomerically soft material permits a huge range of opportunities for embedded material intelligence at a miniaturizable scale as demonstrated by a number of high-profile research groups [16], [33], [34]. It also poses some serious challenges to the simulation and modeling community but we will return to this tangential point in due course. Amongst this ongoing flurry of innovation around magnetic elastomers, in 2016 we saw a length-wise shape forming cilia-like sheet [16], in 2019 a sub-millimeter scale magnetically tip driven guide-wire [13] (Fig. 1.2) and then in 2020, I introduced the first demonstration of this hard magnetic soft matter for a length-wise shape forming catheter-like shape [23].

The difference in terms of modeling, optimization and simulation between soft and hard robotics is vast. The infinite degrees of freedom of elastomeric continua is far more complex to capture in a usable manner than the rigid link behavior of hard robotics [35]. The major consequence of this being that hard robotic kinematics and kinetics has been largely encoded [36] whilst soft robotics modeling is still limited to making aggressive approximations on basic geometries, amongst which is the continuum manipulator.

In order for any soft robotic model to be useful it must be invertible. In hard robotics rigid body kinematics is inverted to derive control algorithms based on desired poses. In soft robotics the concept of kinematics is meaningless as deformation is always a function of force, so I instead refer to considerations of “statics” and “inverse-statics” where force is balanced with pose/deformation.

There are, of course many options of soft robot model available with trade-offs between accuracy and processing time being the usual consideration [1]. For our first publication on tentacles I opted for accuracy of physical representation by implementing a high def-

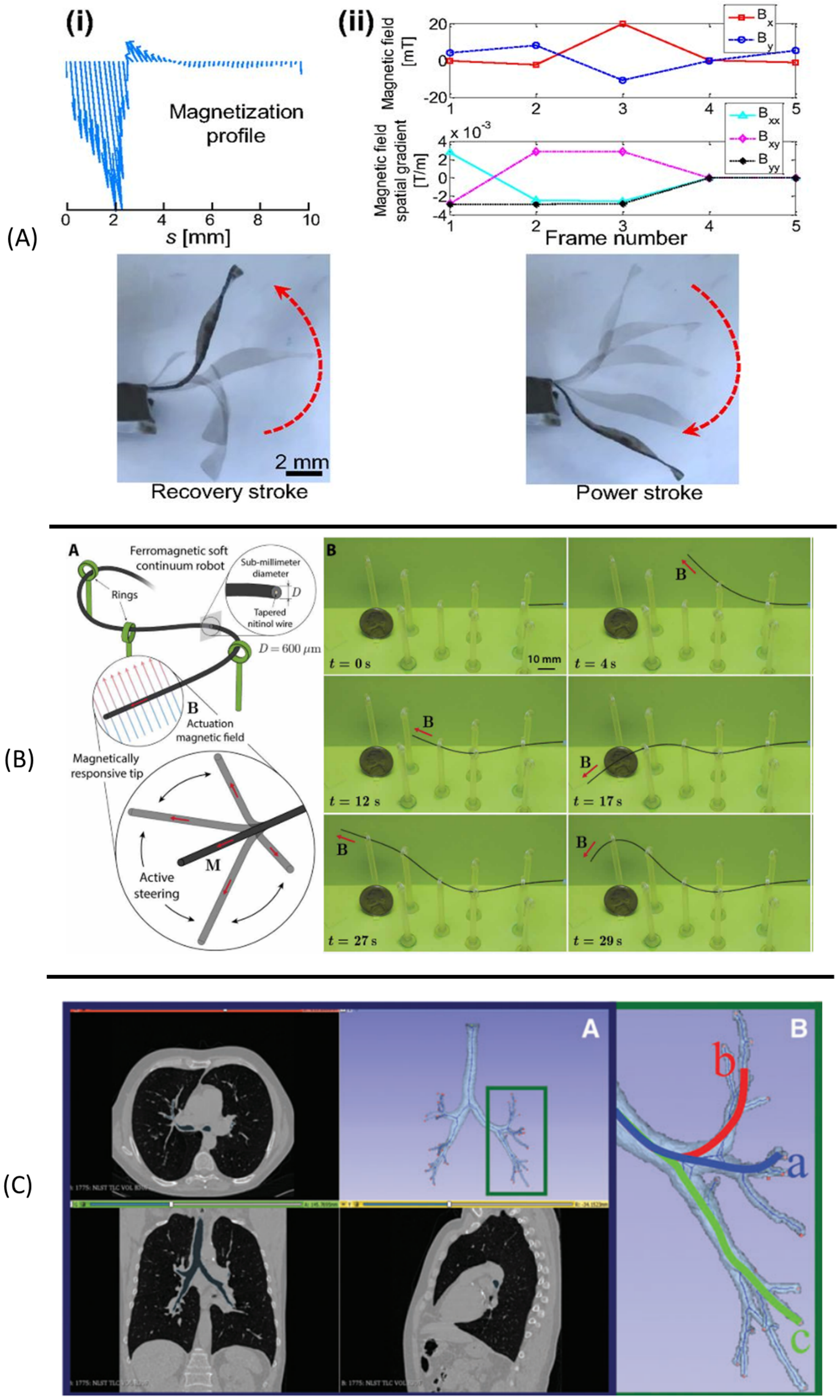

Figure 1.2: Snapshots of the progress of the state of the art. (A) In 2016, an early example of a magnetically hard, materially soft robot - A tethered cilium showing length-wise magnetization signature and full body shape forming [32]. (B) In 2019, the sub-millimetre, soft magnetic tip driven catheter of [13]. (C) In 2022, the STORM lab demonstrated a follow-the-leader navigating length-wise shape forming soft catheter for bronchoscopy [3].

inition continuum mechanics model via commercial Finite Element Modeling. Inspired by non-robotics examples [37] [38], I inverted the statics of this model using an artificial neural network. I produced thousands of simulations to explore the search space and then learnt the relationship between controllable inputs and deformation outputs. With this system I produced three successful prototypes of lengthwise shape forming tentacles as relayed in Chapter 2. I did not however approach the broader challenge of navigating forward through space and therefore demonstrating minimal contact, follow-the-leader motion.

As would become subsequently apparent, this brute-force approach, whilst capable of accommodating the limited search space requirements of a non-navigating tentacle, ran into difficulties associated with computational capacity when it was applied to a multiple time step navigation. Subsequent modeling approaches employed far more aggressive approximations in order that the soft robot statics could be inverted in a computationally feasible manner. From this work, however, I did develop an encouragingly accurate Finite Element Simulation of the notoriously difficult hyper-elastic magnetic domain which went on to be implemented in a number of other studies [39] [40].

## 1.2 A Follow-the-Leader Shape Forming Algorithm

As previously mentioned, the principle degree of separation between the state of the art in 2019 and this project was the lengthwise shape forming component. The ambition was always to develop a tentacle which could pass through tortuous pathways in such a manner as to minimize anatomical contact during transit, a challenge which was addressed for the first time in 2020 [24]. This can only be achieved by applying a non-uniform lengthwise magnetization signature (as demonstrated in [16]) and an actuating field which varies as the tentacle length is augmented during navigation (as in [33]). In order to achieve this ambitious goal I had to derive an algorithm which could simultaneously optimize these two continuous variables. To constrain this infinite search space it was obviously necessary to make physical simplifications and also to apply some degree of discretization.

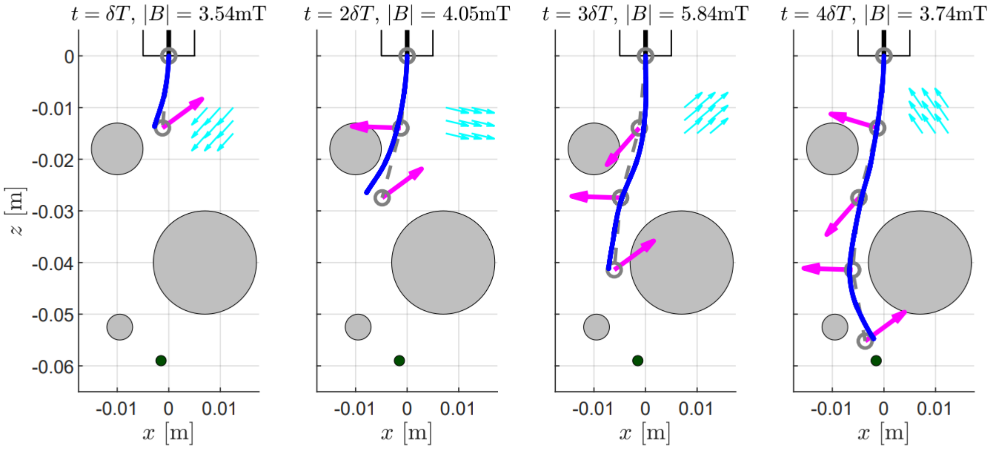

Figure 1.3: The contact free planar navigation adapted from [24]. A rigid link model balances interactions between local magnetization vectors (purple arrows) and actuating fields (turquoise arrows) with internal elastic torques. These vary over four insertion time steps to avoid arbitrary obstacles (in gray) en route to a target location (in dark green).

Inspired by [41] and detailed in Chapter 3, I separated the tentacle into four pseudo-rigid links, each link with an independent magnetization direction. I also separated the transient problem into four pseudo-static time steps with one link inserted at each time step.

I encoded the magnetic torque at each pseudo-link as a function of these unknown magnetizations and actuating fields as in [42]. I calculated elastic torques at each pseudo-joint from a beam bending model as in [41]. I then built a statics model aggregating these magnetic and mechanical torques via a robot Jacobian. Finally, by mapping arbitrary pathways into arrays of desired pseudo-joint angles I built an error function which could be minimized. This balanced desired joint angles from the path planner to the calculated joint angles generated by any given magnetizations and fields. This error function was therefore a 16 dimensional function of the magnetization profile (2D space × 4 links) and the actuating fields (2D space × 4 time steps) and could be solved efficiently using gradient descent optimization or a genetic algorithm in Matlab.

This excessive detail in an introduction is justified on the grounds that this particular publication ([24]) represents a critical contribution towards the overall project. Due to an absence of experimental validation it only appeared as a conference paper - the previously mentioned finite element simulation was considered ground truth. It went on however, two years later, to form the optimization basis for two, more significant experimental publications [3] [18] and, as of late 2022, is still in regular use within our lab. At the time of publication of this conference paper the assumption was that an experimental journal paper would soon follow. There was however a significant and unexpected issue to be addressed before any real world results could be successfully recorded which is detailed next.

## 1.3 Actuation Instability and Material Reinforcement

The four time-step follow-the-leader navigation presented at the International Symposium on Medical Robotics (ISMR) in 2020 [24] made the critical assumption that magnetization and actuation occurred on a plane within which all joint angles existed. The outcome of the calculation which determined optimal magnetization vectors and actuating fields was constrained to this plane. Under this assumption (described in detail in Chapter 3), if the actuating field was pointed towards a magnetization vector - creating an instability - large bending deformation would occur. Critically, what the planar assumption misses is that, in three-dimensional space, this mode of actuation will seek the lowest energy deformation. This energy minima is found by twisting around the long axis and bending significantly less (Fig. 1.4). Furthermore, as twisting occurs, the deformed magnetization vector becomes increasingly out of plane and the cross product calculation results in *greater* twisting torque - a classic inverted pendulum instability.

This unexpected issue became immediately apparent when experiments were conducted to try and reconcile the work in [24]. In practice, and for relatively small deformations (less than 100°), the optimization algorithm can be constrained to avoid these actuating instabilities. This is exactly the system employed in [3] but in order to generate large deformations it was apparent that some kind of physical constraint (material or geometric) would need embedding within the design. It is worth remembering that deformations of many hundreds of degrees are commonplace and easily controlled in certain designs of

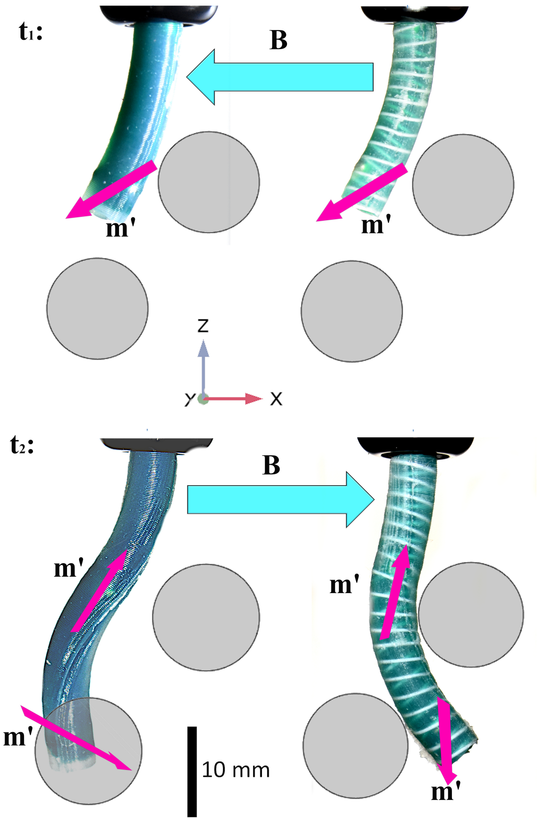

Figure 1.4: ($t_1$) Stable actuation. The flexible fibres have little adverse impact on deformation. ($t_2$ - Left) The unreinforced tentacle twists about its long "easy" axis when actuated in such a direction as to induce the inverted pendulum instability. ($t_2$ - Right) This twist is dramatically reduced using helical fibre reinforcing.

pneumatic soft robot. This limitation therefore represents a significant challenge for the feasibility in certain scenarios of magnetic actuation.

The first attempt to overcome this challenge involved the embedding of extremely thin, flexible but effectively inextensible, nylon fibres in a double helix arrangement along the length of the tentacle (Fig. 1.4) [25]. This also represented the first ever example of materially reinforced magnetic actuation. Inspired by fibre reinforcing works in pneumatic actuation (such as [43]) I built an FEM driven optimization to vary the characteristic parameters of the reinforcing. This was experimentally verified with great success in a single segment (20 mm long × 6 mm diameter) tentacle and with some success in a two segment tentacle (40 mm long × 6 mm diameter). The emerging problem with this design related to aspect ratio - the ratio of length over diameter of the tentacle. The loss of actuating torque in the bending plane is experienced when the tip of the tentacle rotates about the local z axis by more than some small angle (this is a continuous function but consequential losses occur above around 20°). A design which constrains the twist to 10° in a 20 mm tentacle will allow at least 20° of twisting in an otherwise similar 40 mm tentacle and so forth. As such it became apparent that I needed a system which constrained twisting far more aggressively than the design offered in [25]. The next development therefore, was to embed a braid into the tentacle.

Thus followed considerable searching of the private market-place to find braids appropriate for the extremely low torques imparted by the tentacle. Any braid must be sufficiently narrow and flexible to be useful at our scale and torque range, but also sufficiently torsionally rigid to successfully constrain the tentacle. This latter requirement unfortunately eliminated braided fishing line which enjoys a well developed manufacturing process in a huge range of clinically relevant sizes. The smallest commercially available braid is designed for lightweight blind cords and has an external diameter of 1 mm.

The final publication featured in this thesis demonstrates the efficacy of embedding a 1 mm diameter braid into a 2 mm diameter × 50 mm long tentacle [18]. The braided tentacle shows large deformations in a clinically relevant environment - navigating in an atraumatic manner into mechanically realistic phantoms of the bile and pancreatic ducts. I also demonstrate how these large deformation, low contact force navigations are unachievable without both the optimized magnetization profile ([24]) and the embedded braid. Furthermore, there are indications from ongoing work within our lab that this twisting effect is occurring in *axially* magnetized unreinforced tentacles when deformation is sufficiently large (approaching and even exceeding 180°). It is therefore my belief that in the near future, the idea of producing a tentacle without at least some form of material reinforcing will become outdated.

Fibre reinforcing offers a system of design and fabrication which can be optimized and manipulated in a way that embedded braiding currently can not be. The parameters of the fibre reinforcing can be varied according to the specific requirements of the tentacle. The braid however offers a level of torsional rigidity that we haven't managed to achieve

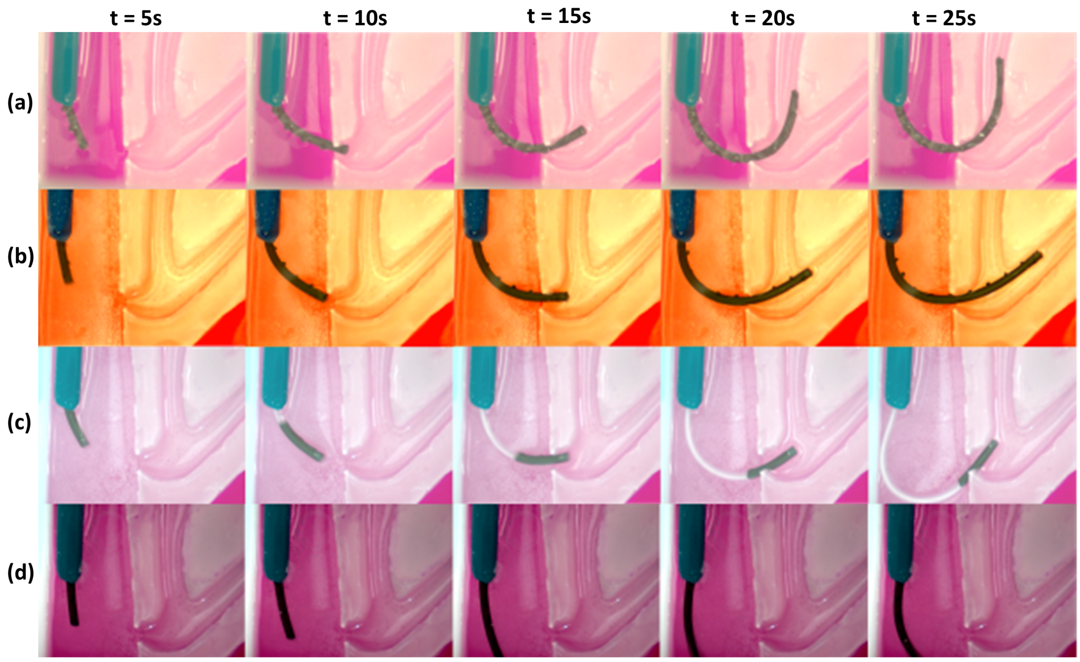

Figure 1.5: The efficacy of a length-wise magnetized, braid reinforced tentacle [18]. (A) Navigation from the main digestive tract into the bile duct. (B) Navigation into the pancreatic duct. (C) A tip driven magnetic catheter unsuccessfully attempting to navigate into the pancreatic duct. (D) A length-wise magnetized but unreinforced tentacle unsuccessfully attempting to navigate into the pancreatic duct.

with fibre reinforcing. There is therefore abundant potential for an extension study into closing this gap via fabrication technology. Either developing the helical winding system such that it produces ever greater torsional rigidity, or developing a braid fabrication system that can be miniaturized and characteristically manipulated according to system requirements, or both.

## 1.4 Variable Stiffness for Coiling

The majority of the work presented in this thesis pertains purely to considerations of navigation. In order to fulfill the original vision of providing the capability to *administer* care, the tentacle must be functionalized. As discussed in Chapter 7, this functionalization could take on many forms however, in Chapter 6 I show the tentacle performing the role of grasping and releasing an arbitrary cargo [26]. This is demonstrated with a high deformation coiling action induced by the combination of a rotating applied field synchronized with a sliding nitinol backbone. As the applied magnetic field rotates with respect to time, the sliding nitinol backbone is withdrawn. The spatially rotating magnetization of the tentacle is optimized such that, as regions lose the stiffening effect of the sliding backbone, they deform into a coiled shape. This high deformation pose represents a higher energy state than would be achievable without synchronized actuation. In order for magnetic coiling to be successfully demonstrated the tentacle was also, for the first time, visually tracked and controlled in closed-loop.

Whilst this is purely a proof of concept publication, the variable stiffness grasping robot has potential as a surgical tool for applications in cargo delivery and retrieval. Furthermore, this represents the first step of the next stage of the tentacle project in which practical applications can be explored and tested and the tentacle can move towards a clinically useful entity.

## 1.5 Summary and Contributions

To summarize, I first introduced the concept of the shape forming soft magnetic catheter. This design was simulated in a finite element model, inverted using a neural network then three samples were manufactured and tested statically in a one dimensional Helmholtz coil [23]. This proved the viability of the length-wise magnetized tentacle concept and also the legitimacy of both a magnetic-hyperelastic Finite Element Model and an artificial neural network as a system for inverting the solution.

Second, I developed an optimization algorithm based on a magnetic rigid link model which could invert to find a solution over four discrete time-steps. This allowed me to demonstrate contact free navigation of the tentacles in a simulated planar environment [24].

Third, I identified a key instability inherent in non-axially aligned magnetic actuation - the twisting instability - and presented a feasible solution to this problem. In fact this solution was the first example of a fibre reinforced magnetic soft robot.

Fourth, I developed and expanded the concept of fibre reinforcing into embedded braid reinforcing and successfully leveraged this technology to demonstrate a low contact navigation into a soft phantom of both bile and pancreatic ducts.

Fifth and finally, I demonstrated a coiling tentacle which exploits variable stiffness and a rotating applied field under closed loop control to achieve large ($>400°$) deformations to grasp and release objects. This represents the starting point of the functionalization stage of the project.

### List of Publications

The present thesis contains material from the following first authored and (*) joint first authored publications:

- **P. Lloyd**, A. K. Hoshiar, T. da Veiga, A. Attanasio, N. Marahrens, J. H. Chandler, and P. Valdastri, "A learnt approach for the design of magnetically actuated shape forming soft tentacle robots," IEEE Robotics and Automation Letters, vol. 5, no. 3, pp. 3937–3944, 2020.

- **P. Lloyd**, G. Pittiglio, J. H. Chandler, and P. Valdastri, "Optimal design of soft continuum magnetic robots under follow-the-leader shape forming actuation," 2020 International Symposium on Medical Robotics (ISMR), 2020, pp. 111–117.

- **P. Lloyd**, Z. Koszowska, M. Di Lecce, O. Onaizah, J. H. Chandler, and P. Valdastri, "Feasibility of fiber reinforcement within magnetically actuated soft continuum robots," Frontiers in Robotics and AI, vol. 8, 2021.

- **P. Lloyd**, O. Onaizah, G. Pittiglio, D. K. Vithanage, J. H. Chandler, and P. Valdastri, "Magnetic soft continuum robots with braided reinforcement," IEEE Robotics and Automation Letters, vol. 7, no. 4, pp.9770–9777, 2022.

- **P. Lloyd***, T. L. Thomas*, V. K. Venkiteswaran, G. Pittiglio, J. H. Chandler, P. Valdastri, and S. Misra, "A magnetically-actuated coiling soft robot with variable stiffness," IEEE Robotics and Automation Letters, under review - submitted October 2022.

The following non first authored papers have also contributed to the work presented:

- G. Pittiglio, **P. Lloyd**, T. da Veiga, O. Onaizah, C. Pompili, J. Chandler, and P. Valdastri, "Patient-specific magnetic catheters for atraumatic autonomous endoscopy," Soft Robotics, 2022.

- T. da Veiga, J. H. Chandler, **P. Lloyd**, G. Pittiglio, N. J. Wilkinson, A. K. Hoshiar, R. A. Harris, and P. Valdastri, "Challenges of continuum robots in clinical context: a review," Progress in Biomedical Engineering, vol. 2, no. 3, p. 032003, aug 2020.

- M. Di Lecce, O. Onaizah, **P. Lloyd**, J. Chandler, and P. Valdastri, "Evolutionary inverse material identification: Bespoke characterization of soft materials using a metaheuristic algorithm," Front Robot AI., no.14;8:790571, Jan 2022.

- T. Da Veiga, J. H. Chandler, G. Pittiglio, **P. Lloyd**, M. Holdar, O. Onaizah, A. Alazmani, and P. Valdastri, "Material characterization for magnetic soft robots," in 2021 IEEE 4th International Conference on Soft Robotics (RoboSoft), 2021, pp. 335–342.

# Bibliography

[1] T. da Veiga, J. H. Chandler, P. Lloyd, G. Pittiglio, N. J. Wilkinson, A. K. Hoshiar, R. A. Harris, and P. Valdastri, "Challenges of continuum robots in clinical context: a review," *Progress in Biomedical Engineering*, vol. 2, no. 3, p. 032003, aug 2020.

[2] C. Heunis, J. Sikorski, and S. Misra, "Flexible Instruments for Endovascular Interventions: Improved Magnetic Steering, Actuation, and Image-Guided Surgical Instruments," *IEEE Robotics and Automation Magazine*, vol. 25, no. 3, pp. 71–82, 2018.

[3] G. Pittiglio, P. Lloyd, T. da Veiga, O. Onaizah, C. Pompili, J. Chandler, and P. Valdastri, "Patient-specific magnetic catheters for atraumatic autonomous endoscopy," *Soft Robotics*, 2022.

[4] J. Burgner-Kahrs, D. C. Rucker, and H. Choset, "Continuum robots for medical

applications: A survey," *IEEE Transactions on Robotics*, vol. 31, no. 6, pp. 1261–1280, 2015.

[5] P. E. Dupont, B. J. Nelson, M. Goldfarb, B. Hannaford, A. Menciassi, M. K. O'Malley, N. Simaan, P. Valdastri, and G.-Z. Yang, "A decade retrospective of medical robotics research from 2010 to 2020," *Science Robotics*, vol. 6, no. 60, p. eabi8017, 2021. [Online]. Available: https://www.science.org/doi/abs/10.1126/scirobotics.abi8017

[6] C. Majidi, "Soft-matter engineering for soft robotics," *Advanced Materials Technologies*, vol. 4, no. 2, p. 1800477, 2019.

[7] P.-G. de Gennes, "Soft matter (nobel lecture)," *Angewandte Chemie International Edition in English*, vol. 31, no. 7, pp. 842–845, 1992.

[8] N. Kastor, V. Vikas, E. Cohen, and R. D. White, "A definition of soft materials for use in the design of robots." *Soft Robotics*, pp. 181–182, Sep 2017.

[9] I. Levental, P. C. Georges, and P. A. Janmey, "Soft biological materials and their impact on cell function," *Soft Matter*, vol. 3, pp. 299–306, 2007. [Online]. Available: http://dx.doi.org/10.1039/B610522J

[10] S. Toggweiler, J. Leipsic, R. K. Binder, M. Freeman, M. Barbanti, R. H. Heijmen, D. A. Wood, and J. G. Webb, "Management of vascular access in transcatheter aortic valve replacement," *JACC: Cardiovascular Interventions*, vol. 6, no. 8, pp. 767–776, 2013.

[11] J. Edelmann, A. J. Petruska, and B. J. Nelson, "Magnetic control of continuum devices," *The International Journal of Robotics Research*, vol. 36, no. 1, pp. 68–85, 2017.

[12] S. Jeon, A. K. Hoshiar, K. Kim, S. Lee, E. Kim, S. Lee, J.-y. Kim, B. J. Nelson, H.-J. Cha, B.-J. Yi, and H. Choi, "A Magnetically Controlled Soft Microrobot Steering a Guidewire in a Three-Dimensional Phantom Vascular

Network," *Soft Robotics*, vol. 6, no. 1, pp. 54–68, oct 2018. [Online]. Available: https://doi.org/10.1089/soro.2018.0019

[13] Y. Kim, G. A. Parada, S. Liu, and X. Zhao, "Ferromagnetic soft continuum robots," *Science Robotics*, vol. 4, no. 33, p. eaax7329, 2019.

[14] L. B. Kratchman, T. L. Bruns, J. J. Abbott, and R. J. Webster, "Guiding elastic rods with a robot-manipulated magnet for medical applications," *IEEE Transactions on Robotics*, vol. 33, no. 1, pp. 227–233, Feb 2017.

[15] C. M. Heunis, Y. P. Wotte, J. Sikorski, G. P. Furtado, and S. Misra, "The armm system-autonomous steering of magnetically-actuated catheters: Towards endovascular applications," *IEEE Robotics and automation letters*, vol. 5, no. 2, pp. 704–711, 2020.

[16] G. Z. Lum, Z. Ye, X. Dong, H. Marvi, O. Erin, W. Hu, and M. Sitti, "Shape-programmable magnetic soft matter," *Proceedings of the National Academy of Sciences*, vol. 113, no. 41, pp. E6007 LP – E6015, oct 2016. [Online]. Available: http://www.pnas.org/content/113/41/E6007.abstract

[17] M. Richter, V. K. Venkiteswaran, and S. Misra, "Multi-point orientation control of discretely-magnetized continuum manipulators," *IEEE Robotics and Automation Letters*, vol. 6, no. 2, pp. 3607–3614, 2021.

[18] P. Lloyd, O. Onaizah, G. Pittiglio, D. K. Vithanage, J. H. Chandler, and P. Valdastri, "Magnetic soft continuum robots with braided reinforcement," *IEEE Robotics and Automation Letters*, vol. 7, no. 4, pp. 9770–9777, 2022.

[19] T. Xu, J. Zhang, M. Salehizadeh, O. Onaizah, and E. Diller, "Millimeter-scale flexible robots with programmable three-dimensional magnetization and motions," *Science Robotics*, vol. 4, no. 29, p. eaav4494, 2019.

[20] C. Pawashe, S. Floyd, and M. Sitti, "Modeling and experimental characterization of an untethered magnetic micro-robot," *The International Journal of Robotics*

*Research*, vol. 28, no. 8, pp. 1077–1094, 2009. [Online]. Available: https://doi.org/10.1177/0278364909341413

[21] J. C. Norton, P. R. Slawinski, H. S. Lay, J. W. Martin, B. F. Cox, G. Cummins, M. P. Desmulliez, R. E. Clutton, K. L. Obstein, S. Cochran, and P. Valdastri, "Intelligent magnetic manipulation for gastrointestinal ultrasound," *Science Robotics*, vol. 4, no. 31, pp. 1–14, 2019.

[22] J. W. Martin, B. Scaglioni, J. C. Norton, V. Subramanian, A. Arezzo, K. L. Obstein, and P. Valdastri, "Enabling the future of colonoscopy with intelligent and autonomous magnetic manipulation," *Nature machine intelligence*, vol. 2, no. 10, pp. 595–606, 2020.

[23] P. Lloyd, A. K. Hoshiar, T. da Veiga, A. Attanasio, N. Marahrens, J. H. Chandler, and P. Valdastri, "A learnt approach for the design of magnetically actuated shape forming soft tentacle robots," *IEEE Robotics and Automation Letters*, vol. 5, no. 3, pp. 3937–3944, 2020.

[24] P. Lloyd, G. Pittiglio, J. H. Chandler, and P. Valdastri, "Optimal design of soft continuum magnetic robots under follow-the-leader shape forming actuation," in *2020 International Symposium on Medical Robotics (ISMR)*, 2020, pp. 111–117.

[25] P. Lloyd, Z. Koszowska, M. Di Lecce, O. Onaizah, J. H. Chandler, and P. Valdastri, "Feasibility of fiber reinforcement within magnetically actuated soft continuum robots," *Frontiers in Robotics and AI*, vol. 8, 2021. [Online]. Available: https://www.frontiersin.org/article/10.3389/frobt.2021.715662

[26] P. Lloyd, T. L. Thomas, V. K. Venkiteswaran, G. Pittiglio, J. H. Chandler, P. Valdastri, and S. Misra, "A magnetically-actuated coiling soft robot with variable stiffness," *IEEE Robotics and Automation Letters*, under review - submitted October 2022.

[27] B. J. Nelson, S. Gervasoni, P. W. Chiu, L. Zhang, and A. Zemmar, "Magnetically actuated medical robots: An in vivo perspective," *Proceedings of the IEEE*, 2022.

[28] H. Tillander, “Magnetic guidance of a catheter with articulated steel tip,” *Acta radiologica*, vol. 35, no. 1, pp. 62–64, 1951.

[29] F. Carpi and C. Pappone, “Stereotaxis niobe magnetic navigation system for endocardial catheter ablation and gastrointestinal capsule endoscopy,” *Expert review of medical devices*, vol. 6, no. 5, pp. 487–498, 2009.

[30] E. Gang, B. L. Nguyen, Y. Shachar, L. Farkas, L. Farkas, B. Marx, D. Johnson, M. Fishbein, C. Gaudio, and S. Kim, “Dynamically shaped magnetic fields initial animal validation of a new remote electrophysiology catheter guidance and control system,” *Circulation. Arrhythmia and electrophysiology*, vol. 4, pp. 770–7, 06 2011.

[31] Y. Chitalia, S. Jeong, J. Bok, V. Nguyen, S. Melkote, J. J. Chern, and J. P. Desai, “Towards the design and development of a pediatric neuroendoscope tool,” in *2019 IEEE/RSJ International Conference on Intelligent Robots and Systems (IROS)*, 2019, pp. 2998–3004.

[32] E. Diller, J. Zhuang, G. Zhan Lum, M. R. Edwards, and M. Sitti, “Continuously distributed magnetization profile for millimeter-scale elastomeric undulatory swimming,” *Applied Physics Letters*, vol. 104, no. 17, p. 174101, 2014.

[33] R. Zhao, Y. Kim, S. A. Chester, P. Sharma, and X. Zhao, “Mechanics of hard-magnetic soft materials,” *Journal of the Mechanics and Physics of Solids*, vol. 124, pp. 244–263, 2019. [Online]. Available: http://www.sciencedirect.com/science/article/pii/S0022509618307646

[34] V. K. Venkiteswaran, L. F. P. Samaniego, J. Sikorski, and S. Misra, “Bio-inspired terrestrial motion of magnetic soft millirobots,” *IEEE Robotics and Automation Letters*, vol. 4, no. 2, pp. 1753–1759, 2019.

[35] P. E. Dupont, N. Simaan, H. Choset, and C. Rucker, “Continuum robots for medical interventions,” *Proceedings of the IEEE*, vol. 110, no. 7, pp. 847–870, 2022.

[36] B. Siciliano, L. Sciavicco, L. Villani, and G. Oriolo, *Robotics: Modelling, Planning and Control.* Springer Publishing Company, Incorporated, 2010.

[37] M. Pfeiffer, C. Riediger, J. Weitz, and S. Speidel, "Learning soft tissue behavior of organs for surgical navigation with convolutional neural networks," *International Journal of Computer Assisted Radiology and Surgery*, vol. 14, no. 7, pp. 1147–1155, 2019. [Online]. Available: https://doi.org/10.1007/s11548-019-01965-7

[38] A. Madani, A. Bakhaty, J. Kim, Y. Mubarak, and M. R. K. Mofrad, "Bridging Finite Element and Machine Learning Modeling: Stress Prediction of Arterial Walls in Atherosclerosis," *Journal of Biomechanical Engineering*, vol. 141, no. 8, may 2019. [Online]. Available: https://doi.org/10.1115/1.4043290

[39] T. Da Veiga, J. H. Chandler, G. Pittiglio, P. Lloyd, M. Holdar, O. Onaizah, A. Alazmani, and P. Valdastri, "Material characterization for magnetic soft robots," in *2021 IEEE 4th International Conference on Soft Robotics (RoboSoft)*, 2021, pp. 335–342.

[40] M. Di Lecce, O. Onaizah, P. Lloyd, J. Chandler, and P. Valdastri, "Evolutionary inverse material identification: Bespoke characterization of soft materials using a metaheuristic algorithm," *Front Robot AI.*, no. 14;8:790571, Jan 2022.

[41] R. J. Roesthuis and S. Misra, "Steering of multisegment continuum manipulators using rigid-link modeling and fbg-based shape sensing," *IEEE transactions on robotics*, vol. 32, no. 2, pp. 372–382, 2016.

[42] S. Salmanipour and E. Diller, "Eight-Degrees-of-Freedom Remote Actuation of Small Magnetic Mechanisms," in *2018 IEEE International Conference on Robotics and Automation (ICRA)*, 2018, pp. 3608–3613.

[43] F. Connolly, P. Polygerinos, C. J. Walsh, and K. Bertoldi, "Mechanical programming of soft actuators by varying fiber angle," *Soft Robotics*, vol. 2, no. 1, pp. 26–32, 2015.

# Chapter 2

# Magnetic Shape Forming Soft Robots

**Chapter source:** P. Lloyd, A. K. Hoshiar, T. da Veiga, A. Attanasio, N. Marahrens, J. H. Chandler, and P. Valdastri, “A learnt approach for the design of magnetically actuated shape forming soft tentacle robots,” IEEE Robotics and Automation Letters, vol. 5, no. 3, pp. 3937–3944, 2020.

## Abstract

Soft continuum robots have the potential to revolutionize minimally invasive surgery. The challenges for such robots are ubiquitous; functioning within sensitive, unstructured and convoluted environments which are inconsistent between patients. As such, there exists an open design problem for robots of this genre. Research currently exists relating to the design considerations of on-board actuated soft robots such as fluid and tendon driven manipulators. Magnetically reactive robots, however, exhibit off-board actuation and consequently demonstrate far greater potential for miniaturization and dexterity. In this paper we present a soft, magnetically actuated, slender, shape forming ‘tentacle-like’ robot. To overcome the associated design challenges we also propose a novel design methodology based on a Neural Network trained using Finite Element Simulations. We demonstrate how our design approach generates static, two-dimensional tentacle profiles under homogeneous actuation based on predefined, desired deformations. To demonstrate our learnt approach, we fabricate and actuate candidate tentacles of 2mm diameter and 42mm length producing *shape* profiles within 8% mean absolute percentage error of desired shapes. With this proof of concept, we make the first step towards showing how tentacles with bespoke magnetic profiles may be designed and manufactured to suit specific anatomical constraints.

## 2.1 Introduction

Continuum Manipulators (CMs) have been used to assist with and enable surgical procedures in the form of catheters and endoscopes for at least the last 120 years [1]. Traditional CMs rely on body rigidity to transmit forces and torques from proximal to distal ends.

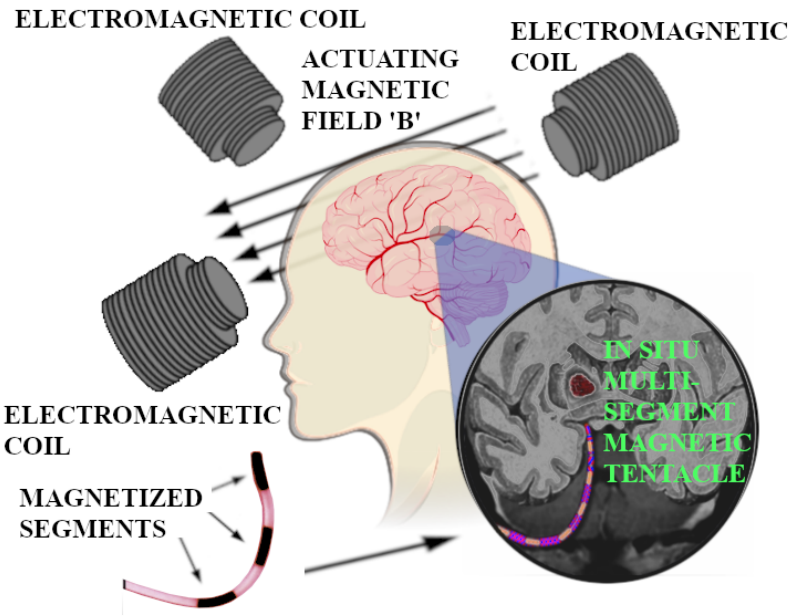

Figure 2.1: A sample application of the magnetically actuated tentacle – neurovascular catheter navigation. The target shape is derived from a pre-operative Magnetic Resonance Image of the brain. Under specific electro-magnetic actuation, the desired shape is assumed.

This approach relies on operator skill, offers limited accuracy or dexterity and the process itself can cause tissue trauma [2]. These limitations may be mitigated with the use of soft robotic manipulators which are primarily fabricated from elastomeric materials and actuated through a wide range of methods as detailed in [3]. Common methods of actuation are fluid driven [4], tendon driven [5], shape memory alloy [6], electroactive polymer [7] and magnetic [8] systems. For the non-magnetic 'on-board' actuated systems a fundamental trade-off will always exist between dexterity and miniaturisation potential; for each additional degree of freedom (DoF) controlled within the manipulator, a further driveline (e.g. a fluid channel or tendon) must be added. This limitation does not apply to magnetic actuation and, consequentially, the magnetic approach exhibits far greater potential for miniaturisation and therefore surgical application than rival methods.

Magnetically actuated tip driven systems [9] [10] have been demonstrated to increase control and reduce trauma [11], [12] during the negotiation of anatomical convolutions. Recently a number of works [13], [14], [8] have demonstrated the efficacy and miniaturisation potential of such catheters. These systems, however, can only assume the body shape of their respective conduit via anatomical interaction. A soft continuum robot equipped with full body-shape control would possess the potential to assume a predefined shape without relying on these forces. We would consider such a robot, with numerous wrenches acting along its length, to be ‘fully shape forming’ in contrast to the conventional tip driven manipulators. The magnetic shape control demonstrated in [15], [16] and [17] could, in principle, be exploited to provide a safe railroad to a predefined working location. This would enable improvements in safety, procedure time and patient comfort; this concept is shown schematically in Fig. 2.1. For real-world applications, the highly convoluted geometries and millimetre scale workspaces encountered make magnetic actuation a promising, if challenging, avenue of research. Magnetic actuation, however, comes with its own attendant complexities regarding the modelling and simulation of long, slender and therefore potentially unstable, magnetically active elastomers. Henceforth, we refer to our slender, shape forming, soft robots as magnetic tentacles.

Shape forming CMs presented in the literature exhibit a variety of modelling methods. Most prominently we observe the Cosserat rod [18], the constant curvature [19] and the rigid-link [20] models. Each model represents a level of approximation and attendant computational intensity deemed appropriate for its particular application. There also exists the set of magnetically actuated shape forming materials [21], [22], [16] which have heavily influenced this work. These tend to employ a full continuum mechanics model via commercial FEM packages as, generally, they are not considering closed loop control applications. The subset at the intersection of these two groups (where our work resides) is the magnetically actuated rectangular cross-section shape forming continuum robots appearing in [17] and [23]. These use a numerically intensive Fourier representation of manipulator shape to solve their statics and dynamics.

The concept of a fully flexible, shape forming tentacle robot fabricated from a magnetically active elastomer, orders of magnitude softer than present day catheters, represents a step change in the evolution of CM design. These tentacles can be pre-programmed to assume the profile of the conduit through which they are designed to pass. This relies on prior knowledge of the route in question - which may be derived from pre-operative imaging - and a methodology to translate this pathway into a magnetization profile. The contribution presented here offers a first step towards this goal coupled with a design methodology to overcome the inherent complications of magnetically active elastomers.

The two discrete functions of the tentacle can be defined as; quasi-static shape forming and dynamic shape forming. The first, quasi-static role, is to stiffen into a pre-defined shape upon arrival at a specific location such as the tumour at the base of the skull illustrated in Fig. 2.1. This stiffening would provide a safe and robust working channel for the delivery of treatment and the evacuation of tissue whilst also permitting the increased force required for cutting or ablation. The second, dynamic role, would incorporate shape forming during navigation to that same working location and would be driven by an in-homogeneous and transient magnetic field. The work presented here considers the quasi-static case under a planar, homogeneous and time invariant actuating field.

The first contribution of this work is to present the fundamental concept, including the fabrication process, of our fully soft, shape forming tentacle robots. The second contribution is our learnt approach to the two-dimensional design of these tentacles, actuated in a time-invariant homogeneous field. We employ a Finite Element Model (FEM) as the source of training data for a fully connected Artificial Neural Network (ANN). The output of the trained ANN represents the solution to the inverse statics of our soft robot - when we refer to forward and inverse *statics*, we are referring to the soft serial robot equivalent of kinematics in conventional hard robotics. The difference being the requirement, for a soft robot, of forces to maintain static equilibrium. This solution in turn informs the design of our experimental prototypes. The results produced by the ANN are validated for three demonstrative shapes in both the underlying FEM and, after fabrication, in our experimental setup.

## 2.2 Design Approach

Machine learning techniques which are driven by real-world experimental data can minimise or even bypass modelling assumptions. To train such networks, learning via demonstration [24], or input from a randomized feed (sometimes referred to as motor babble) [25] offer valid methods. However, in the absence of high-volume, reliable sensory data and the ability to rapidly prototype test samples these real-world approaches are unfeasible. For our design methodology we therefore employ a FEM as the source of training data for a fully connected ANN.

Utilizing FEM to simulate the interaction between magnetic and mechanical forces has been successfully demonstrated in previous work [21] and been successfully applied to CMs [8]. In addition, the use of ANNs as surrogates of FEMs has also been reported; for example in [26] and [27] convolutional neural networks are used to fully recreate FE simulations of a liver and an arterial wall respectively. These works exhibit results evidencing the effectiveness of deep learning in this particular sphere of research. To the authors knowledge there are no examples in the literature of Neural Network replication of Finite Element Modelling for CMs under magnetic actuation or otherwise.

The approach taken to realise our FEM surrogate ANN is comprised of the following steps: (1) a simplified single segment FEM is used to set modelling assumptions based on correlation with experimental data; (2) the FEM is extended to a functional number of magnetized segments; (3) a large number of simulations are performed to create a database for training validation and testing of the ANN; (4) the ANN is trained; (5) the ANN generalises for predefined, novel tentacle shapes; and (6) these shapes are verified in the multi-segment FEM, fabricated, and experimentally evaluated under a homogeneous magnetic field.

## 2.3 Modelling Approach

### 2.3.1 Constitutive Model

For the purposes of this study, we assume the elastomer in consideration is homogeneous, isotropic and, for the range of strains experienced herein, incompressible. Assuming a quasi-static state and entirely elastic deformation, under the Lagrangian description in

[28], the deformation gradient tensor F is the partial derivative of the deformed position with respect to the relaxed position.

For the case of a magnetic material, torque when placed wholly within a homogeneous magnetic field, may be defined as the cross product of magnetic moment (m) and the surrounding field of flux (B). This may be considered as the mechanical work of the magnetic torque performed to align the magnetic dipole moments [21]. Defining magnetization as $M = \frac{m}{V}$ we can say that the Cauchy stress tensor for magnetic effects is:

$$\sigma^{mag} = (M \times B) \cdot F \tag{2.1}$$

and with reference to the quasi-static assumption we can also state that, for the full Cauchy stress tensor:

$$div(\sigma) + f_g = 0 \tag{2.2}$$

where $f_g$ is the body force vector per unit volume; equal to gravity as magnetic body forces are included in the stress tensor. These two equations can be solved for appropriate boundary conditions to give the deformation gradient tensor and thus the deflection of our tentacle due to magnetic actuation.

### 2.3.2 The Single Segment Cantilever Beam Model

Using the planar cantilever beam of uniform magnetization, depicted in Fig. 2.2, as our example, it is possible to compare experimental data with an analytic model and our FEM. This permits verification of our assumptions before we extend the FEM beyond the reach of any analytical solution. In the simple shear stress model, the symmetrical mechanical stress components net to zero leaving only the magnetic stress components contributing to bending moment. From Euler-Bernoulli beam theory we can thus say that:

$$\frac{\delta}{L} = \frac{(m_1 B_2) 16 L^2}{3 E d^2} \tag{2.3}$$

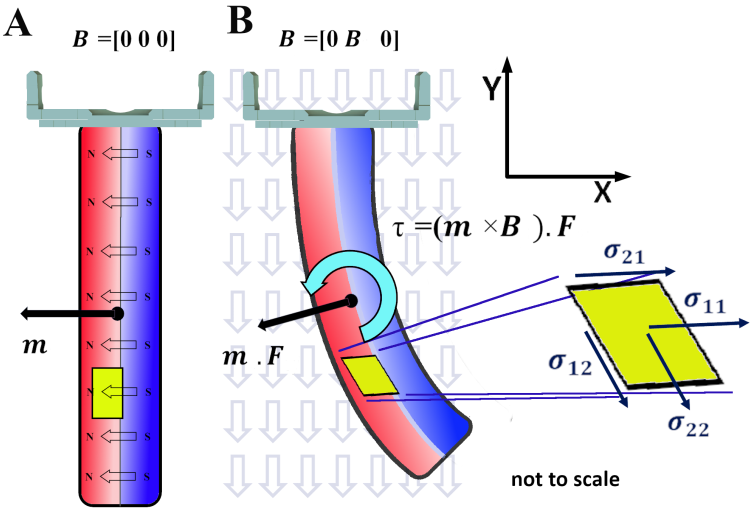

Figure 2.2: **(A)** The undeformed position under a zero actuating field, the tentacle is magnetized in the $-x$ direction. **(B)** The deformed position under an actuating torque $\tau$ generated by the field, $B$, applied orthogonally to the magnetization $m$. The deformation gradient tensor $F$ influences the effective direction of magnetization. An exploded infinitesimal volume shows the Cauchy stress tensor $\sigma$ in two dimensions.

where $\delta$ is beam deflection, $E$ is elastic modulus, $L$ is length and $d$ is diameter. As in [29], given invariant geometric and material properties, (2.3) offers a linear correlation between $\delta$ and $B_2$. To simulate the system, FEMs were constructed under the plane strain assumption in two dimensions in COMSOL multiphysics suite v5.4 (COMSOL AB, Stockholm, Sweden). The model employed solid mechanics and electromagnetics modules connected via the Maxwell surface stress tensor utilizing Newton-Raphson iterative convergence within the MUltifrontal Massively Parallel sparse direct Solver (MUMPS) option.

Due to the highly non-linear nature of the Maxwell equations, the mesh optimization process results in local mesh concentrations around the edges of the magnetized segments (visible in Fig. 2.3). These segment edges were constrained to 50 nodes per 7mm length and 25 nodes per 1.5mm diameter. A maximum element growth rate of 1.2 was applied throughout. The air domain in which the tentacle is suspended is 250mm x 250mm with a zero gradient boundary condition applied around its periphery. This domain has a maximum element growth rate of 1.1 and a maximum element size of 20mm. For the single segment cantilever case, the resultant model was comprised of 27,000 free triangular

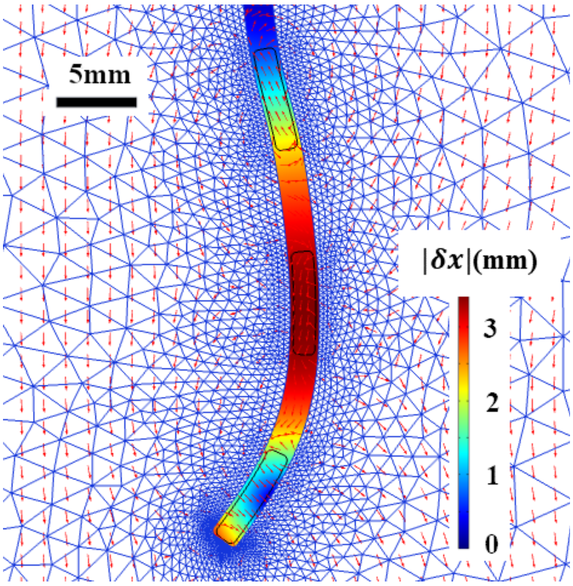

Figure 2.3: The multi-segment Finite Element Model: three discretely magnetized segments in a homogeneous background field. This is numerically represented by 238,000 spatially optimized nodes and produces a range of poses which are quantified by deflections in x and y at three Points of Interest down the length of the tentacle.

(two-dimensional) nodes.

### 2.3.3 The Multi-Segment Model

The multi-segment 'tentacle' structure was represented with three discrete segments of magnetically doped elastomer, 7.0mm long by 1.5mm diameter, embedded within the magnetically unreactive silicone, 42mm in length by 2mm in diameter. The magnetization direction of each segment can be independently controlled within the two-dimensional plane. To generate a geometrically accurate simulation, the resulting FEM, as shown in Fig. 2.3, was discretized using 238,000 free triangular (two-dimensional) nodes subject to the same constraints as the single segment mesh (Section 2.3.2).

## 2.4 The Artificial Neural Network

The appeal of Machine Learning (ML) for our problem is its ability to generalize for previously unseen scenarios from sample data thus forecasting future outcomes in the absence of a constitutive model. This renders ML an ideal tool for solving contrived inverse static problems such as those occurring in hyper-redundant, elastomeric CMs.

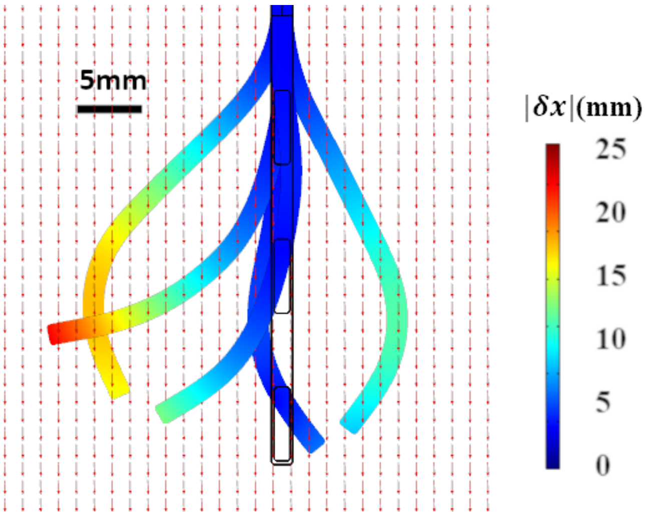

Figure 2.4: A visual sample of the 13,800 shapes generated during the 'virtual motor babble' phase. A snapshot of this process features in the supplementary video.

### 2.4.1 The Dataset

In order to train an ANN, we need large quantities of data. In real world applications, as described previously, this can be produced via motor babble. To generate 'virtual motor babble', we parametrically swept each of the three magnetization input variables. For each magnetized segment of the tentacle the modulus of the magnetization vector remains unchanged, the only variable is the direction of magnetization. As such the input to be swept can be represented by three unit vectors representing magnetization direction.

An incremental rotation of the magnetization vector of $\frac{1}{24}$ of a revolution (24 possible values for each of 3 input variables) produces $24^3 = 13,824$ sequential entries. These actuating variables were fed as inputs to the pre-assembled FEM and run on a 3.2GHz, 32GB, 16 core Intel Xeon Gold processor in a total run time of 38 hours. This process generated a set of deflection vectors at each of three Points of Interest (PoI) corresponding to the magnetization vectors at those same PoI. To represent, as a point in space, the global position of a segment of non-zero volume, the centre of mass of each of the three magnetically active segments was chosen as the PoI. An example selection of resultant deformed tentacles is shown in Fig. 2.4.

As illustrated in Fig. 2.5, for each segment, the magnetization angle produces a deflection. This deflection reaches some maximum, beyond this point further increases in magnetization angle, $\theta$, will begin to reduce deflection. This phenomenon produces a non-unique relationship between inputs and outputs – kinematic redundancy - something which is anathema to a Neural Network. It is therefore necessary to systematically remove duplicate results; those vectors residing in the red shaded region of Fig. 2.5, from each of the three actuating segments. The resulting lookup table reduces from 13,824 systematically produced entries to 2298 unique solutions each with 6 dimensions of input data (two-dimensional magnetization vectors at three PoI) and a corresponding 6 dimensions of output data (two-dimensional deflection vectors at the same three PoI). These planar deflection vectors are simplified to scalars, representing the lateral x-displacement of the PoI on the actuated manipulator to the unactuated centreline. Under the assumption of negligible tentacle extension (under 5mT actuation a maximum stretch of 0.1% is observed in the numerical model) it can be assumed that y-deflection is purely a function of x-deflection i.e. only one DoF exists per segment. This dataset is split 70% for training, 15% for validation and 15% for testing.

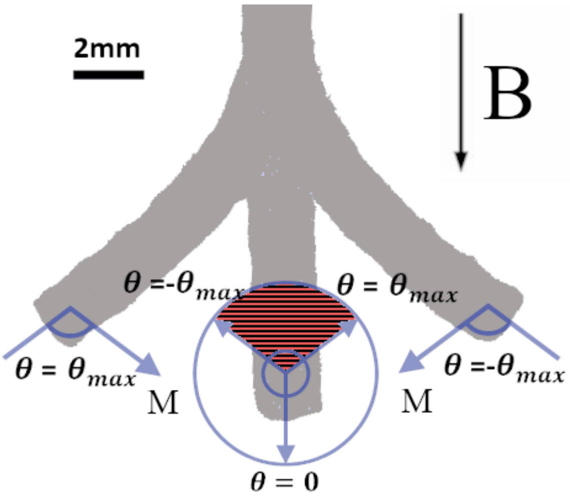

Figure 2.5: Schematic of the positive and negative angles of maximum deflection. For a fixed applied field ‘B’, and fixed initial pose a maximum deflection is achievable by applying a magnetization ‘M’ at an angle $\theta_{max}$(or $-\theta_{max}$). The single segment tentacle is shown in grey with the unactuated pose in the centre of the image and the maximum and minimum deflections also shown. For magnetization angles greater than $\theta_{max}$ the resultant deflection will drop, rendering results produced by magnetizations in the red shaded region repetitious.

### 2.4.2 The Learning Network

The architecture of the ANN employed to replicate the FEM is a fully connected neural network with an output regression layer. The effect of variations in number of neurons and number of hidden layers was assessed based on runtime and validation accuracy and the final arrangement emerged containing 6 hidden layers of 20 neurons each. After iterating for 60 epochs of Levenberg-Marquardt backpropagation of error employing sigmoid activation functions this arrangement gave a 6.3% mean absolute percentage error (MAPE) at the validation (inverse model) phase.

## 2.5 Fabrication

### 2.5.1 The Single Segment

The single segment was fabricated from Ecoflex 00-30 embedded with neodymium-iron-boron (NdFeB) microparticles with an average diameter of 5 $\mu$m (MQFP-B+, Magnequench GmbH, Germany). Particles of NdFeB were added to the prepolymer in a 1:1 ratio by weight equating to a volumetric ratio of 0.88:0.12 (Ecoflex:NdFeB). The compos-

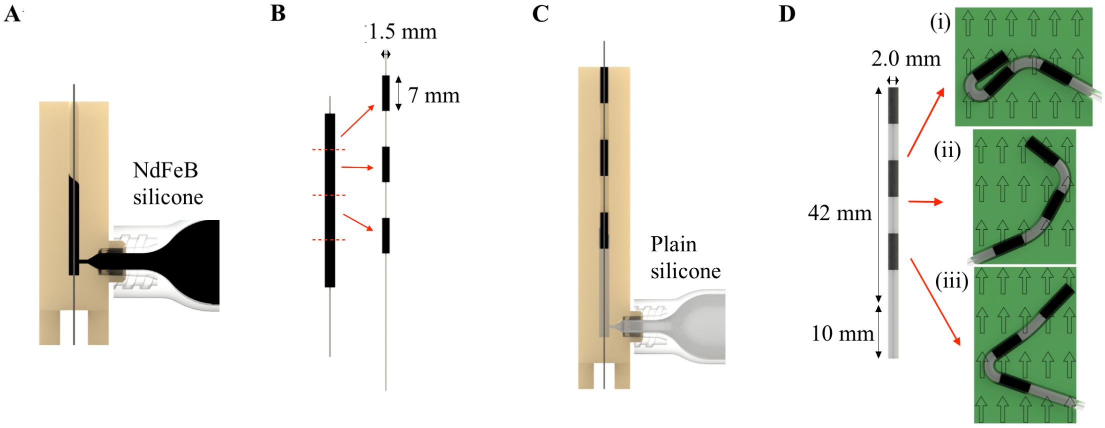

Figure 2.6: . Fabrication process of a multi-segment tentacle. (A) Injection molding of a continuous, magnetizable tentacle of diameter 1.5mm. (B) Once cured, the elastomer is cut into 7mm segments and positioned along the Nitinol needle at 14mm centres. (C) The needle is placed in a second mold of diameter 2mm and injected with plain silicone. (D) After curing, demolding and needle removal, the tentacle is placed in a 3D printed magnetizing tray. Here the three trays (i), (ii) and (iii) correspond to the scenarios A, B and C shown in Section 3.5 Results.

ite was mixed and degassed in a high vacuum mixer (ARV-310, THINKYMIXER, Japan) at 1400 rpm, 20.0 kPa for 90 seconds and then injected onto a straight cylindrical mold of diameter d=1.5mm and length 20mm and left to cure. The mold contained a centrally aligned 0.25mm diameter Nitinol needle running for 10mm of its length. This needle remained embedded in the polymer and was used to suspend and constrain the specimen during testing. Once the polymer had cured, the specimen was subjected to a uniform field of 46.44 KGauss (4.644 T) (ASC IM-10-30, ASC Scientific, USA) orthogonal to the tentacle's principle axis.

### 2.5.2 The Multi-Segment Tentacle

For the multi-segment arrangement, the unmagnetized doped elastomer (Fig. 2.6A) was divided into three identical 7mm segments (Fig. 2.6B). Each segment was subsequently embedded, concentrically, at 14mm intervals (in the longitudinal direction) into an undoped silicone host (Ecoflex 00-30) (Fig. 2.6C). A centrally aligned 0.25mm Nitinol needle supports the *full length* of the structure during fabrication. Upon curing this needle is removed save for the final 10mm which remains embedded to act as the mechanical constraint during experimentation. The total length of the multi-segment tentacle (Fig. 2.6D) is 52mm. From bottom to top this can be broken down as 10mm of constrained length followed by 42mm of unconstrained length. Undoped segments appear white and doped segments appear black. The dimensional accuracy of the fabricated tentacle samples was assessed through image analysis software (LAZ EZ, Leica, Germany), calibrated against a known reference length with images obtained using a digital light microscope (DMS300, Leica, Germany). Values of segment lengths (Mean+/-SD) were found to be 7.4+/-0.43mm, and segment diameters were 1.9+/-0.03mm. For future work it is planned that an automated fabrication technique would significantly reduce these errors and, for any systematic discrepancies, a post fabrication analysis could identify and incorporate these into simulations.

This arrangement was housed in a magnetizing tray (Fig. 2.6D) and exposed to the same 46.44 KGauss saturating field which was employed to magnetize the single segment.

The geometry of the magnetizing tray was driven by the solution to the inverse static problem for the soft robot. This solution was generated by the Neural Network based on pre-defined desired deflections.

## 2.6 Experimental Evaluation

### 2.6.1 The Single Segment

The single segment was hung vertically downwards on its embedded Nitinol needle in the centre of a Helmholtz coil (DXHC10-200, Dexing Magnet Tech. Co., Ltd, Xiamen, China). As in Fig. 2.7, 10mm of this 20mm section was constrained by the Nitinol needle and 10mm was free to deform. The Helmholtz coil was arranged so as to produce a vertically aligned homogeneous magnetic field. The current through the coils was ramped from -10mT to 10mT in 2mT increments to produce a piece-wise increasing actuating field orthogonal to the undeformed magnetization of the test piece. Images of the specimen were taken on a Nikon D5500 DSLR with an AF-S NIKKOR 18-55mm lens at each field strength and were post-processed in GIMP 2.10 prior to analysis. The maximum deflection was measured at the centre of the distal end of the specimen in both the numerical and experimental analyses. The experiment was repeated three times, the first iteration of which is shown in Fig. 2.7 and also in the supporting video.

This analysis was performed to verify the mechanical and magnetic properties of the doped elastomer. The Elastic modulus of the doped and undoped silicone was measured to be 91 kPa and 69 kPa respectively. These values were obtained using a uniaxial load tester (MultiTest 2.5-xt, Mecmesin, UK) operating up to a maximum of 100% strain. The Poisson's ratio was set to 0.5 for both elastomers representing the assumption of incompressibility. The remanent flux density of the doped elastomer was calculated to be 107 mT which reconciles with comparable works in [17] and [21].

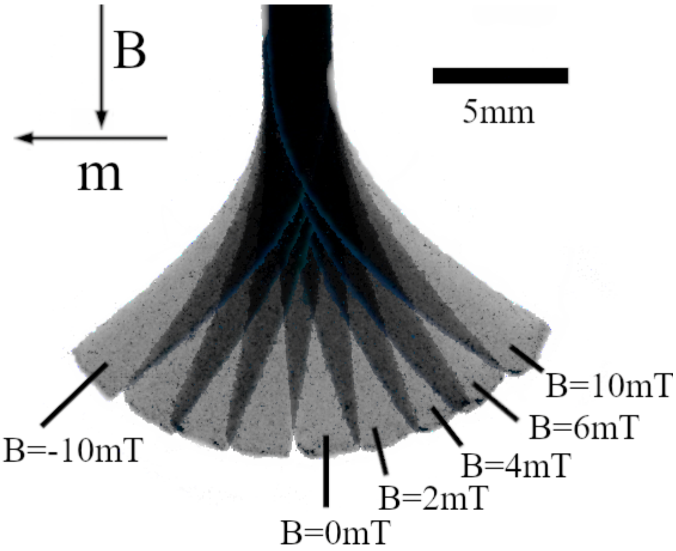

Figure 2.7: Superimposition of experimental results for fixed magnetization'm' for the range of Magnetic fluxes from B=-10mT to B=10mT in 2mT increments. For the purposes of visual clarity some results are omitted. The upper 10mm of the elastomer is restrained on a Nitinol pin whilst the lower 10mm is free to deform. A video of this actuation is included in the supplementary material.

### 2.6.2 The Multi-Segment Tentacle

As with the single segment arrangement the multi-segment tentacle was hung in the vertically aligned homogeneous field of the Helmholtz coil. For the multi-segment model, a field of 5mT was applied (10mT actuating fields appear in the supporting video). Images of the tentacles were taken on the same camera as the single segment arrangement and again processed in GIMP 2.10. After superimposition of the undeformed and deformed images from the experimental setup, deflections were measured along the x-axis from centre to centre of each of the three magnetized segments. Due to the rigid tubular formwork used during the fabrication process, unactuated tentacle deformations are minimal (MAPE 0.27mm or 0.6% of robot length, when subject to gravity). Furthermore, the zero line for deflection measurements is taken from the unactuated tentacle position, thus mitigating the worst of any residual unactuated deformation.

## 2.7 Results

The analytical result derived in Section 2.3 using (2.3) is shown in Fig. 2.8 and can be seen to produce a less than accurate replica of experimental and numerical results even in the small strain region. As deflection increases the linear analytical model becomes increasingly inaccurate, quickly reaching a point where it can no longer be said to represent the behavior of the tentacle at all.

The single-segment FEM results, also shown in Fig. 2.8, reflect the experimental results with a MAPE of 14.9% up to the maximum field strengths of ±10mT. This result effectively verifies the material and magnetic properties of the elastomer in the numerical model and provides the requisite confidence in the FEM to extend the simulation up to the multi-segment tentacle.

As shown in Fig. 2.9, the multi-segment system was tested using three different x-axis desired deflections. The trained ANN translated these idealized outcomes into magnetization vectors based on its learnt weights. These magnetization vectors were input into the original FEM for validation. For the three candidate profiles the ANN replicated the

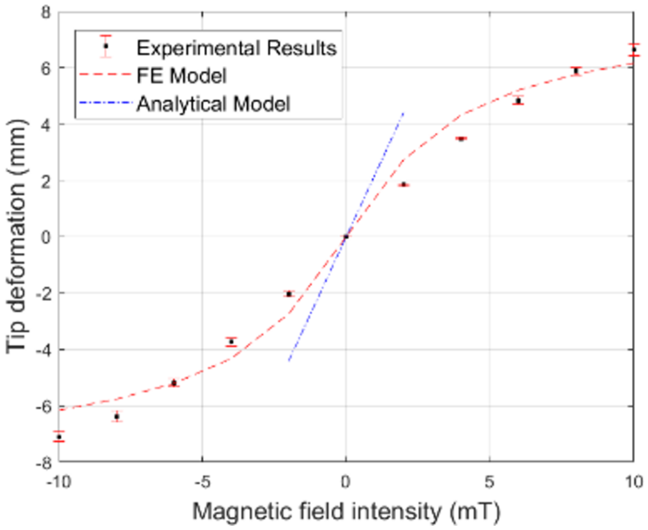

Figure 2.8: A comparison of deformations for Experimental, Numerical and Analytical solutions for the homogeneously magnetized single segment elastomer. The average error between experimental and numerical output is 14.9%. As can be observed, the linear beam analytical model offers a fairly poor approximation for this highly non-linear system, particularly at higher strains.

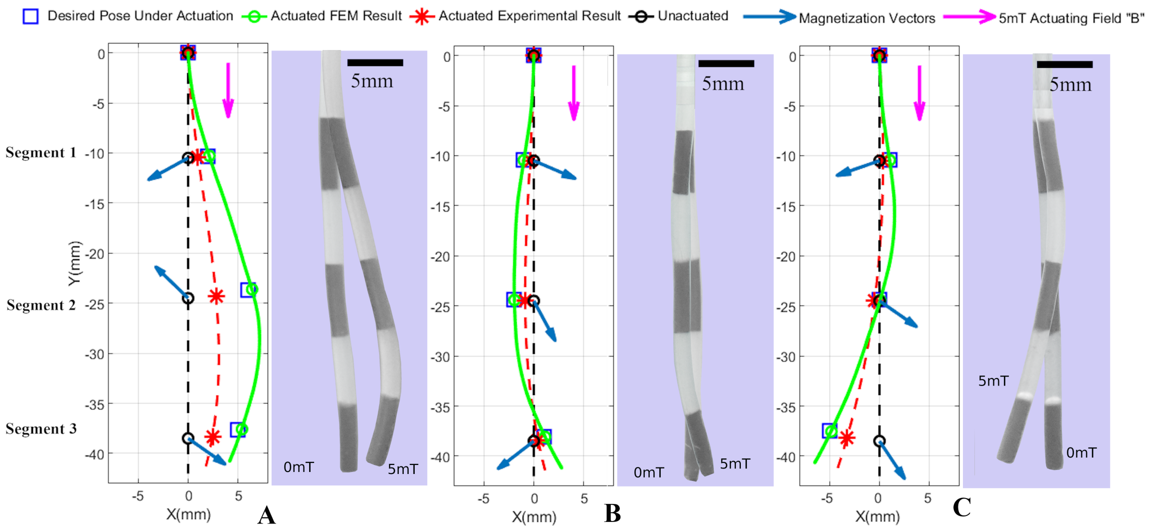

Figure 2.9: Sample experimental results shown against numerical results for three predefined scenarios of the full tentacle. The magnetization vectors are the output of the trained Neural Network using desired deflections as input. The experimental result on the right is shown with B=0 and 5mT. The graphical result on the left shows both experimental and numerical outcomes. (A) Desired deflections (top to bottom) of $\delta$x = [2 6 5] (mm). (B) $\delta$x = [-1 -2 1] (mm). (C) $\delta$x = [1 0 -5] (mm).

FEM with a MAPE of 4.4%. This reconciles with the validation error of 6.3% shown in Section 2.4.2.

Table 2.1 shows absolute x-axis deflection and, in brackets, x-axis deflection as a percentage of maximum. The absolute deflection reveals discrepancies in magnitude between experimental and numerical results. From the images in Fig. 2.9, it can be observed that

Table 2.1: A comparison of x-axis deflection for the input to the neural network, the output of the FEM and the experimental readings. Deflections are also shown, in brackets, as percentage of maximum.

**Scenario A**

| *Segment Number* | *Requested x Deflection (mm)* | *Numerical Deflection (mm)* | *Experimental Deflection (mm)* |
|---|---|---|---|
| 1 | 2 (33%) | 2.1 (33%) | 0.9 (35%) |
| 2 | 6 (100%) | 6.4 (100%) | 2.6 (100%) |
| 3 | 5 (83%) | 5.4 (84%) | 2.2 (85%) |

**Scenario B**

| *Segment Number* | *Requested x Deflection (mm)* | *Numerical Deflection (mm)* | *Experimental Deflection (mm)* |
|---|---|---|---|
| 1 | -1 (50%) | -1.0 (53%) | -0.4 (44%) |
| 2 | -2 (100%) | -1.9 (100%) | -0.9 (100%) |
| 3 | 1 (-50%) | 1.1 (-58%) | 0.4 (-44%) |

**Scenario C**

| *Segment Number* | *Requested x Deflection (mm)* | *Numerical Deflection (mm)* | *Experimental Deflection (mm)* |
|---|---|---|---|
| 1 | 1 (-20%) | 1 (-21%) | 0.4 (-12%) |
| 2 | 0 (0%) | 0.1 (-2%) | -0.5 (15%) |
| 3 | -5 (100%) | -4.8 (100%) | -3.3 (100%) |

the experimental prototypes are deforming into a comparable *shape* to those requested (if not by a comparable *magnitude*). As such, proportional deflections are included to give a comparison of shape only. This normalizing process has been included purely for representational reasons; to enable the visual shape comparison available in Fig. 2.9 to be quantified. The existence of this adjustment is a recognition of two key limitations of this study. The first relates to the un-modelled three-dimensional effects unavoidably embedded in the multi-segment experiment. To accurately replicate the two-dimensional assumption made in the numerical model we would need to magnetize our specimens in a perfectly planar and twist-free fashion. This is unachievable and the consequence of any unwanted axial rotation introduced here is a loss of magnetic moment in the plane being considered. The second limitation is the non-automated fabrication and magnetization process of the multi-segment arrangement. As discussed earlier, the tentacle does not exactly achieve its intended dimensions, exhibits some unactuated deformation and, additionally, will not be magnetized in exactly the intended directions.

Both of these factors are significant areas for future work discussed in Section 4.6. Furthermore errors may well persist in the measurement and calculation of material and magnetic properties. Notwithstanding this, after normalization, the *shape* profiles give results with a MAPE across all scenarios of 7.8%, calculated as

$$\epsilon = \frac{\sum_{j=1}^{3}\sum_{i=1}^{3}(|\delta x_{i,j}^{exp(norm)} - \delta x_{i,j}^{requested}|)}{\sum_{j=1}^{3}\sum_{i=1}^{3}(|\delta x_{i,j}^{requested}|)}$$

Where i = segment number, j = scenario number and

$\delta x_{i,j}^{exp(norm)}$ = normalized experimentally measured deflection, calculated as

$$\delta x_{i,j}^{exp(norm)} = \delta x_{i,j}^{exp} . \frac{\sum_{i=1}^{3}(|\delta x_{i,j}^{requested}|)}{\sum_{i=1}^{3}(|\delta x_{i,j}^{exp}|)}$$

Where $\delta x_{i,j}^{exp}$ = experimentally measured deflection and $\delta x_{i,j}^{requested}$ = requested deflection from initial desired path.

More work will of course be required to understand the discrepancy observed in the magnitude of deflection.

## 2.8 Conclusions

Once trained, the ANN produces a reliable replica of the FEM and is capable of producing forward and inverse static results in real-time with 6.1% MAPE. This system of design, of course, is not limited to magnetically actuated CMs and could well be generalized to other applications. Once duplicate results have been removed from the training data (Section 2.4.1), the ANN can provide a useful surrogate of the numerical model subject to one further caveat; the operational workspace of the robot. Without external assistance the ANN, unlike the FEM, has no indication of which deformations lie within or outside of the physical scope of the system. This requires additional restrictions to the neural network, connecting desired deflections to the lookup table of possible outcomes. At present these restrictions are applied on a manually observed basis but for future work this system should be automated.

Beyond the accuracy of the learner, any significant further errors can be attributed to the modelling assumptions entering the FEM and to limitations in the manual fabrication and magnetization process. These will be reduced with further experimentation, fabrication process refinement, the inclusion of more sophisticated elasticity and magnetic field models in the FEM and inclusion of the third spatial dimension. In any future application of the proposed method, we would also aim to integrate an appropriate sensing technique (e.g. [30], [31], [32], [33]) to identify and balance the discrepancy between model and reality. This could inform a specific magnetic field controller which, in turn, would adjust the field to achieve the desired shape.

As well as the above improvements this work can now be extended for more convoluted, real-world trajectories derived from pre-operative imaging. This will be enabled by a greater variety of input variables (including geometric) to the lookup table. In addition to this, stiffening under actuating fields is known to occur for magnetic elastomers [34], harnessing this property to improve the capabilities of magnetic tentacles will form an interesting area of future research. It should also be noted that the current technique for generating magnetic fields is limited to homogeneous field generation within a centimetre scale workspace and therefore unsuitable for clinical application. For future feasibility, and also to address the issue of dynamic shape forming for navigation, there are a variety of potential methods of field generation available which operate on a much larger scale and with higher degrees of freedom [35], [36], [10]. In particular [12] and [37] propose magnetic manipulation using a permanent magnet positioned at the end effector of a medical-grade serial robotic manipulator whilst [13] employ an electromagnetic actuator hosted on a similar serial robot arm providing a clinically relevant workspace. Furthermore [38] propose actuation by means of a clinically-relevant external magnetic resonance imaging (MRI) system.

Looking further ahead, with improved sensing technology, we may be able to eliminate the FE model altogether and train the ANN from incoming sensory data thus fully eliminating modelling error and further harnessing the enormous potential of Machine Learning. With this work we have begun to demonstrate the potential of our magnetic shape forming tentacles and their scope to, in future works, conform to specific anatomical constraints.

## Bibliography

[1] G. S. Litynski, “Laparoscopy–the early attempts: spotlighting Georg Kelling and Hans Christian Jacobaeus,” *JSLS : Journal of the Society of Laparoendoscopic Surgeons*, vol. 1, no. 1, pp. 83–85, 1997. [Online]. Available: https://www.ncbi.nlm.nih.gov/pubmed/9876654https://www.ncbi.nlm.nih.gov/pmc/articles/PMC3015224/

[2] K. A. Hausegger, P. Schedlbauer, H. A. Deutschmann, and K. Tiesenhausen, “Complications in endoluminal repair of abdominal aortic aneurysms,” *European journal of radiology*, vol. 39, no. 1, pp. 22–33, 2001.

[3] J. Burgner-Kahrs, D. C. Rucker, and H. Choset, “Continuum robots for medical

applications: A survey," *IEEE Transactions on Robotics*, vol. 31, no. 6, pp. 1261–1280, 2015.

[4] I. De Falco, M. Cianchetti, and A. Menciassi, "A soft multi-module manipulator with variable stiffness for minimally invasive surgery," *Bioinspiration & Biomimetics*, vol. 12, no. 5, p. 56008, 2017. [Online]. Available: http://dx.doi.org/10.1088/1748-3190/aa7ccd

[5] C. Heunis, J. Sikorski, and S. Misra, "Flexible Instruments for Endovascular Interventions: Improved Magnetic Steering, Actuation, and Image-Guided Surgical Instruments," *IEEE Robotics and Automation Magazine*, vol. 25, no. 3, pp. 71–82, 2018.

[6] Y. Kim, S. S. Cheng, M. Diakite, R. P. Gullapalli, J. M. Simard, and J. P. Desai, "Toward the development of a flexible mesoscale mri-compatible neurosurgical continuum robot," *IEEE Transactions on Robotics*, vol. 33, no. 6, pp. 1386–1397, Dec 2017.

[7] A. Benouhiba, K. Rabenorosoa, P. Rougeot, M. Ouisse, and N. Andreff, "A multisegment electro-active polymer based milli-continuum soft robots," in *2018 IEEE/RSJ International Conference on Intelligent Robots and Systems (IROS)*. IEEE, 2018, pp. 7500–7506.

[8] S. Jeon, A. K. Hoshiar, K. Kim, S. Lee, E. Kim, S. Lee, J.-y. Kim, B. J. Nelson, H.-J. Cha, B.-J. Yi, and H. Choi, "A Magnetically Controlled Soft Microrobot Steering a Guidewire in a Three-Dimensional Phantom Vascular Network," *Soft Robotics*, vol. 6, no. 1, pp. 54–68, oct 2018. [Online]. Available: https://doi.org/10.1089/soro.2018.0019

[9] J. Martin, J. Martin, J. Norton, K. L. Obstein, and P. Valdastri, "Toward Autonomous Robotic Colonoscopy: Motion Strategies for Magnetic Capsule Navigation," in *2018 IEEE International Conference on Cyborg and Bionic Systems (CBS)*, 2018, pp. 240–244.

[10] J. Edelmann, A. J. Petruska, and B. J. Nelson, "Magnetic control of continuum devices," *The International Journal of Robotics Research*, vol. 36, no. 1, pp. 68–85, 2017. [Online]. Available: https://doi.org/10.1177/0278364916683443

[11] L. Barducci, G. Pittiglio, J. C. Norton, K. L. Obstein, and P. Valdastri, "Adaptive dynamic control for magnetically actuated medical robots," *IEEE robotics and automation letters*, vol. 4, no. 4, pp. 3633–3640, 2019.

[12] J. C. Norton, P. R. Slawinski, H. S. Lay, J. W. Martin, B. F. Cox, G. Cummins, M. P. Desmulliez, R. E. Clutton, K. L. Obstein, S. Cochran, and P. Valdastri, "Intelligent magnetic manipulation for gastrointestinal ultrasound," *Science Robotics*, vol. 4, no. 31, pp. 1–14, 2019.

[13] C. M. Heunis, Y. P. Wotte, J. Sikorski, G. P. Furtado, and S. Misra, "The armm system-autonomous steering of magnetically-actuated catheters: Towards endovascular applications," *IEEE Robotics and automation letters*, vol. 5, no. 2, pp. 704–711, 2020.

[14] Y. Kim, G. A. Parada, S. Liu, and X. Zhao, "Ferromagnetic soft continuum robots," *Science Robotics*, vol. 4, no. 33, p. eaax7329, 2019.

[15] Y. Kim, H. Yuk, R. Zhao, S. A. Chester, and X. Zhao, "Printing ferromagnetic domains for untethered fast-transforming soft materials," *Nature*, vol. 558, no. 7709, p. 274, 2018.

[16] T. Xu, J. Zhang, M. Salehizadeh, O. Onaizah, and E. Diller, "Millimeter-scale flexible robots with programmable three-dimensional magnetization and motions," *Science Robotics*, vol. 4, no. 29, p. eaav4494, 2019.

[17] G. Z. Lum, Z. Ye, X. Dong, H. Marvi, O. Erin, W. Hu, and M. Sitti, "Shape-programmable magnetic soft matter," *Proceedings of the National Academy of Sciences*, vol. 113, no. 41, pp. E6007 LP – E6015, oct 2016. [Online]. Available: http://www.pnas.org/content/113/41/E6007.abstract

[18] D. C. Rucker and R. J. Webster, “Statics and dynamics of continuum robots with general tendon routing and external loading,” *IEEE Transactions on Robotics*, 2011.

[19] R. J. Webster and B. A. Jones, “Design and Kinematic Modeling of Constant Curvature Continuum Robots: A Review,” *The International Journal of Robotics Research*, vol. 29, no. 13, pp. 1661–1683, jun 2010. [Online]. Available: https://doi.org/10.1177/0278364910368147

[20] R. J. Roesthuis and S. Misra, “Steering of Multisegment Continuum Manipulators Using Rigid-Link Modeling and FBG-Based Shape Sensing,” *IEEE Transactions on Robotics*, vol. 32, no. 2, pp. 372–382, 2016.

[21] R. Zhao, Y. Kim, S. A. Chester, P. Sharma, and X. Zhao, “Mechanics of hard-magnetic soft materials,” *Journal of the Mechanics and Physics of Solids*, vol. 124, pp. 244–263, 2019. [Online]. Available: http://www.sciencedirect.com/science/article/pii/S0022509618307646

[22] V. Q. Nguyen, A. S. Ahmed, and R. V. Ramanujan, “Morphing soft magnetic composites,” *Advanced Materials*, vol. 24, no. 30, pp. 4041–4054, 2012.

[23] W. Hu, G. Z. Lum, M. Mastrangeli, and M. Sitti, “Small-scale soft-bodied robot with multimodal locomotion,” *Nature*, vol. 554, no. 7690, p. 81, 2018.

[24] I. A. Seleem, H. El-Hussieny, and S. F. M. Assal, “Motion Planning for Continuum Robots: A Learning from Demonstration Approach,” in *2018 27th IEEE International Symposium on Robot and Human Interactive Communication (RO-MAN)*, 2018, pp. 868–873.

[25] M. T. Gillespie, C. M. Best, E. C. Townsend, D. Wingate, and M. D. Killpack, “Learning nonlinear dynamic models of soft robots for model predictive control with neural networks,” in *2018 IEEE International Conference on Soft Robotics (RoboSoft)*, 2018, pp. 39–45.

[26] M. Pfeiffer, C. Riediger, J. Weitz, and S. Speidel, “Learning soft tissue behavior of organs for surgical navigation with convolutional neural networks,” *International*

*Journal of Computer Assisted Radiology and Surgery*, vol. 14, no. 7, pp. 1147–1155, 2019. [Online]. Available: https://doi.org/10.1007/s11548-019-01965-7

[27] A. Madani, A. Bakhaty, J. Kim, Y. Mubarak, and M. R. K. Mofrad, "Bridging Finite Element and Machine Learning Modeling: Stress Prediction of Arterial Walls in Atherosclerosis," *Journal of Biomechanical Engineering*, vol. 141, no. 8, may 2019. [Online]. Available: https://doi.org/10.1115/1.4043290

[28] S. Nair, *Introduction to continuum mechanics.* Cambridge University Press, 2009.

[29] S. Jeon, A. K. Hoshiar, S. Kim, S. Lee, E. Kim, S. Lee, K. Kim, J. Lee, J.-y. Kim, and H. Choi, "Improving guidewire-mediated steerability of a magnetically actuated flexible microrobot," *Micro and Nano Systems Letters*, vol. 6, no. 1, p. 15, 2018. [Online]. Available: https://doi.org/10.1186/s40486-018-0077-y

[30] A. Z. Taddese, P. R. Slawinski, M. Pirotta, E. De Momi, K. L. Obstein, and P. Valdastri, "Enhanced real-time pose estimation for closed-loop robotic manipulation of magnetically actuated capsule endoscopes," *The International journal of robotics research*, vol. 37, no. 8, pp. 890–911, 2018.

[31] D. Son, S. Yim, and M. Sitti, "A 5-d localization method for a magnetically manipulated untethered robot using a 2-d array of hall-effect sensors," *IEEE/ASME Transactions on Mechatronics*, vol. 21, no. 2, pp. 708–716, 2015.

[32] F. Khan, A. Denasi, D. Barrera, J. Madrigal, S. Sales, and S. Misra, "Multi-core optical fibers with bragg gratings as shape sensor for flexible medical instruments," *IEEE sensors journal*, 2019.

[33] G. J. Vrooijink, M. Abayazid, and S. Misra, "Real-time three-dimensional flexible needle tracking using two-dimensional ultrasound," in *2013 IEEE International Conference on Robotics and Automation.* IEEE, 2013, pp. 1688–1693.

[34] Y. Li, J. Li, W. Li, and H. Du, "A state-of-the-art review on magnetorheological elastomer devices," *Smart materials and structures*, vol. 23, no. 12, p. 123001, 2014.

[35] L. B. Kratchman, T. L. Bruns, J. J. Abbott, and R. J. Webster, "Guiding elastic rods with a robot-manipulated magnet for medical applications," *IEEE Transactions on Robotics*, vol. 33, no. 1, pp. 227–233, Feb 2017.

[36] K. M. Popek, T. Hermans, and J. J. Abbott, "First demonstration of simultaneous localization and propulsion of a magnetic capsule in a lumen using a single rotating magnet," in *2017 IEEE International Conference on Robotics and Automation (ICRA)*, May 2017, pp. 1154–1160.

[37] P. R. Slawinski, A. Z. Taddese, K. B. Musto, K. L. Obstein, and P. Valdastri, "Autonomous retroflexion of a magnetic flexible endoscope," *IEEE Robotics and Automation Letters*, vol. 2, no. 3, pp. 1352–1359, July 2017.

[38] A. Azizi, C. C. Tremblay, K. Gagné, and S. Martel, "Using the fringe field of a clinical mri scanner enables robotic navigation of tethered instruments in deeper vascular regions," *Science Robotics*, vol. 4, no. 36, 2019.

# Chapter 3

# The Optimization Algorithm

**Chapter source:** P. Lloyd, G. Pittiglio, J. H. Chandler, and P. Valdastri, “Optimal design of soft continuum magnetic robots under follow-the-leader shape forming actuation,” 2020 International Symposium on Medical Robotics (ISMR), 2020, pp. 111–117.

## Abstract

We describe a novel paradigm for task-specific optimization of millimetre scale, magnetically actuated soft continuum robots for application in endoscopic procedures. In particular, we focus on a multi-segment, elastomeric manipulator whose magnetization and actuating field is optimized for follow-the-leader shape forming during insertion into a known environment. Optimization of length-wise magnetization profile, or *magnetic signature*, is performed in parallel with that of the actuating magnetic field for a range of desired shapes. We employ a rigid-link model for the mechanics of the manipulator and assume the ability to generate a controlled homogeneous magnetic field across the workspace. To demonstrate the efficacy of the proposed approach, we present our results against those generated via Finite Element Analysis (FEA). Moreover, we compare our proposed method with a traditional tip-driven system exhibiting fixed magnetization; demonstrating a 48% error reduction in shape forming capability. The presented approach is evaluated across three additional navigation scenarios, demonstrating potential as a design tool for soft magnetic medical robots.

## 3.1 Introduction

In the last few decades, much medical research and development has focused on minimally invasive diagnosis and treatment. We have seen the advent of technologies that can facilitate scare-less endoluminal inspection of the human body. In general this can improve patient outcomes through lower morbidity and reduced recovery times [1]. With the proliferation of minimally invasive procedures a number of technological challenges have arisen in relation to the tools involved. Specifically, there has been a need to reduce instrument size, increase dexterity, and improve safety during tissue interactions.

In summation, these challenges may be generally considered in relation to the tools' ability to effectively navigate through, and operate within, complex and tortuous environments. In pursuit of this capability researchers have extensively investigated the use of *continuum manipulators* [2]. These are generally characterised by high dexterity with some degree of shape control, making them highly suitable for application in minimally invasive diagnosis and treatment.

Although high dexterity is essential for navigation within complex environments, it is also important for safety and comfort to minimize inadvertent contact forces. For this reason, soft robots - with their elastomeric materials - have been proposed [3] and applied to surgical procedures [4]. A soft robot can rely on environmental interaction to provide shape forming forces without subjecting the patient to excessive discomfort or risk.

Enhanced shape forming of continuum robots, through higher controllable degrees of freedom, has the consequence of increasing their size. Indeed, across many actuation systems we can generally equate higher dexterity with a corresponding increase in size. An example of this, for tendon-driven manipulators, is the increase in number of tendons required as controlled degrees of freedom are increased [5]. Due to this restriction, much recent research has focused on *magnetically actuated* solutions [6; 7; 8]. In the case of magnetic actuation, dexterity is not directly correlated to size and miniaturization is no longer limited to very simple (one or two degree of freedom) shapes. Adversely, a corresponding relationship exists for magnets between maximum applicable force and their size. This can be counter-acted with the application of strong magnetic fields as in, for example, the Magnetic Resonance Imaging (MRI) fringe field detailed in [9].

As a consequence of the independence of size and dexterity, magnetic actuation has proven effective in endoscopic procedures [10; 11]. Single point [12], shape [13], multi-magnet [6; 7] and magnetic soft matter control [8] have all been investigated. One limitation of all of these approaches resides in sub-optimal magnetization profile - generally in the direction of motion - and focusing on magnetic field control only. This does not, in general, allow for minimized contact during navigation.

Inspired by [14; 15; 16; 17; 18], who demonstrate magnetic signature design for enhanced functionalities, we propose a novel procedure for optimal design of *magnetic soft tentacles* for endoscopic procedures. Starting from a known anatomical pathway, we optimize the tentacle magnetization along its length in conjunction with the instantaneous controlling magnetic field to minimize contact forces during insertion. An autonomous routine, based on a combination of rigid link [19] and magnetic modelling [20] has been designed to optimize the length-wise magnetization profile or *magnetic signature* of the tentacle. We consider the tentacle as being formed from multiple sections of magnetized elastomeric material operating under sequential insertion.

Following a detailed overview of the problem (Section 3.2), we present the proposed optimization strategy including simplifying assumptions (Section 3.3). The insertion process for the optimized multi-segment magnetic tentacle and controlling field is evaluated through implementation of rigid link and finite element simulations (Section 3.4). We assess our approach against a traditional tip-driven configuration, as well as verifying its efficacy over a range of navigation scenarios (Section 3.5).

## 3.2 Problem Formulation

Consider the problem of guiding a soft *tentacle* through a lumen, from an *insertion point* (I) to the *target point* (T) as depicted in Fig. 3.1. We assume the lumen shape is known from pre-imaging for example, and that the optimal (desired) path from I to T has been ascertained by means of either a manual or an automated path planning algorithm (e.g. [21]).

The aim in this case is to find the *magnetization* ($\mu_i$) of the $i$-th link ($L_i$) and the global *homogeneous magnetic field* ($B$) such that the magnetized tentacle conforms to a desired shape, minimizing contact with the environment. This is achieved through an optimization procedure, detailed in Section 3.3.3. The insertion process is considered to be step-wise; for each insertion step ($\delta T$) a new segment is introduced into the environment and its magnetization, along with the global homogeneous magnetic field $B(k\delta T)$, $k =$

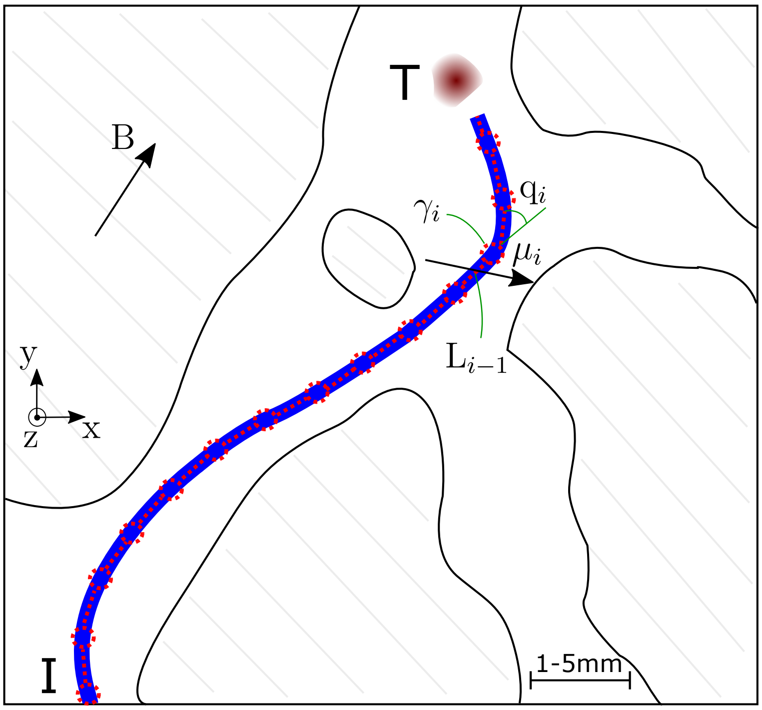

Figure 3.1: Example of navigation of magnetic tentacle in generic lumen, from insertion point (I) to target point (T). Approximate scale bar shown to give indication of magnitude

$0,\ 1,\ \cdots$, is optimized to produce the desired shape.

In the present work we do not consider a specific actuation system, rather we assume a pure homogeneous field is generated throughout the work-space. This assumption is intuitively valid for the case of coil-based actuation [20] and can also be made for sufficiently small work-spaces (relative to magnets' remanence) in permanent magnet based counterparts such as [10].

To achieve suitable optimization, a model of the mechanical response of the tentacle as it interacts with its actuating magnetic field is required. Since we are dealing with a soft continuum robot, full mechanical characterization is not straightforward, and has been an active topic of research [22]. Here we employ the *rigid-link model* as already proposed for magnetically actuated continuum robots in [19].

## 3.3 Magneto-mechanical Design

In the following section, the modeling approach applied to the magnetic tentacle shown in Fig. 3.1 is described; including the mechanical and magnetic properties and their interaction. For the presented study, a planar case is considered, however, this could be generalised to more complex 3D scenarios.

### 3.3.1 Mechanics

Consider the insertion of a magnetically active tentacle starting from the insertion point (I) shown in Fig. 3.1. At each time step $t = k\ \delta T,\ k = 0, 1, \cdots$, we assume a segment of length $\delta l$ is inserted into the environment. This process is assumed to be independent of the magnetic actuation, i.e. the tentacle is mechanically introduced into the environment and not driven via magnetic wrenches. This segment will be the $i$-th link $L_i$ of the continuum robot, connected to the link $L_{i-1}$ and $L_{i+1}$ by means of the *rotational joints* $\gamma_{i-1}$ and $\gamma_i$, respectively.

The $i$-th joint angle $q_i$ is defined as the angle between the link $L_{i-1}$ and $L_i$, as per the standard Denavit-Hartenberg (DH) convention [23].

At the $k$-th insertion step, the robot joint space can be described by $q^{(k)} = (q_1\ q_2\ \cdots\ q_k)^T$. We consider that a wrench $f_j \in \mathbb{R}^6$ is applied at the centre of the $j$-th link whose end position is

$$p_j = -\sum_{i=1}^{j} \prod_{k=1}^{i} \mathrm{rot}_z(q_k)\ \delta l\ e_2$$

where $\mathrm{rot}_z(\cdot)$ is the rotation around the $z$ axis and $e_r^{(s)} \in \mathbb{R}^s$ is the $r$-th element of the canonical basis of $\mathbb{R}^s$. For the sake of analytical simplicity we model components of the wrench which lie out of plane however these components do not play a role in the torque balance equation. Moreover, since we consider homogeneous magnetic field - hence, torque only - the location of the applied wrench along the link does not have effect on the results.

By considering the *differential kinematics* of the continuum manipulator [23], under the rigid-link assumption, the twist at the center of $L_j$ can be expressed as

$$\begin{pmatrix} v_j \\ \dot{\theta}_j \end{pmatrix} = \sum_{i=1}^{j} \begin{pmatrix} (\frac{1}{2}p_j - p_i) \times \delta l \; e_3^{(3)} \\ e_3^{(3)} \end{pmatrix} \dot{q}_i = J_j^{(k)} \dot{Q}_k,$$

with $\theta_j$ deflection of the $j$-th segment and $v_j = \frac{\dot{p}_j}{2}$. By stacking the Jacobians for the $j$-th link at insertion step $k$, as $J^{(k)^T} = \left( J_1^{(k)^T} \; J_2^{(k)^T} \; \cdots \; J_k^{(k)^T} \right)$, and considering the duality between differential kinematics and statics, we obtain

$$\tau^{(k)} = J^{(k)^T} f^{(k)}, \tag{3.1}$$

with $f^{(k)} = (f_1^T \; f_2^T \; \cdots \; f_k^T)^T$ being the wrench applied to each inserted link. The torque on the joints $\tau^{(k)}$, considering the tentacle's resting position $Q^{(k)} = 0_{k,0}$, with $0_{ij} \in \mathbb{R}^{i \times j}$ the zero vector, is

$$\tau^{(k)} = K^{(k)} Q^{(k)}, \tag{3.2}$$

where the stiffness matrix $K^{(k)}$ can be found from the mechanical characteristics of the material [19]. We assume, without loss of generality, that the stiffness is linear with respect to the joint variables. This assumption (which could be relaxed for the modelling of complex elastomeric behaviour and/or large deformation) is considered valid when $\delta l$ is chosen to be *sufficiently small* and, thus, each $q_i$ is small. Herein

$$K^{(k)} = \mathrm{diag}(\underbrace{EI \; EI \; \cdots \; EI}_{k \text{ times}}),$$

with $E$ Young modulus and $I$ second moment of area [24].

### 3.3.2 Magnetics

As introduced in Section 3.2, we consider the $i$-th link of the tentacle to have magnetization $\mu_i$, with respect to the link's reference frame. By considering the direct kinematics of the manipulator, in the global reference frame, we obtain

$$\overline{\mu}_i = \prod_{j=1}^{i} \mathrm{rot}_z(q_j)\mu_i.$$

In the case of our homogeneous field $B$, we obtain the wrench on the $i$-th link being [20]

$$f_i = \begin{pmatrix} 0_{3,1} \\ B \times \overline{\mu}_i \end{pmatrix} = \begin{pmatrix} 0_{3,1} \\ -\overline{\mu}_{i_\times} B \end{pmatrix},$$

with $(\cdot)_\times$ being the *skew operator*. We build the mapping from field to wrench as

$$S^{(k)} = \begin{pmatrix} 0_{3,3} \\ -\overline{\mu}_{k_\times} \\ 0_{3,3} \\ -\overline{\mu}_{k-1_\times} \\ \vdots \\ 0_{3,3} \\ -\overline{\mu}_{1_\times} \end{pmatrix}.$$

This, combined with (3.1) and (3.2), leads to the *magneto-mechanical static equilibrium*

$$K^{(k)}Q^{(k)} = J^{(k)^T}(S^{(k)}B(k\delta T) + G^{(k)}), \tag{3.3}$$

with the gravity vector $G^{(k)} = -mg^{(k)}$,

$$g^{(k)} = \left.\begin{pmatrix} e_2^{(6)} \\ e_2^{(6)} \\ \vdots \\ e_2^{(6)} \end{pmatrix}\right\} k \text{ times},$$

and $m$ the mass of each link.

### 3.3.3 Optimization

The fundamental step of the proposed approach lies in the optimization of the magnetization $\mu = \left(\mu_1^T \; \mu_2^T \; \cdots \; \mu_n^T\right)^T$ and the magnetic field $U = (B(0) \; B(1) \; \cdots \; B((n-1)\delta T))$. Herein, $n$ is the number of segments needed to reach the target (T).

With this aim, we define the system of equations of the magneto-mechanical equilibrium

$$\lambda = \begin{pmatrix} K^{(1)}Q^{(1)} - J^{(1)^T}(S^{(1)}B(0) + G^{(1)}) \\ K^{(2)}Q^{(2)} - J^{(2)^T}(S^{(2)}B(\delta T) + G^{(2)}) \\ \vdots \\ K^{(n)}Q^{(n)} - J^{(n)^T}(S^{(n)}B((n-1)\delta T) + G^{(n)}) \end{pmatrix}$$

and the vector of unknowns $x = (\mu^T \; U^T)^T$. We thus solve the minimization problem

$$\begin{aligned} \min_{x} \quad & ||\lambda|| \\ \text{s.t.} \quad & ||\mu_i|| = C, \; \forall i \end{aligned}$$

by using the Matlab function `fmincon` [25], with the *interior point algorithm.*

Constraints are applied with consideration of fabrication simplicity. Specifically, we constrain the magnitude of magnetization to be constant in each segment representing a fixed proportion of magnetic doping throughout all magnetically active sections of the manipulator.

## 3.4 Numerical Analysis

In order to assess the strength of the proposed approach we performed a Finite Element Analysis (FEA) representing four distinct scenarios; different configurations of obstacles in a planar environment. We considered a desired path ($\Gamma_d$) connecting the insertion point with the target point - the origin and the green circle respectively in Figs. 3.2, 3.3, 3.4, 3.5, 3.6. The sample path was generated considering four segments of equal length $\delta l = 14mm$. This length gives sufficient flexibility to exhibit length-wise shape forming without being so flexible as to violate the assumptions of linear elasticity; we noticed breakdown in the validity of the rigid link assumption for $q_i > 15^o$.

The algorithm described in Section 3.3 was applied to determine the case-specific magnetization ($\mu_i$ for the $i$-th segment) and the magnetic field at each time step ($B$). In parallel to our rigid-link model (see Section 3.3.1), a full continuum mechanics FEA model was constructed using the commercial software package COMSOL multiphysics v5.4 (COMSOL AB, Stockholm, Sweden). This simulation employed the solid mechanics and electro-magnetics modules connected via the Maxwell surface stress tensor. The plane strain assumption was utilised and the 78,000 node manually assembled mesh was converged using the Newton-Raphson iterative method.

The tentacle radius was fixed at 1 mm. Each of the four identical 14 mm long segments was assembled in series from 7 mm of magnetically unreactive silicone (Ecoflex 00-30, Young Modulus 69 kPa, density 1070 $kgm^{-3}$) and 7 mm of magnetically reactive silicone (Young Modulus 80 kPa, density 1400 $kgm^{-3}$, remanent magnetization 107 mT). These properties were calculated assuming equal proportions by weight of silicone and Neodymium-iron-boron (NdFeb) in the doped segments of the tentacle [8]. Notice that, even if the rigid-link model used in the optimization does not, the COMSOL simulation considers magnetic interaction between reactive segments. This numerical simulation provides a series of derived tentacle shapes ($\Gamma$) which we assumed to be an accurate representation of reality. The Young modulus and density of the arbitrary homogenised material represented by the rigid link model are weighted means of those in the numerical model.

## 3.5 Results

In order to compare the performance of the rigid link optimization with previously proposed techniques applied to magnetically actuated soft continuum robots [8] we established a basis for comparison. This comparison is made for the first arrangement of obstacles only; Scenario A* versus Scenario A. To this end, an initial scenario (Scenario

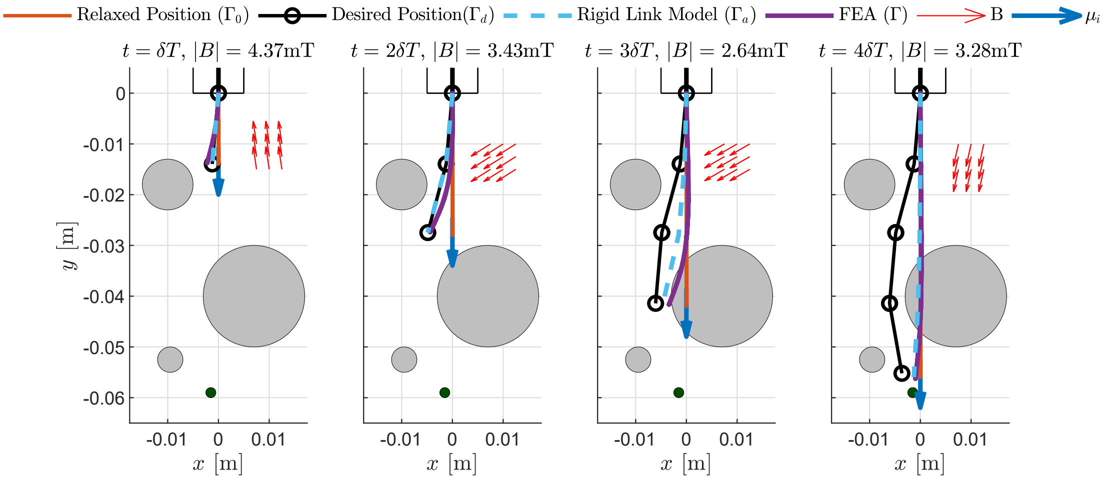

Figure 3.2: Scenario A*. The tip driven catheter with optimized magnetic field showing collision at $t = 4\delta T$

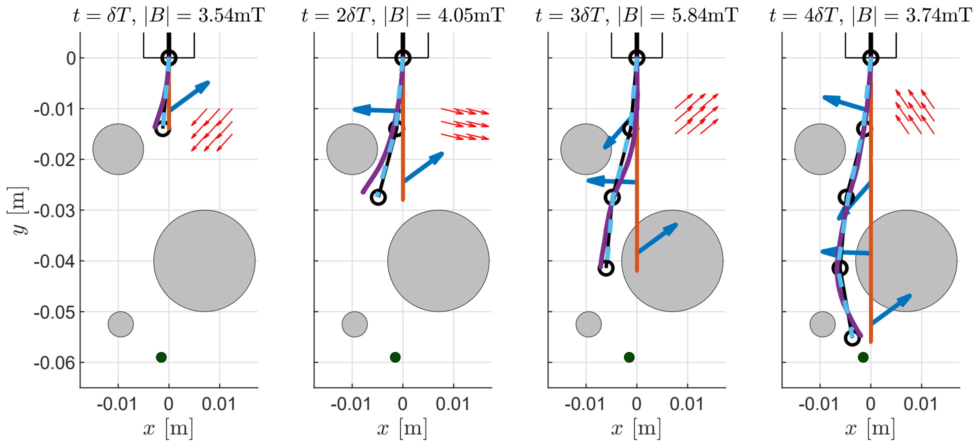

Figure 3.3: Scenario A. The fully shape forming tentacle shown successfully navigating an identical environment to Scenario A*. For legend see Fig. 3.2.

A*) was considered with a fully constrained magnetization representing a conventional tip driven continuum manipulator; optimized for field only. This is reported in Fig. 3.2 where the impact with an interstitial obstacle (the grey circles in, for example, Fig. 3.2) can be clearly observed. This approach would therefore rely on environmental interaction to navigate such a pathway, as shown in [8]. Conversely, as detailed in Fig. 3.3, the proposed method, by design, eliminates contact and demonstrates obstacle avoidance.

To demonstrate the diversity of the proposed methodology, we presented three further cases of successful obstacle avoidance in Figs. 3.4, 3.5 and 3.6. All four of the evaluated scenarios successfully avoid collision. however Scenario C (Fig. 3.5), due to its more

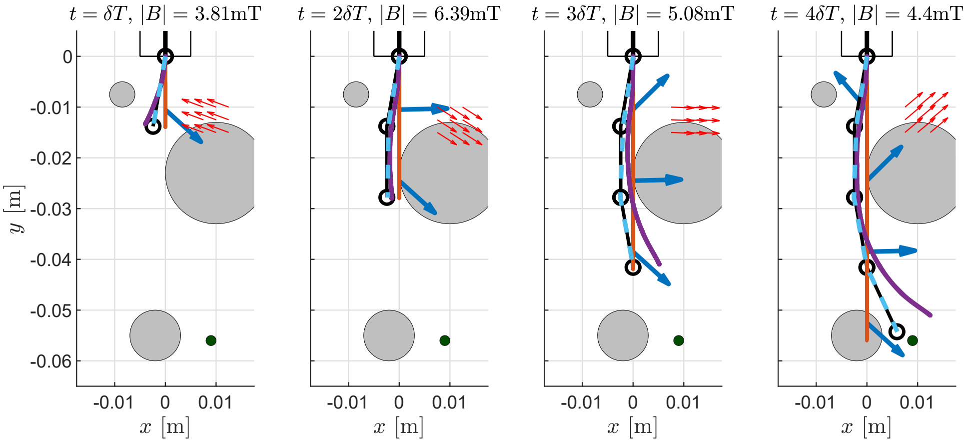

Figure 3.4: Scenario B. An alternative arrangement of obstacles

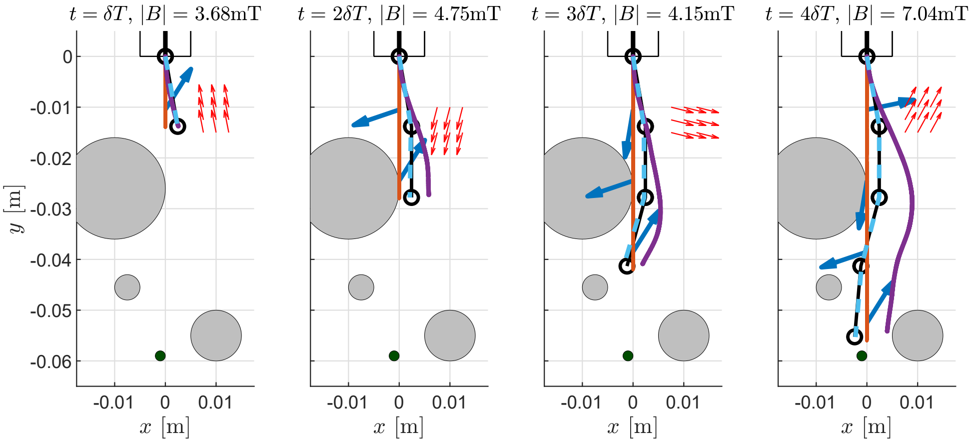

Figure 3.5: Scenario C. The constraint of a homogeneous field appears prohibitive for this more convoluted path

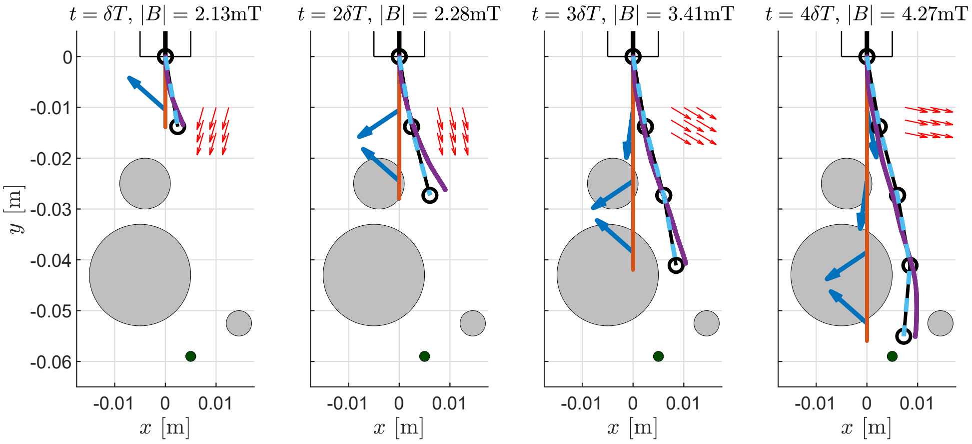

Figure 3.6: Scenario D. A fourth arrangement of obstacles demonstrating a high level of reconciliation between rigid link and FEA models

Table 3.1: A Comparison of RMS Errors (*mm*) for the tip driven catheter (A*) and the fully magnetized tentacle in four different topological scenarios (A, B, C and D). Row 3 also shows the absolute error in final tip position (*mm*)

| | **Scenario A*** | | **Scenario A** | | **Scenario B** | | **Scenario C** | | **Scenario D** | |
|---|---|---|---|---|---|---|---|---|---|---|
| | $\Gamma_d - \Gamma$ | $\Gamma_d - \Gamma_a$ | $\Gamma_d - \Gamma$ | $\Gamma_d - \Gamma_a$ | $\Gamma_d - \Gamma$ | $\Gamma_d - \Gamma_a$ | $\Gamma_d - \Gamma$ | $\Gamma_d - \Gamma_a$ | $\Gamma_d - \Gamma$ | $\Gamma_d - \Gamma_a$ |
| **Tip Deflection** | **2.0** | 1.4 | **2.0** | 0.14 | 4.3 | 0.10 | 4.0 | 0.38 | 2.2 | 0.02 |
| **Full-shape Deflection** | **2.5** | 1.97 | **1.3** | 0.19 | 2.2 | 0.17 | 3.1 | 0.23 | 1.2 | 0.03 |
| **Final Tip Position** | **2.7** | 2.34 | **1.7** | 0.04 | 6.6 | 0.10 | 6.4 | 0.16 | 2.3 | 0.01 |

convoluted desired shape exhibits errors in magnitude of deflection. The requested profile in Scenario C changes direction mid-length and as a consequence of this complication the rigid link optimization fails to produce an accurate replica of the FEA. Whilst the deflected shape is produced, accuracy is lost in the magnitude of deflection. This is due to the constraint of a homogeneous field; were field gradients and their associated forces permitted, the optimization may more accurately replicate this more convoluted desired shape.

Table 3.1 reports the Root Mean Square (RMS) of errors in deflection in the $x$ axis between the desired path and the FEA result (Left hand sub-column; $\Gamma_d - \Gamma$) and between the desired path and the rigid link model result (Right hand sub-column; $\Gamma_d - \Gamma_a$). Errors are presented for each of the five scenarios in Figs 3.2, 3.3, 3.4, 3.5 and 3.6 respectively. The first of these Scenarios (A*) being the purely tip driven example and the subsequent four scenarios being our fully shape forming analyses with various obstacle locations.

Errors for each of these five illustrated scenarios are presented in three distinct forms represented by the rows of Table 3.1. In row 1 the error in the position of *just* the tip is shown, the average is taken of the tip position at each of the four insertion time-steps

$$\epsilon = \sqrt{\frac{1}{T}\sum_{t=1}^{T}(p_{x,d}^{(t)} - p_x^{(t)})^2}$$

with $p_{x,d}^{(t)}$ *desired* $x$ position of the tip at time $t$, $p_x^{(t)}$ the same for *derived* value and T the total number of time steps.

In row 2 we show the error in the position of *all* of the segment centres at every time step

$$\epsilon = \sqrt{\frac{1}{NT}\sum_{t=1}^{T}\sum_{i=1}^{N}(p_{x,d}^{(i,t)} - p_x^{(i,t)})^2}$$

with $p_{x,d}^{(i,t)}$ *desired* $x$ position of the $i$-th segment at time $t$, $p_x^{(i,t)}$ the same for *derived* value and N the total number of segments. This second row provides a suitable proxy for the error in the shape forming capability of the tentacle. Finally, in row 3 we show the absolute error (in mm) of the finishing tip position.

From this we can make an objective comparison of the tip driven example in Scenario A* against our shape forming example in Scenario A. This comparison is shown in boldface in Table 3.1. We can see that the error in the tip position does not improve when a full length-wise magnetization is employed. For the full body shape error in row 2, however, an error reduction of 48% is shown. This reduction is intuitively apparent, as the tip driven system has no capacity to shape form as is observable in Fig. 3.2. For the shape forming tentacle, across all four topographies we observe an RMS error between desired and derived segment positions of 2.1mm (3.7% of manipulator length) with a standard deviation of 0.9mm (1.6% of manipulator length).

Further to this, across all four shape forming Scenarios (Figs. 3.3, 3.4, 3.5 and 3.6) it is observed that the rigid link model exhibits very close adherence to the desired shape. This level of accuracy is not replicated when the results of the rigid link model are processed in the FEA. From this we conclude that there remain inaccuracies in the assumptions of the rigid link model which are exposed by the FEA. These inaccuracies most notably relate to link length and the linear pseudo-spring constant. We intend to address and minimize these in our future work.

## 3.6 Conclusions

In this work we described a novel approach for the parallel optimization of magnetic signature and actuating field for our soft continuum magnetized manipulators or *magnetic tentacles*. We focused on the problem of minimizing interaction with the environment and hence increasing patient safety and comfort. The proposed approach relies on magneto-mechanical modelling of the static equilibrium of the continuum manipulator. This system is based on a combination of magnetic dipole and rigid-link mechanical models. By considering this equilibrium, we performed an off-line optimization procedure which outputs the optimal magnetization profile of the tentacle and the attendant actuating fields at each step of insertion. We defined the application as a planar case under the assumption that a homogeneous magnetic field can be generated across the work-space.

We reported numerical results from the FEA for four different obstacles settings. We also computed the comparison, for the first of these settings, of non-optimized magnetization - the tip driven manipulator. This resembles previously proposed approaches in the literature [7; 9; 8]. We showed that the proposed solution achieves significantly improved results in terms of follow-the-leader path following accuracy and obstacle avoidance.

Our future work will be devolved to improvements and developments in the rigid link modelling assumptions, applying the proposed method to a 3D case and investigating cases of non-homogeneous magnetic field. Moreover, we will analyse and report experimental studies.

# Bibliography

[1] K. A. Hausegger, P. Schedlbauer, H. A. Deutschmann, and K. Tiesenhausen, "Complications in endoluminal repair of abdominal aortic aneurysms," *European journal of radiology*, vol. 39, no. 1, pp. 22–33, 2001.

[2] J. Burgner-Kahrs, D. C. Rucker, and H. Choset, "Continuum Robots for Medical Applications: A Survey," pp. 1261–1280, 12 2015.

[3] D. Trivedi, C. D. Rahn, W. M. Kier, and I. D. Walker, "Soft robotics: Biological inspiration, state of the art, and future research," *Applied Bionics and Biomechanics*, vol. 5, no. 3, pp. 99–117, 2008.

[4] M. C. Yip, J. A. Sganga, and D. B. Camarillo, "Autonomous Control of Continuum Robot Manipulators for Complex Cardiac Ablation Tasks," *Journal of Medical Robotics Research*, vol. 02, no. 01, p. 1750002, 2017.

[5] T. Kato, I. Okumura, H. Kose, K. Takagi, and N. Hata, "Tendon-driven continuum robot for neuroendoscopy: validation of extended kinematic mapping for hysteresis operation," *International Journal of Computer Assisted Radiology and Surgery*, vol. 11, no. 4, pp. 589–602, 4 2016.

[6] J. Edelmann, A. J. Petruska, and B. J. Nelson, "Magnetic control of continuum devices," *International Journal of Robotics Research*, vol. 36, no. 1, pp. 68–85, 2017.

[7] S. Jeon, A. K. Hoshiar, K. Kim, S. Lee, E. Kim, S. Lee, J.-y. Kim, B. J. Nelson, H.-J. Cha, B.-J. Yi, and H. Choi, "A Magnetically Controlled Soft Microrobot Steering a Guidewire in a Three-Dimensional Phantom Vascular Network," *Soft Robotics*, vol. 6, no. 1, pp. 54–68, 10 2018. [Online]. Available: https://doi.org/10.1089/soro.2018.0019

[8] Y. Kim, G. A. Parada, S. Liu, and X. Zhao, "Ferromagnetic soft continuum robots," *Science Robotics*, vol. 4, no. 33, p. eaax7329, 8 2019. [Online]. Available: http://robotics.sciencemag.org/content/4/33/eaax7329.abstract

[9] A. Azizi, C. C. Tremblay, K. Gagné, and S. Martel, "Using the fringe field of a clinical MRI scanner enables robotic navigation of tethered instruments in deeper vascular regions," *Science Robotics*, vol. 4, no. 36, p. eaax7342, 11 2019. [Online]. Available: http://robotics.sciencemag.org/content/4/36/eaax7342.abstract

[10] L. Barducci, G. Pittiglio, J. C. Norton, K. L. Obstein, and P. Valdastri, "Adaptive Dynamic Control for Magnetically Actuated Medical Robots," *IEEE Robotics and Automation Letters*, vol. 4, no. 4, pp. 3633–3640, 7 2019.

[11] J. C. Norton, P. R. Slawinski, H. S. Lay, J. W. Martin, B. F. Cox, G. Cummins, M. P. Y. Desmulliez, R. E. Clutton, K. L. Obstein, and S. Cochran, "Intelligent magnetic manipulation for gastrointestinal ultrasound," *Science Robotics*, 2019.

[12] G. Pittiglio, L. Barducci, J. W. Martin, J. C. Norton, C. A. Avizzano, K. L. Obstein, and P. Valdastri, "Magnetic Levitation for Soft-Tethered Capsule Colonoscopy Actuated With a Single Permanent Magnet: A Dynamic Control Approach," *IEEE Robotics and Automation Letters*, vol. 4, no. 2, pp. 1224–1231, 2019.

[13] L. B. Kratchman, T. L. Bruns, J. J. Abbott, and R. J. Webster, "Guiding Elastic Rods With a Robot-Manipulated Magnet for Medical Applications," *IEEE Transactions on Robotics*, vol. 33, no. 1, pp. 227–233, 2017.

[14] S. Floyd, C. Pawashe, and M. Sitti, "An untethered magnetically actuated micro-robot capable of motion on arbitrary surfaces," in *2008 IEEE International Conference on Robotics and Automation*, 2008, pp. 419–424.

[15] W. Hu, G. Z. Lum, M. Mastrangeli, and M. Sitti, "Small-scale soft-bodied robot with multimodal locomotion," *Nature*, vol. 554, p. 81, 1 2018. [Online]. Available: https://doi.org/10.1038/nature25443http://10.0.4.14/nature25443https://www.nature.com/articles/nature25443#supplementary-information

[16] G. Z. Lum, Z. Ye, X. Dong, H. Marvi, O. Erin, W. Hu, and M. Sitti, "Shape-programmable magnetic soft matter," *Proceedings of the National Academy of Sciences*, vol. 113, no. 41, pp. E6007 LP – E6015, 10 2016. [Online]. Available: http://www.pnas.org/content/113/41/E6007.abstract

[17] Y. Kim, H. Yuk, R. Zhao, S. A. Chester, and X. Zhao, "Printing ferromagnetic domains for untethered fast-transforming soft materials," *Nature*, vol. 558, no. 7709, pp. 274–279, 2018. [Online]. Available: https://doi.org/10.1038/s41586-018-0185-0

[18] R. Zhao, Y. Kim, S. A. Chester, P. Sharma, and X. Zhao, "Mechanics of hard-magnetic soft materials," *Journal of the Mechanics and Physics of Solids*, vol. 124, pp. 244–263, 2019. [Online]. Available: http://www.sciencedirect.com/science/article/pii/S0022509618307646

[19] V. K. Venkiteswaran, J. Sikorski, and S. Misra, "Shape and contact force estima-

tion of continuum manipulators using pseudo rigid body models," *Mechanism and Machine Theory*, vol. 139, pp. 34–45, 2019.

[20] S. Salmanipour and E. Diller, "Eight-Degrees-of-Freedom Remote Actuation of Small Magnetic Mechanisms," in *2018 IEEE International Conference on Robotics and Automation (ICRA)*, 2018, pp. 3608–3613.

[21] C. Baykal, C. Bowen, and R. Alterovitz, "Asymptotically optimal kinematic design of robots using motion planning," *Autonomous Robots*, vol. 43, no. 2, pp. 345–357, Feb 2019. [Online]. Available: https://doi.org/10.1007/s10514-018-9766-x

[22] R. J. Webster and B. A. Jones, "Design and kinematic modeling of constant curvature continuum robots: A review," *International Journal of Robotics Research*, vol. 29, no. 13, pp. 1661–1683, 2010.

[23] B. Siciliano, L. Sciavicco, L. Villani, and G. Oriolo, *Robotics: Modelling, Planning and Control.* Springer Publishing Company, Incorporated, 2010.

[24] D. C. Rucker and R. J. I. Webster, "Statics and Dynamics of Continuum Robots With General Tendon Routing and External Loading," *IEEE Transactions on Robotics*, vol. 27, no. 6, pp. 1033–1044, 2011.

[25] "Matlab optimization toolbox," version R2018b, the MathWorks, Natick, MA, USA.

# Chapter 4

# Fibre Reinforcement

**Chapter source:** P. Lloyd, Z. Koszowska, M. Di Lecce, O. Onaizah, J. H. Chandler, and P. Valdastri, "Feasibility of fiber reinforcement within magnetically actuated soft continuum robots," Frontiers in Robotics and AI, vol. 8, 2021.

## Abstract

Soft continuum manipulators have the potential to replace traditional surgical catheters; offering greater dexterity with access to previously unfeasible locations for a wide range of interventions including neurological and cardiovascular. Magnetically actuated catheters are of particular interest due to their potential for miniaturization and remote control. Challenges around the operation of these catheters exist however, and one of these occurs when the angle between the actuating field and the local magnetization vector of the catheter exceeds 90 degrees. In this arrangement, deformation generated by the resultant magnetic moment acts to *increase* magnetic torque, leading to potential instability. This phenomenon can cause unpredictable responses to actuation, particularly for soft, flexible materials. When coupled with the inherent challenges of sensing and localization inside living tissue, this behavior represents a barrier to progress. In this feasibility study we propose and investigate the use of helical fiber reinforcement within magnetically actuated soft continuum manipulators. Using numerical simulation to explore the design space, we optimize fiber parameters to enhance the ratio of torsional to bending stiffness. Through bespoke fabrication of an optimized helix design we validate a single, prototypical two-segment, 40 mm X 6 mm continuum manipulator demonstrating a reduction of 67% in unwanted twisting under actuation.

## 4.1 Introduction

Elastomeric soft continuum manipulators (CMs) represent a promising and highly active research area among the soft robotics community [1]. A major subset of these robots are magnetically actuated, tip driven CMs [2] [3] which offer the potential to fulfill and enhance the role of the surgical catheter. Magnetic CM's are popular due to their extrinsic actuation, uniquely offering near limitless potential for miniaturization [4] [5]. The concept of a shape forming soft magnetic robot was introduced for an untethered application in [6]. This was developed into a tethered 'cilium-like' manipulator in [7] and further specialized to catheter-like shapes in [8].

The appeal of the shape forming CM (over tip-driven approaches) lies in the higher dexterity of motion, offering a potentially dramatic reduction in uncomfortable and sometimes damaging anatomical contact forces during navigation within the body. This is of particular relevance for applications which require large bending deformation such as gastrointestinal and endovascular interventions [4]. Full shape-forming can allow for better lumen-following and thus a reduction in friction; permitting the use of softer materials. In order to achieve minimal contact navigation, the lengthwise magnetization profile of the CM and the applied actuating fields must be specifically configured.

Key to the development of the shape forming magnetic CM is the ability to support unstable combinations of magnetization and applied field (illustrated in Figure 6.1 and demonstrated in the supporting video). A combination of diverse magnetic signatures [7] and time-variant actuating fields [9] will inevitably create obtuse angles of actuation. Such obtuse angles will also unavoidably occur in the case that actuation is generated via external permanent magnets (e.g. [10]) which cannot be turned off and must transition from one field to another. These modes of actuation represent a promising option in terms of efficient generation of a clinically relevant workspace but unwanted twist in this situation could potentially disrupt a navigation to a dangerous degree. Large angles between the CM magnetization and the applied field produce an 'inverted pendulum' instability. The CM will then inevitably twist about its long axis (z-axis in Figure 6.1) in a search for the minimum energy pose. An example of this behavior is shown in Figure 6.2. Theoretically, closed loop control strategies such as the adaptive dynamic control demonstrated in [11] could be employed to counteract this instability. However, this solution would prove highly impractical for real life applications due to the challenges of monitoring and sensing within the human body, particularly with reference to magnetically actuated tools [12], [13]. A further alternative to the eradication of twisting would

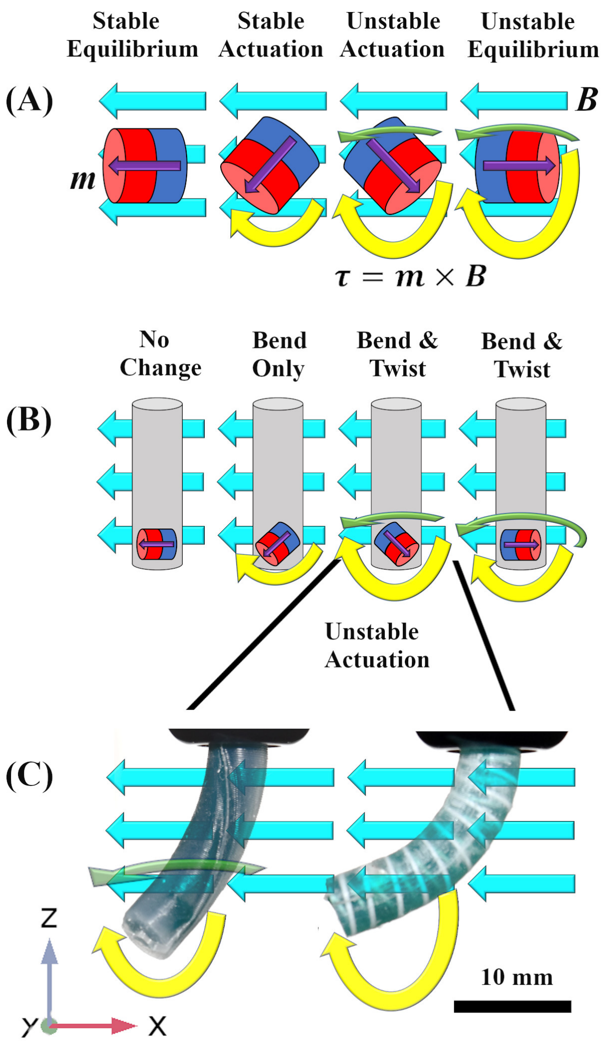

Figure 4.1: **(A)** Magnets in free space subject to a homogeneous actuating field $[-B_x\ 0\ 0]$ (turquoise arrows) and with magnetization $[m_x\ 0\ m_z]$ (purple arrows). As actuation lies in the x-z plane, theoretically, torque acts only about the y axis (yellow arrows) and is zero in the unstable equilibrium position. In practice, due to the inverted pendulum instability, torque exists about both z (green arrows) and y axes. Unstable modes of actuation also produce magnetic torque which increases with deflection. **(B)** Once embedded in a CM these unstable torques translate as both bending and twisting deformations. **(C)** Photographs from experimental actuation; the unreinforced sample on the left succumbs to the twisting instability about the z-axis. The reinforced sample on the right constrains the unstable twisting mode of actuation resulting in larger magnetic torque in the desired, bending, mode of deflection.

be to incorporate axial rotation as a modeled and controlled degree of freedom. This option would add to the complexity of the robot mechanics and would also contribute some out-of-plane manipulability. For the purposes of this investigation we are interested in maximizing in-plane bending deformation and as such we attempt to focus magnetic torque into the bending primitive and not lose energy in twisting.

One potential solution for improving open-loop control of these soft robots is to produce an anisotropic elasticity distribution by reinforcing the elastomer with higher stiffness fibers in order to restrict torsion whilst still permitting bending. This approach has parallels with organically evolved systems such as the collagen fiber reinforcing of the earthworm and related invertebrates, frequently referenced by the soft robotics community [14]. Following this concept, Kreig and Mohseni [15] investigated high deformation anisotropic strain restriction and the geometric arrangement of fibers in elastomeric sheets. The commonly employed Mckibben artificial muscle [16] consists of a pneumatic bladder providing a uniform hydrostatic pressure and strain restricting fibers capable of producing a range of motion primitives [17], [18]. More recently fluidic elastomer actuators have been developed and extensively exploited to offer a diverse range of pre-programmed mechanical responses to pneumatic pressure [19], [20]. Strain restriction has proved highly effective for soft pneumatic actuators, however, this approach has yet to be applied within the field of magnetic CM research.

In this preliminary study we demonstrate the application of strain-limiting fiber reinforcement within magnetically actuated soft CMs for improved open-loop actuation stability.

*Note in response to feedback during Viva, not included in original publication: The legitimate observation that NdFeB magnets are not soft and therefore the claim that this CM is fully soft isn't technically accurate. The design principle could readily be generalized to a fully soft robot by exploiting magnetically doped elastomers but the robot we present here exhibits rigid components encased in soft matter.*

Magnetic CMs have their own specific challenges, notably, small-scale manufacturing, small actuation wrenches and unique input instabilities. Here we present a numerical analysis of the potential usefulness of fiber reinforcement which has previously never been proposed or explored. Our experimental work is for validation purposes only and significant development will be required particularly around fabrication and control before we can perform a full experimental analysis.

The specific application being considered is a multi-segment shape forming CM, or *ten-*

*tacle*, with multiple magnetic elements as introduced in [8]. Here we demonstrate using a single prototypical 2-segment design, as shown in the supporting video, which represents a subset of the full shape forming CM. The workflow through the paper is as follows: In Section 4.2 we set out our goals and research methods. In Section 4.3 we define the underlying theory behind the magnetically actuated elastomeric catheter and our associated numerical model. In Section 4.4 we present the results of our single segment optimization and in Section 4.5 we extend the study into a multi-segment design including fabrication and experimental evaluation. We conclude and discuss in Section 4.6.

## 4.2 Problem Definition

An algorithm for the selection of a magnetization profile and actuating fields for a fully shape forming catheter was demonstrated, in a virtual environment, in [9]. The contribution of this work was to develop an optimization routine to derive specific magnetization profiles and time variant actuating fields to achieve follow-the-leader motion without imparting contact forces on the surrounding environment during navigation. One unavoidable outcome of this insertion process is a number of potentially unstable actuation arrangements. Referring to Figure 6.2, it can be observed in the second time step ($t_2$), the field associated with the lower of the two fixed magnets creates an obtuse angle with the actuating field. This condition *could* be specified as a parameter to be minimized (or excluded) in any optimization routine, however, the wide range of magnetization directions required to achieve any practically useful desired profile will inevitably generate such problems, particularly as the number of magnetized segments increases. The consequence of this instability is often catheter twist about the lower resistance z axis; this twisting can be observed in the unreinforced samples of both Figures 6.1 and 6.2 and the supporting video. This twisting is highly unpredictable and thus extremely difficult to simulate.

The objective of our work is to minimize the twisting primitive whilst maximizing the bending primitive, thus allowing practicable shape forming under a wider range of mag-

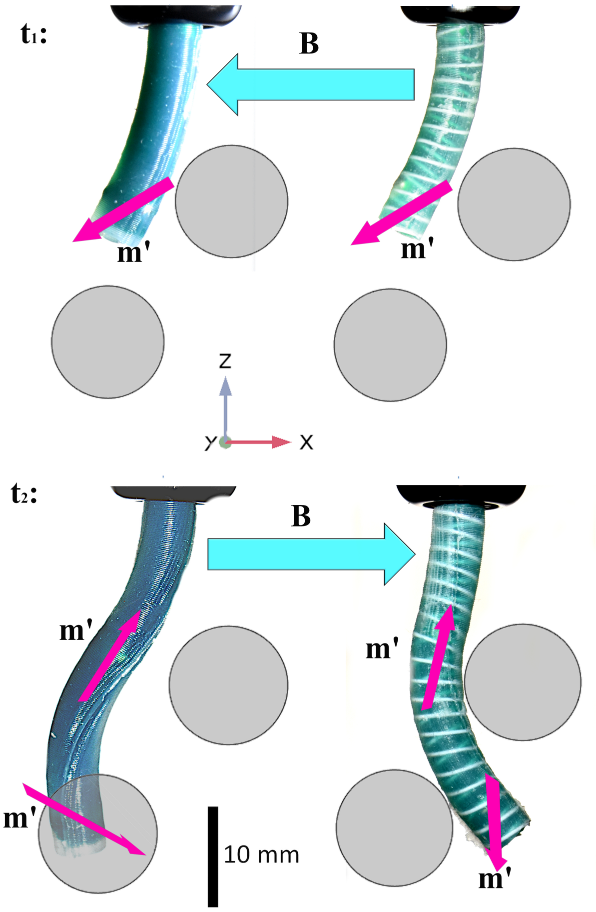

Figure 4.2: A minimal reproducible example of the impact of magnetic instability arising during manipulator navigation (as introduced in [9]). Specific magnetization profiles and time variant actuating fields achieve follow-the-leader motion without imparting contact forces on the surrounding environment. Here, deformed magnetization vectors (**m'**) are shown as purple arrows and applied fields (**B**, which change with respect to time) as turquoise (referential magnetizations are omitted to avoid clutter but are shown in the supporting video and in Section 4.5). The range of magnetization vectors required to achieve desired profiles generates unavoidable instabilities where the angle between **m** and **B** is obtuse. As can be seen bottom left, the unreinforced manipulator is prone to twist about the, lower resistance, local z-axis causing a loss of desired deformation; this twist is also clearly shown in the supporting video. If the manipulator was rotated 180° about global z for the second step of the navigation, the twisting torque would disappear but the bending torque about the lower magnet in the deformed state would also diminish such that the desired manipulator shape could not be achieved. In the reinforced specimen this twisting is minimized and deformation is focused about the y axis thus achieving the required contact free navigation. In this example, obstacles are represented by 2D background images placed in order to illustrate the objective.

netization - magnetic field conditions. There are many potential solutions to the general problem of twist minimization in CMs but we are constrained by certain application specific requirements. In order to preserve the softness and malleability of the manipulator,

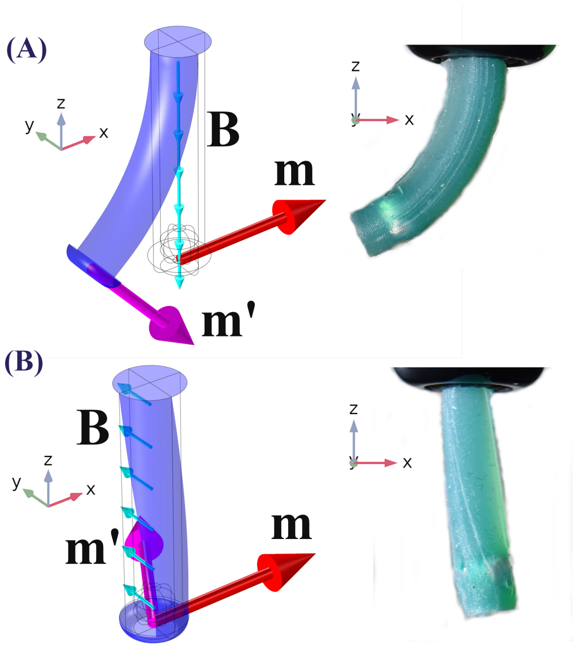

Figure 4.3: Pure bending about $y$ (**A**) and pure twisting about $z$ (**B**). The unreinforced Single Segment demonstrating the two non-trivial motion primitives (Pure bending about x and y are characteristically identical). On the left are isometric views of numerical simulations and on the right, planar (x-z) images of unreinforced prototypes. Referential magnetization vectors (**m**) are shown as red arrows, deformed magnetization vectors (**m'**) as purple and applied fields (**B**) as turquoise. Simulations recreated experimental results for the range $-20mT \leqslant B \leqslant 20mT$ with errors (mean ± standard deviation) of $3.6° \pm 2.7°$ demonstrating accuracy of the magnetic and material modeling assumptions.

and given the very low wrenches involved, we must employ soft, flexible reinforcing material in a sparse manner to produce anisotropic response to actuation. Specifically, we are attempting to minimize helical strain whilst allowing axial strain using only soft material. As such, our proposed solution to this multivariate problem, as inspired by [15], [16], [18] and [19] uses a double (and therefore symmetrical) helix of reinforcing fiber.

To quantify prospective designs, we established baseline tests using a Finite Element (FE) simulation of a 20 mm long x 6 mm diameter elastomeric catheter as shown in Figure 4.3. A single 3.2 mm x 3.2 mm cylindrical permanent magnet (PM) is embedded at the tip (PM's center 2 mm from the distal end) and the catheter is secured at its proximal end. The axis of magnetization of the PM was aligned in the positive $x$ direction as indicated by the red arrows in Figure 4.3. The bending primitive was tested by applying a uniform magnetic field, **B**, in the negative $z$ direction (Figure 4.3**A**). This actuating field generates a magnetic moment about the positive $y$ axis and thus results in pure bend. The same sample, when subject to a **B** field in the positive $y$ direction (Figure 4.3**B**), generates a magnetic moment about the positive $z$ axis and thus results in pure twist. With these test cases we separate the two deformation primitives which, in most realistic states, will co-exist. We use this separation to assess the relative susceptibility of a range of designs to the two primitives before they are combined in experimental prototypes.

Evaluating designs using FE simulation allows exploration of a wide range of design properties. Here we explore variations in elastic modulus of elastomer ($E_{silicone}$), filament diameter of reinforcing fibers ($d$), fiber angle ($\theta_H$) and number of helices ($N$). The samples shown in Figure 4.3 are unreinforced and these results constitute the baseline, or $N = 0$, result. We explore the design space with the underlying objective of determining an arrangement of fibers which constrain twisting without excessively constraining bending.

## 4.3 Modelling and Simulation

### 4.3.1 Material Model

We consider a soft catheter fabricated from elastomeric material (Ecoflex00-30, Smooth-On, USA) with strain limiting fibers made from Polylactic acid (PLA) (Material 1613, Ultimaker, Netherlands), both with readily available material properties. The reinforcing fibers are assumed to be linearly elastic and are thus represented in the numerical model by the two constants; elastic modulus $E_{PLA} = 2.4$ GPa and Poisson ratio $v = 0.4$. Due to the large elastic deformation experienced by the catheter we represent the silicone using an isotropic, strain energy based hyperelastic model. The commonly employed Yeoh model, which represents a trucation of the Rivlin power series to the 3rd order for only the first principle stretch [21] and [22], is represented by:

$$W = \sum_{i=1}^{n} C_i(\bar{I}_1 - 3)^i + \frac{1}{2}\kappa(J-1)^2 \tag{4.1}$$

where $W$ is Strain energy, $n$=3, is the order of the model, $\kappa$, is bulk modulus, $\bar{I}_1$ is the first principle stretch (not to be confused with second moment of area) and $J$ is the Jacobian determinant of the deformation gradient tensor - the measure of compressibility. The choice of model and parameters were based on the work of [23] who conclude that the Yeoh model with parameters $C_1$ = 17000 Pa, $C_2$ = -200 Pa, $C_3$ = 23 Pa and $\kappa$ = 300 kPa gives the most accurate representation of Ecoflex00-30 for strains up to 100%.

### 4.3.2 Magnetic Model

From Maxwell's third equation, $\nabla.\mathbf{B} = 0$; divergence of a magnetic field must always be zero. From the fourth equation for a current-free field $\nabla\times\mathbf{B} = 0$; curl must also be zero. From the Lorentz force, a magnetic dipole moment $\mathbf{m}$ will be pulled in the direction of any spatial gradient of $\mathbf{B}$ with a force $\mathbf{F} = (\mathbf{m}.\nabla)\mathbf{B}$. That same magnetic dipole will also experience a resultant torque, linearly proportional to applied field strength $\boldsymbol{\tau} = \mathbf{m}\times\mathbf{B}$ (where $\mathbf{B}$, $\mathbf{m}$, $\mathbf{F}$, $\boldsymbol{\tau} \in \mathbb{R}^3$). Throughout this paper we assume homogeneity of applied fields such that $\nabla\mathbf{B} = 0$ and thus $\mathbf{F} = 0$. Consequentially, the only active component of the wrench is $\boldsymbol{\tau}$.

### 4.3.3 Balance of Momentum

The torque acting on the tentacle as a consequence of the interaction of the actuating magnetic field and the magnetization of the embedded PM is counteracted by gravity and by the elastic properties of the material. In the case of the unreinforced tentacle this material response is exclusively generated by the isotropic bulk elasticity of the silicone. However, for the reinforced tentacle we must also include the tensile and compressive stresses of the fibers. At all measured states the system was assumed quasi-static and as such the sum of all forces and the sum of all torques at all points must be zero.

A reduction in the ratio of bending to twisting stiffness is achieved by constraining the principle stretches of the twisting primitive using a material of far greater elastic modulus than the host elastomer ($E_{PLA} \approx 40E_{silicone}$). These higher stiffness fibers have extremely high aspect ratios such that they can be assumed to only support compressive and tensile stresses (not shear stresses); the mechanical definition of a truss element. This characteristic, when oriented correctly, can be exploited to minimize the impact of any strain limitation in the bending primitive.

It is possible to characterize elastic moduli as a function of direction, to accommodate a difference between tensile and compressive stiffness. This characteristic is explored in some depth in [24] and would add significant complication to any analysis of fiber reinforcing. In the presented case we only consider reinforcing materials that can be considered to have a scalar elastic modulus.

### 4.3.4 Finite Element Method

The simulation environment was built in COMSOL mutiphysics v5.5 (COMSOL AB, Stockholm, Sweden) using the solid mechanics module to simulate the silicone elastomer and PM's, and the truss module to simulate the fiber reinforcement.

NdFeB magnets have an elastic modulus of 150 GPa, ($\approx 10^6$ times the stiffness of Ecoflex 00-30) and can therefore be modeled as rigid domains of infinite stiffness. Magnetic torque is applied via mechanical moment on a rigid domain. This torque is a function of applied field and magnetization in each of the three directions but also of the three dimensional rotation of the rigid domain. This iterative calculation was hardcoded into the mechanical moment input, without loss of accuracy, circumventing the need to include direct consideration of electromagnetics with its attendant non-linearity and mesh requirements. Actuation was simulated as a 3.2 mm x 3.2 mm N52 NdFeB cylindrical PM embedded into the elastomer subject to a homogeneous magnetic flux density of -20 mT $\leqslant |\mathbf{B}| \leqslant$ 20 mT. The remanent magnetization of N52 NdFeB is given as $B_r = 1.455$ T (K&J Magnetics, Inc., USA).

The material employed for the reinforcing fiber is, in the numerical model, represented as a chain of truss elements. These elements are attached to the solid mechanics module using a prescribed displacement option effectively imposing zero slippage between the fibers and the elastomer; a valid assumption when interactive shear forces are sufficiently low.

All models were meshed using tetrahedral elements, free-formed by the COMSOL auto-mesh generator. The larger, two segment, simulation required 26,000 tetrahedral finite elements and took 60 seconds to converge utilizing Newton-Raphson iterations within the MUltifrontal Massively Parallel sparse direct Solver (MUMPS) option. For a parametric sweep of applied actuating field $|\mathbf{B}|$ from -20 to +20 mT in 1 mT increments this represents a 40 minute run-time on a 3.2 GHz, 32 GB, 16 core Intel Xeon Gold processor.

## 4.4 Single Segment Optimization

Here we isolate bending and twisting in our single segment numerical simulations with the objective of assessing the impact of variations in our design variables on these respective primitives. The optimized solution which we converge upon will then be implemented for a multi-segment tentacle in Section 4.5. The four design variables considered in this study are; fiber angle, $\theta_H$, number of helices, $N$, elastic modulus, $E$ and filament diameter, $d$. The objective of the optimization is to increase twisting stiffness with as little increase in bending stiffness as possible. The first two design variables are considered in Section 4.4.1 and the latter two, which are inextricably linked, in Section 4.4.2.

### 4.4.1 Variation in Fiber Angle and Number of Helices

For the purposes of this study fiber angle ($\theta_H$) is defined as the angle between the fibers and the longitudinal axis of the manipulator ([15]). Figure 4.4**A** shows the effect on bending and twisting of varying fiber angle for a double helix ($N = 2$) of filament diameter $d = 200$ $\mu$m and modulus of elasticity $E = 1$ GPa. An increase in fiber angle produces a higher ratio of bending to twisting only beginning to fall away above $\theta_H = 85°$.

A higher fiber angle increases the length of fiber per unit length of manipulator (as pitch is proportional to the tangent of the negative of fiber angle). An alternative method for increasing fiber length per unit length of the manipulator is through the use of additional concentric helices. To maintain symmetry, these helices must be increased in pairs (one left-handed helix and one right-handed helix). Figure 4.4**B** shows the effect of varying

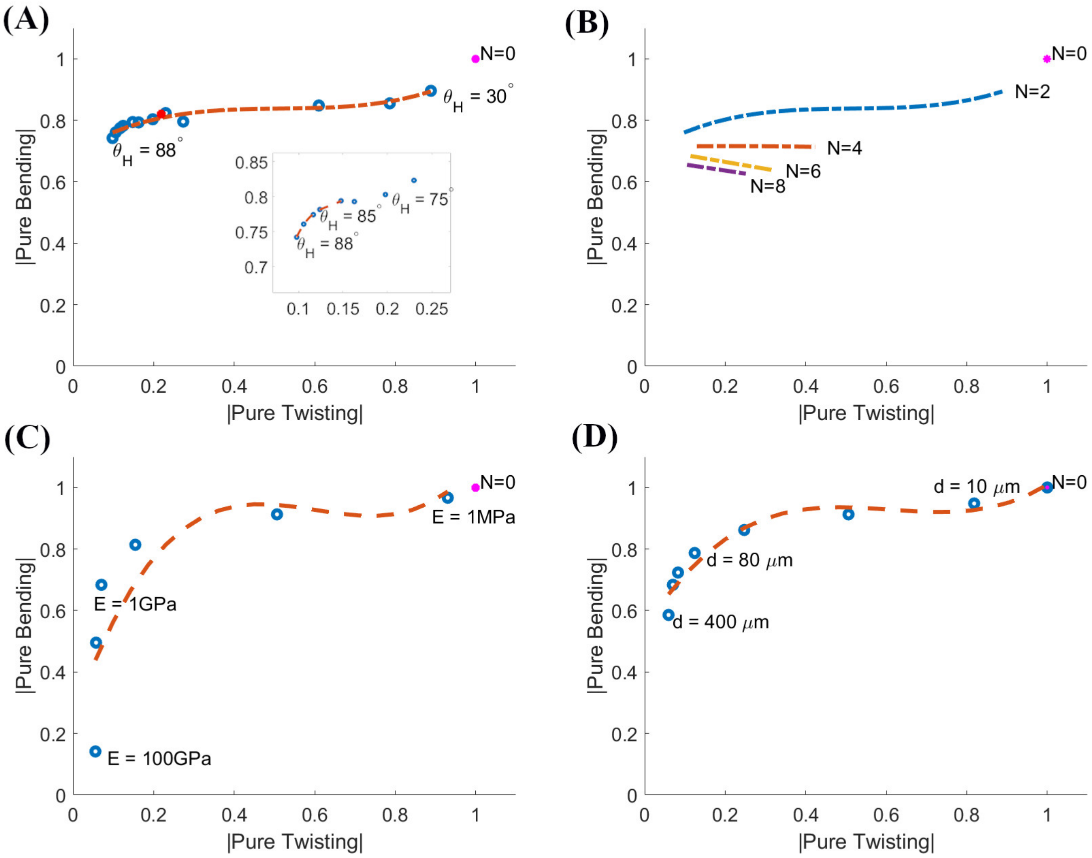

Figure 4.4: Pure bending versus pure twisting for various helix arrangements under 10 mT actuation. **(A)** Variation in fiber angle ($\theta_H$). **(B)** Variation in number of helices ($N$). **(C)** Variation in elastic modulus ($E$), **(D)** Variation in diameter of reinforcing fibers ($d$). The unreinforced sample appears as N = 0 at the point (1,1). All twisting (x-axis) and bending (y-axis) results are shown as a proportion of this unreinforced result. The objective therefore is to move as far to the left on the x-axis as possible whilst staying as high as possible on the y-axis. **(A)** Shows the double helix ($N = 2$) arrangement for $30° \leqslant \theta_H \leqslant 88°$ and the inset shows a zoom of the left hand extremity of the curve for higher $\theta_H$. The red spot represents the degenerate case $\theta_H = 90°$ which is included for completeness. This is not in fact a helix but reinforcing rings spaced at 1mm centers along the tentacle length. The curve gradient equals unity at $\theta_H = 85°$. **(B)** Shows the impact of increasing number of helices at various fiber angles. Results shown are: $N = 2$ taken from **(A)**, $N$ = 4, 6, 8, $\theta_H = 50° : 85°$. **(C)** Shows the effect of a logarithmic increase in elastic modulus for fixed filament diameter ($d = 200$ $\mu$m), fiber angle ($\theta_H = 85°$) and number of helices ($N = 2$). The curve gradient equals unity at $E = 1$ GPa. **(D)** Shows the effect of increasing filament diameter for fixed elastic modulus ($E = 1$ GPa), fiber angle ($\theta_H = 85°$) and number of helices ($N = 2$). The curve gradient equals unity at $d$ = 200 $\mu$m.

the number of helices for a variety of fiber angles (where filament diameter $d = 200$ $\mu$m and modulus of elasticity $E = 1$ GPa). It is clear from Figure 4.4**B** that $N = 2$ dominates alternative arrangements, this result also supports ease of manufacture.

### 4.4.2 Variation in Elastic Modulus and Filament Radius

The elastic and geometric characteristics of the fiber reinforcement, relative to the elastomer, are crucial to successful strain restriction. If the elastic modulus or fiber diameter are too high then bending flexibility will be lost and if too low then twisting will be unconstrained and instability will persist. There is, however, a fundamental inter-relationship between the two variables. The uni-axial stiffness of a truss member is a linear function of $EA$ (where $A$ is cross-sectional area) so any increase in $E$ can be counteracted by a corresponding decrease in $A$ and vice versa. The tipping point at which the ratio of bending to twisting stiffness starts to drop in both Figure 4.4**C** and 4.4**D** lies where the constant $EA$ is approximately equal to 30 N.

In theory, there are infinite ways to produce an $EA$ value of approximately 30 N, however, in practice limitations in material type and achievable dimensions exist. If a non-ferrous metal such as Titanium were used as reinforcing material ($E_{Titanium} = 100$ GPa), a filament diameter of $d = 20$ $\mu$m would be required. This does not represent an easy-to-manufacture scale. Conversely, were we to manufacture our reinforcing filament from a highly flexible polymer such as Ninjaflex ($E_{Ninjaflex} = 10$ MPa) we would need a filament diameter, $d = 2$ mm which would not physically fit into the catheter at our desired scale. The consequence of these practically imposed limits is that, to fulfill an optimal $EA$ of 30 N, we need a mid-range stiffness material fabricated at a physically realistic diameter.

## 4.5 Shape Forming Tentacle

Figure 4.5 demonstrates, for an unstably actuated (135° between **B** and **m**) single-segment CM, the potential of fiber reinforcing to reduce twisting while allowing bending for obtuse magnetization-magnetic field angles. The use of reinforcement, however, is most beneficial

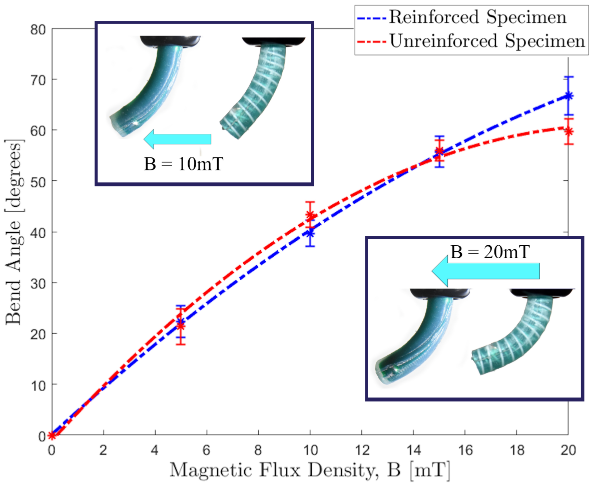

Figure 4.5: Actuating magnetic flux density ($|\mathbf{B}|$) against bend angle ($\theta$) for unreinforced and reinforced single segment specimens, magnetized in the unstable orientation (135° between **B** and **m**) as detailed in Figure 6.1. At lower actuating fields the absence of reinforcing fibers results in a softer CM and thus permits a higher level of deformation (as observed in the 10 mT insert). As applied field increases the reinforced specimen resists the unstable twisting primitive and thus generates greater magnetic torque about the desired axis, we therefore observe greater bending deformation (20 mT insert).

in multi-segment cases where magnet directions are non-parallel [9]. Accordingly, in this section we apply the concept to a two segment design. As shown in Figure 4.6, we have a CM of 40 mm total unconstrained length and 6 mm diameter with two 3.2 mm x 3.2 mm cylindrical N52 NdFeB PMs embedded at 18 mm and 38 mm centers from the mechanical constraint (z = 0). Both magnets are aligned such that their magnetization vectors lie in the x-z plane. The upper embedded magnet is aligned at a 90° angle to the applied field and the lower at a 135° angle.

### 4.5.1 Numerical Result

To demonstrate minimization of unstable twisting in the FE simulation we show Figures 4.7**A** and 4.7**C**. Optimal fiber reinforcement would represent PLA ($E_{PLA}$ = 2.4 GPa) at a filament diameter of $d$ = 130 $\mu$m. In practice, the thinnest filament we managed to extrude for this study was $d$ = 400 $\mu$m; suboptimal by a factor of 3 but sufficiently close to the optimal diameter to demonstrate our concept. The simulated result for the unreinforced tentacle (Figure 4.7**A** and supporting video) clearly illustrates the issue we are trying to eradicate. In a twist free solution we would expect to see twist: $\psi = 0°$ and all

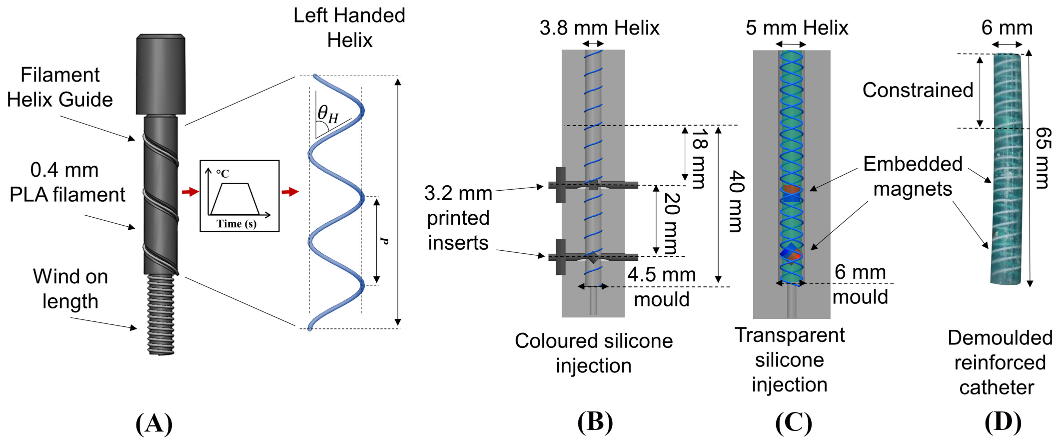

Figure 4.6: Fabrication process of the reinforced magnetic catheter. **(A)** Helix formation with a 0.4mm PLA fiber at a fiber angle of $\theta_H$. Helix pitch (P) is the parallel length of one complete turn such that $tan(90° - \theta_H) = P/\pi D$ ($D$ = helix diameter). **(B)** Molding of tentacle core with inner helix and printed inserts to create magnet cavities, EcoFlex00-30 was injected into the mold and cured. **(C)** Magnets placed in cavities and outer, opposing helix secured around the tentacle core. EcoFlex00-30 injected into the mould and cured to create a 1.5 mm outer coating. **(D)** The demolded two segment tentacle featuring double helix reinforcing.

rotation being concentrated into bend: $\theta$. This is what we see for the reinforced specimen with $\theta = 68°$. The unreinforced specimen however, taking the inverse solution from the rotation matrix, we see a large twist angle, $\psi = 161°$, and the attendant reduction in bending, $\theta = 10°$.

### 4.5.2 Fabrication

To verify the findings from the FE simulation, we fabricated a design of the same dimensions. Figure 4.6 outlines the full fabrication process. Helices were fabricated from white PLA (Material 1613, Ultimaker, Netherlands). Filament was extruded to a fiber of diameter 0.4 mm (±0.02 mm). Cylinders featuring the desired helical groove were 3D printed (RS-F2-GPGR-04, Formlabs, USA) to host the fibers, which were wound around the forms and secured before being subjected to a heat cycle peaking at 60°C for 30 minutes. This process embedded the helical shape into the filaments allowing them to retain the helix design upon removal from the form. This was repeated for both left and right-handed helices with a helix angle of $\theta_H = 85°$. As depicted in Figure 4.6**B**, the lower diameter, clockwise helix was secured in a 65 mm X 4.5 mm cylindrical mold. Cylindrical inserts were also secured inside the helix to create cavities at predefined desired angles for the PMs to be retrofitted. Silicone (Ecoflex00-30, Smooth-On Inc, USA) was mixed with green pigment (Silc Pig, Smooth-On Inc, USA) and degassed in a high vacuum mixer (ARV-310, THINKYMIXER, Japan) at 1400 rpm, 20.0 kPa for 90 seconds. The mixture was then injected into the mold and cured at room temperature for four hours. This cured structure was demolded and set within the outer, anti-clockwise helix, inserts were removed and PMs placed in the resulting cavities. The second moulding stage (Figure 4.6**C**) then provided 1.5 mm additional diameter of clear EcoFlex00-30 to secure the PMs and the outer helix. An example of the completed design is shown in Figure 4.6**D**.

### 4.5.3 Experimental Result

To evaluate the fabricated samples, an actuating field was supplied using a uni-directional Helmholtz coil (DXHC10-200, Dexing Magnet Tech. Co., Ltd, Xiamen, China) as shown in Figure 4.8. The response to actuation (taken at $|\mathbf{B}| = 20$ mT) of our two segment catheter is shown in Figure 4.7 (magnetization and actuating field vectors indicated in Figures 4.7**A** and 4.7**C**). Angle of twist at the tip of the CM is shown for the range of actuating fields 0 mT $\leqslant |\mathbf{B}| \leqslant$ 20 mT for simulated and experimental results in Figure 4.9.

Bend angle of the lower PM is derived from the derivative (yellow hatched line) of a fitted second order polynomial (red hatched curve: Polyfit, Matlab version R2018b, the MathWorks, Natick, MA, USA.). The angle of twist has been determined by fitting a first order polynomial to imprinted longitudinal lines down the trunk of the segment and measuring the angle $\phi$ between this and the angle of bending at the same z position. This helix angle determines the angle of twist $\psi$ via the relationship:

$$tan(\phi) = \frac{\psi.d}{2.L} \tag{4.2}$$

All experiments were repeated three times under identical conditions. Figures 4.7**A** and 4.7**B** are unreinforced and therefore more prone to the twisting instability. In the

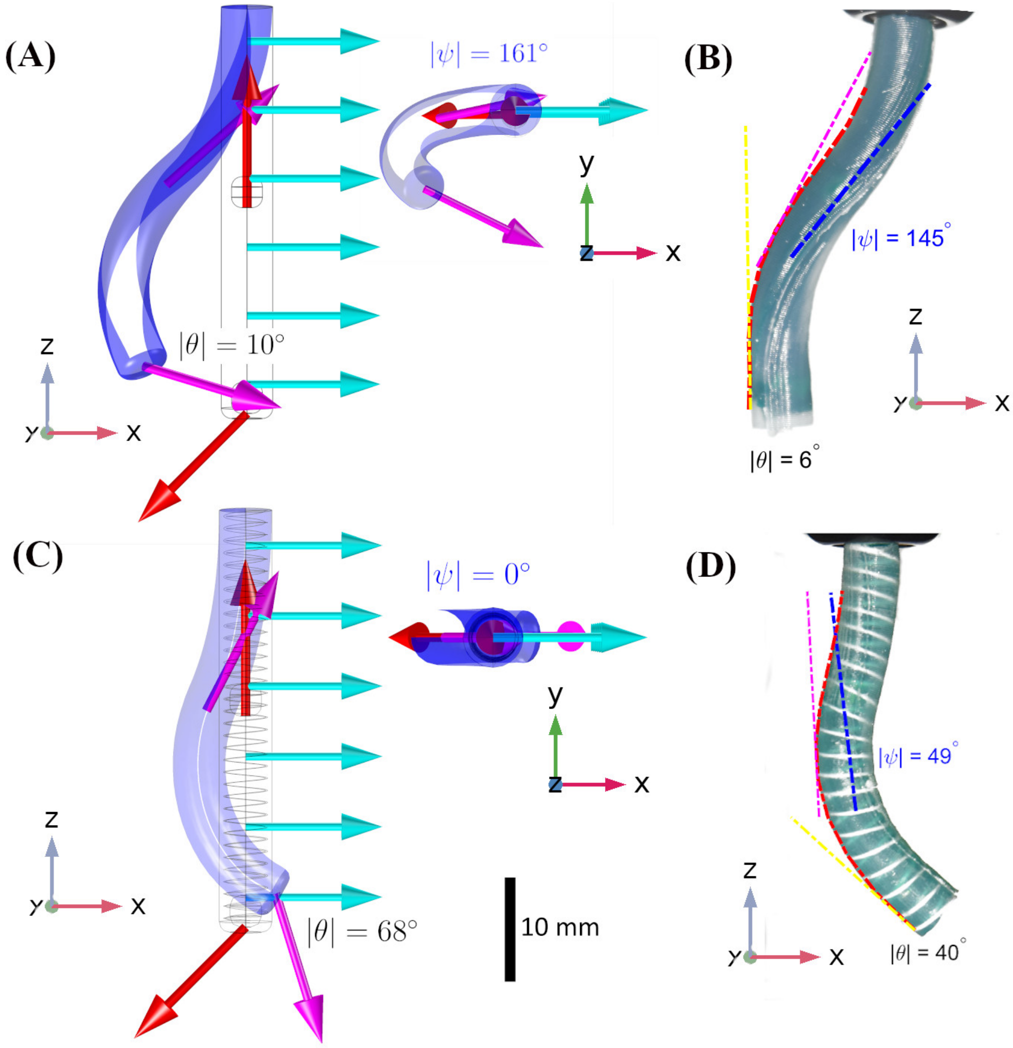

Figure 4.7: Both reinforced and unreinforced specimens have identical referential magnetizations (red arrows in the numerical simulation) and are subject to the same actuating field ($\mathbf{B} = [20 \quad 0 \quad 0]^T$ mT; turquoise arrows in the numerical simulation). In the unreinforced sample **(B)** mean twist is $\psi = 145° \pm 12°$ (where 180° would indicate a complete reversal of the PM about $z$) and mean bend is $\theta = 6° \pm 5°$. In the reinforced sample **(D)** mean twist is reduced to $\psi = 49° \pm 5°$ and, due to preservation of magnetic energy, mean bend increases to $\theta = 40° \pm 7°$. The instability which is observed in real world experiments **(B)** clearly appears in the unreinforced state in the FE Simulation **(A)**. This twist is shown more strikingly from the superior view in the upper inset of **(A)**. In the reinforced numerical model **(C)** twisting is completely eradicated by a double helix of PLA at a fiber angle of 85°. This is shown from the superior view in the lower inset. Videos of these deformations are available in the supplementary material.

unreinforced FE model (Figure 4.7**A**) we observe a distal twist angle of $\psi = 161°$ and bend angle of $\theta = 10°$ at $|\mathbf{B}| = 20$ mT (a plot of actuating field against twist angle is shown in Figure 4.9). The unreinforced experimental sample (Figure 4.7**B**) twists through $\psi = 145° \pm 12°$ (as compared to $\psi = 49° \pm 5°$ in the reinforced sample). This twisting

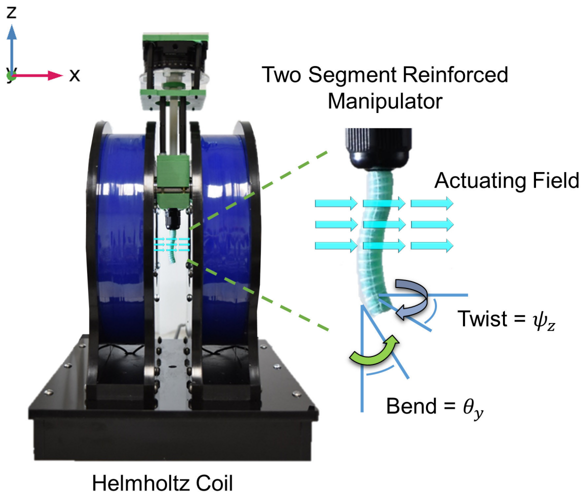

Figure 4.8: A sample tentacle under actuation in the Helmholtz coil and the two motion primitives being measured: Twist about the local $z$ axis ($\psi$) and Bend about the $y$ axis ($\theta$).

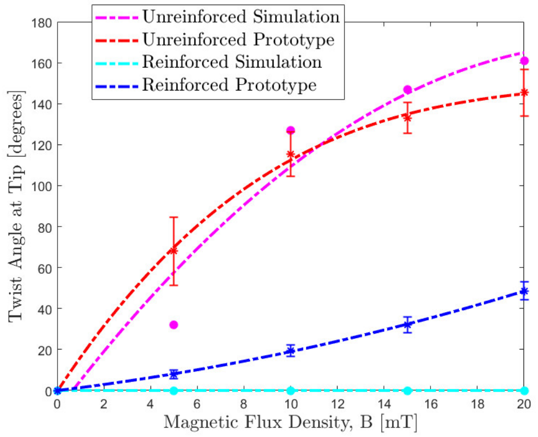

Figure 4.9: Actuating magnetic flux density ($|\mathbf{B}|$) against twist angle at tip ($\psi$) for the unreinforced and reinforced two segment *tentacles* shown in Figure 4.7. In the reinforced simulation (yellow), twist is completely eradicated for all applied fields. Whilst this success isn't fully recreated in the reinforced experimental protoype (blue) there is still a significant reduction in unwanted twist across the full spectrum of actuation.

results in a loss of magnetic energy in the desired primitive and a consequential reduction in bending at the lower PM, $\theta = 6° \pm 5°$. Figures 4.7**C** and 4.7**D** are reinforced with PLA filament ($E_{PLA}$ = 2.4 GPa) of diameter $d$ = 400 $\mu$m at a fiber angle of $\theta_H = 85°$ and display reduced twist and consequential increase in bend compared to the unreinforced sample. The lower PM shows a bend angle, for the reinforced specimen (Figure 4.7**D**), of $\theta = 40° \pm 7°$ as compared to a bend angle of $\theta = 68°$ in the corresponding FE model (Figure 4.7**C**). This discrepancy can be attributed to the continued (but greatly reduced) presence of twist in the experimental prototype as compared to the complete eradication of twist in the idealized FE Model.

## 4.6 Conclusion and Future Work

In this introductory work, we demonstrate the issue of instability of magnetic CMs under certain configurations of $\mathbf{B}$ and $\mathbf{m}$. We then applied fiber reinforcement, for the first time in magnetic soft robotics, as a means to mitigate this issue. Using our reinforcing at an optimized fiber angle of 85° we achieve a 78% mean reduction in the twisting primitive and a 67% reduction at $|\mathbf{B}| = 20$ mT for our fabricated 40 mm by 6 mm two-segment shape forming catheter. Using our novel design we have significantly reduced the consequences of chaotic input instabilities and created a more robust system which will allow for longer and more varied magnetic catheter profiles.

Limitations in fabrication capabilities have restricted our experimental twist reduction capacity. For practical, large deformation navigations such as gastrointestinal and endovascular interventions we need to exhibit closer reconciliation to numerical results. As such, we hope to develop an automated, miniaturized, and therefore more robust and versatile fabrication technique for variable reinforcement of magnetic catheters. Additionally a more exhaustive optimization procedure for the geometric characteristics of the reinforcement is desirable. In order for the simulation to more closely recreate reality we would also incorporate the unavoidable low magnitude, out of plane input errors in the actuating field which always occur in the real world and also simulate the interaction between multiple embedded permanent magnets. Both small but present contributions to simulation error.

These developments will allow us to move beyond this preliminary phase of study into more thorough and expansive experimental demonstrations. This should offer closer agreement to simulated outcomes and a greater reduction in unwanted twisting which will start to open up the possibility of practical, real-world navigation. From this initial platform, we can look forward to producing multiple-segment catheters capable of stable open-loop navigation through trajectories taken from pre-operative patient images. With this contribution we have taken a step towards fulfilling the potential of magnetic shape forming tentacles for navigation through specific anatomical constraints in a safe and stable manner.

## Bibliography

[1] J. Burgner-Kahrs, D. C. Rucker, and H. Choset, "Continuum robots for medical applications: A survey," *IEEE Transactions on Robotics*, vol. 31, no. 6, pp. 1261–1280, 2015.

[2] J. Edelmann, A. J. Petruska, and B. J. Nelson, "Magnetic control of continuum devices," *The International Journal of Robotics Research*, vol. 36, no. 1, pp. 68–85, 2017.

[3] Y. Kim, G. A. Parada, S. Liu, and X. Zhao, "Ferromagnetic soft continuum robots," *Science Robotics*, vol. 4, no. 33, p. eaax7329, 2019.

[4] T. da Veiga, J. H. Chandler, P. Lloyd, G. Pittiglio, N. J. Wilkinson, A. K. Hoshiar, R. A. Harris, and P. Valdastri, "Challenges of continuum robots in clinical context: a review," *Progress in Biomedical Engineering*, vol. 2, no. 3, p. 032003, aug 2020.

[5] N. Bira, P. Dhagat, and J. R. Davidson, "A review of magnetic elastomers and their role in soft robotics," *Frontiers in Robotics and AI*, vol. 7, p. 146, 2020. [Online]. Available: https://www.frontiersin.org/article/10.3389/frobt.2020.588391

[6] E. Diller, J. Zhuang, G. Zhan Lum, M. R. Edwards, and M. Sitti, "Continuously distributed magnetization profile for millimeter-scale elastomeric undulatory swimming," *Applied Physics Letters*, vol. 104, no. 17, p. 174101, 2014.

[7] G. Z. Lum, Z. Ye, X. Dong, H. Marvi, O. Erin, W. Hu, and M. Sitti, "Shape-programmable magnetic soft matter," *Proceedings of the National Academy of Sciences*, vol. 113, no. 41, pp. E6007–E6015, 2016.

[8] P. Lloyd, A. K. Hoshiar, T. da Veiga, A. Attanasio, N. Marahrens, J. H. Chandler,

and P. Valdastri, “A learnt approach for the design of magnetically actuated shape forming soft tentacle robots,” *IEEE Robotics and Automation Letters*, vol. 5, no. 3, pp. 3937–3944, 2020.

[9] P. Lloyd, G. Pittiglio, J. H. Chandler, and P. Valdastri, “Optimal design of soft continuum magnetic robots under follow-the-leader shape forming actuation,” in *2020 International Symposium on Medical Robotics (ISMR)*, 2020, pp. 111–117.

[10] G. Pittiglio, J. Chandler, M. Richter, V. Venkiteswaran, S. Misra, and P. Valdastri, “Dual-arm control for enhanced magnetic manipulation,” 2020, iEEE/RSJ International Conference on Intelligent Robots and Systems, IROS 2020 : Consumer Robotics and Our Future, IROS 2020 ; Conference date: 25-10-2020 Through 25-11-2020. [Online]. Available: https://www.iros2020.org/index.html

[11] L. Barducci, G. Pittiglio, J. C. Norton, K. L. Obstein, and P. Valdastri, “Adaptive dynamic control for magnetically actuated medical robots,” *IEEE robotics and automation letters*, vol. 4, no. 4, pp. 3633–3640, 2019.

[12] G. J. Vrooijink, M. Abayazid, and S. Misra, “Real-time three-dimensional flexible needle tracking using two-dimensional ultrasound,” in *2013 IEEE International Conference on Robotics and Automation.* IEEE, 2013, pp. 1688–1693.

[13] J. C. Norton, P. R. Slawinski, H. S. Lay, J. W. Martin, B. F. Cox, G. Cummins, M. P. Desmulliez, R. E. Clutton, K. L. Obstein, S. Cochran, and P. Valdastri, “Intelligent magnetic manipulation for gastrointestinal ultrasound,” *Science Robotics*, vol. 4, no. 31, pp. 1–14, 2019.

[14] A. A. Calderón, J. C. Ugalde, J. C. Zagal, and N. O. Pérez-Arancibia, “Design, fabrication and control of a multi-material-multi-actuator soft robot inspired by burrowing worms,” in *2016 IEEE International Conference on Robotics and Biomimetics (ROBIO)*, 2016, pp. 31–38.

[15] M. Krieg and K. Mohseni, “Relative planar strain control and minimizing deforma-

tion work in elastomeric sheets via reinforcing fiber arrays," *Composites Science and Technology*, vol. 142, pp. 50–64, 2017.

[16] F. Connolly, P. Polygerinos, C. J. Walsh, and K. Bertoldi, "Mechanical programming of soft actuators by varying fiber angle," *Soft Robotics*, vol. 2, no. 1, pp. 26–32, 2015.

[17] A. D. Marchese, R. K. Katzschmann, and D. Rus, "A recipe for soft fluidic elastomer robots," *Soft robotics*, vol. 2, no. 1, pp. 7–25, 2015.

[18] F. Connolly, C. J. Walsh, and K. Bertoldi, "Automatic design of fiber-reinforced soft actuators for trajectory matching," *Proceedings of the National Academy of Sciences*, vol. 114, no. 1, pp. 51–56, 2017.

[19] P. Polygerinos, Z. Wang, J. T. Overvelde, K. C. Galloway, R. J. Wood, K. Bertoldi, and C. J. Walsh, "Modeling of soft fiber-reinforced bending actuators," *IEEE Transactions on Robotics*, vol. 31, no. 3, pp. 778–789, 2015.

[20] J. Zhang, T. Wang, J. Wang, M. Y. Wang, B. Li, J. X. Zhang, and J. Hong, "Geometric confined pneumatic soft–rigid hybrid actuators," *Soft Robotics*, 2020.

[21] O. H. Yeoh, "Some Forms of the Strain Energy Function for Rubber," *Rubber Chemistry and Technology*, vol. 66, no. 5, pp. 754–771, 11 1993. [Online]. Available: https://doi.org/10.5254/1.3538343

[22] S. Nair, *Introduction to continuum mechanics.* Cambridge University Press, 2009.

[23] D. Steck, J. Qu, S. B. Kordmahale, D. Tscharnuter, A. Muliana, and J. Kameoka, "Mechanical responses of ecoflex silicone rubber: Compressible and incompressible behaviors," *Journal of Applied Polymer Science*, vol. 136, no. 5, p. 47025, 2019.

[24] L. Cappello, K. C. Galloway, S. Sanan, D. A. Wagner, R. Granberry, S. Engelhardt, F. L. Haufe, J. D. Peisner, and C. J. Walsh, "Exploiting textile mechanical anisotropy for fabric-based pneumatic actuators," *Soft robotics*, vol. 5, no. 5, pp. 662–674, 2018.

# Chapter 5

# The Braided Tentacle

**Chapter source:** P. Lloyd, O. Onaizah, G. Pittiglio, D. K. Vithanage, J. H. Chandler, and P. Valdastri, “Magnetic soft continuum robots with braided reinforcement,” IEEE Robotics and Automation Letters, vol. 7, no. 4, pp.9770–9777, 2022.

## Abstract

Flexible catheters are used in a wide variety of surgical interventions including neurological, pancreatic and cardiovascular. In many cases a lack of dexterity and miniaturization along with excessive stiffness results in large regions of the anatomy being deemed inaccessible. Soft continuum robots have the potential to mitigate these issues. Due to its enormous potential for miniaturization, magnetic actuation is of particular interest in this field. Currently, flexible magnetic catheters often rely on interactive forces to generate large deformations during navigation and for soft anatomical structures this could be considered potentially damaging. In this study we demonstrate the insertion of a high aspect ratio, 50 mm long by 2 mm diameter, soft magnetic catheter capable of navigating up to a 180° bend without the aid of interactive forces. This magnetic catheter is reinforced with a lengthwise braided structure and its magnetization allows it to shape form along tortuous paths. We demonstrate our innovation in a planar silicone pancreas phantom. We also compare our approach with a mechanically equivalent tip driven magnetic catheter and with an identically magnetized, unreinforced catheter.

## 5.1 Introduction

Soft continuum robots are an important avenue in overcoming the limitations of traditional steerable microcatheters for endoluminal interventions [1] [2]. Magnetically actuated continuum robots (MCRs) offer huge miniaturization potential and the prospect of safe navigation through small, sensitive and tortuous pathways [3] [4] [5]. Tip driven MCRs are established in the literature [6] [7] but are unable to actively shape form i.e. control their body shape independent of tip pose. This limitation is of particular concern when the navigation passes through unusually soft and sensitive tissue such as the pan-

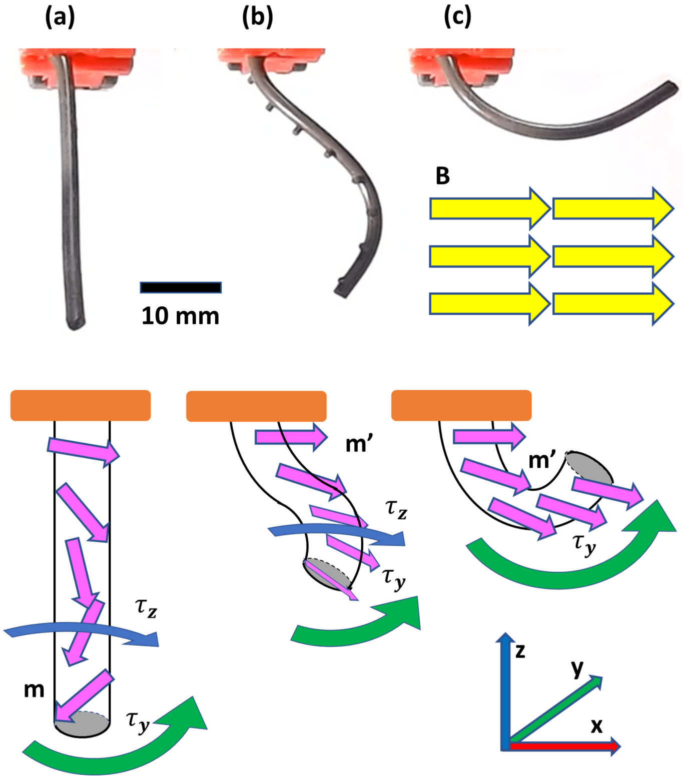

Figure 5.1: (a) The referential (undeformed) MCR showing resultant torques about the Y axis (green) and the Z axis (blue) as a consequence of the interaction between applied field (B, yellow arrows) and magnetization profile (m, purple arrows) (b) Compound bending and twisting of an unreinforced CR. The welts placed along the back of the MCR clearly illustrate the twisting in the experimental domain. (c) Pure bending of a braid reinforced (torsionally constrained) MCR under identical magnetization profiles and applied actuating field ($B_x = 20$ mT).

creas [8] [9] or the brain [10] [11]. Shape forming capability could potentially avoid painful and/or damaging interactive forces along the length of the MCR. Recently, MCRs which can shape form due to a variable magnetization profile along their length have been explored [12] [13] [14] [15], and our previous research demonstrated their efficacy for follow the leader navigations [16]. These MCRs have bespoke non-axial magnetization signatures which interact with applied magnetic fields to create torques capable of producing forward motion optimized for minimal contact [17]. This arrangement permits the use of far softer materials as reduced interaction allows for lower insertion forces - the stiffness of a traditional catheter is driven by the requirement to resist buckling under these insertion forces.

However, a fundamental limitation of this non-axial magnetization design arises when a shape-forming MCR attempts to navigate a path featuring large (90° degrees or more) deformation. As described in detail in [18], in order to generate large deformations, the applied magnetic field must oppose the MCR's magnetization generating an inverted pendulum instability. If unconstrained, in accordance with Timoshenko beam theory, the much lower energy pose available via twisting around the catheter's long 'easy' axis will result (Figure 6.1b and supporting video). This unstable phenomenon is increasingly problematic as the aspect ratio of length to diameter increases.

Closed loop control such as [19] could theoretically counteract this instability however this would require accurate, high frequency feedback from inside the body of both bending and twisting deformations, which currently represents a major challenge. Mechanical reinforcement is an alternative and more practical approach and was introduced to a large diameter (6 mm) MCR design in the form of double helix fibers [18]. This approach demonstrated significant improvement but proved difficult to miniaturize due to its complex fabrication process.

In this paper, we demonstrate the successful harnessing of magnetic instability into large deformation shape forming by reinforcing a high aspect ratio, 50 mm long x 2 mm diameter catheter using a braided structure along its length. The braid we employ is a commercially available, 1 mm external diameter nylon cord. In Section 6.2.5, we use it to experimentally demonstrate an increase in twisting stiffness that is 20 times the increase in bending stiffness. We demonstrate the practical advantage of this approach through autonomous follow-the-leader navigation into the pancreatic and bile ducts of a planar soft gelatinous phantom. This represents a continuation of our earlier work ([18]), but the proposed MCR design is 3 times smaller and exhibits a far higher ratio of twisting to bending stiffness. These improvements result in the first demonstration of such large deformations being generated during the insertion process without the requirement of forces of anatomical interaction. In particular, this absence of these forces represents a significant step forward in the development of atraumatic follow-the-leader MCRs. Furthermore, we demonstrate the inability of either a tip driven MCR or a similarly lengthwise magnetized but unreinforced MCR to achieve similar navigations when interactive forces are not available.

## 5.2 The Braided Catheter

In this section, we detail the model, fabrication method and characterization of our prototype braided MCR, actuated in a 1-D homogeneous field. The design principle is to utilize the anisotropic material response of an embedded braid to reduce instability under opposing field-magnetization conditions. Using mechanical constraint, axial stiffness is increased relative to bending stiffness. As such we develop a rigid-link model to consider these independent stiffness parameters as a function of the catheter's length. Through characterization of fabricated samples in a 1-D field, we determine these relative stiffness parameters to allow for optimization of mechanically reinforced designs in more realistic scenarios.

### 5.2.1 Rigid Link Robot Model

In order to capture anisotropic behavior, we represent our MCR as a serial chain of five rigid links each 10 mm long and connected by a three Degree-of-Freedom (DoF) sprung rotational joint. The three DoFs in each homogeneous rotational joint represent bending about the local X axis, bending about the local Y axis and twisting about the local Z axis, respectively. This characterization is repeated identically for each of the five rigid links such that any desired 50 mm path can be kinematically represented as a 5 x 3 array of joint angles $Q$. This allows the design to consider quasi-static insertion over discrete time steps.

A magnetic dipole with moment $\mathbf{m}$ in a homogeneous field $\mathbf{B}$ will experience a resultant magnetic torque linearly proportional to applied field strength

$$\boldsymbol{\tau} = \mathbf{m} \times \mathbf{B} \tag{5.1}$$

where $\mathbf{B}$, $\mathbf{m}$, $\boldsymbol{\tau} \in \mathbb{R}^3$. The body torque acting on any given finite volume of the MCR as a consequence of the interaction of the actuating magnetic field and the magnetization of that region of doped elastomer will produce deformation and therefore be counteracted by the elastic properties of the material. The deformation resulting from balancing magnetic and elastic torques is represented as the joint angle array ($Q$) which explicitly defines both the tip pose and the body shape of the MCR.

Under a three dimensional rigid link assumption, as detailed in [17] and according to [20] [21], we balance the magnetic and mechanical torques across all 15 joints in the MCR at any given time step

$$J^T\boldsymbol{\tau} - KQ = \lambda \tag{5.2}$$

with $J^T$ the Jacobian transpose of the MCR, $\boldsymbol{\tau}$ the magnetic torque from Equation 6.1 (both calculated at the desired joint angles, $Q$), $K$ the stiffness matrix and $\lambda$ the residual error in the torque balance: zero for a stable arrangement.

For the sake of simplicity, and due to the principle demonstration being performed in a low friction horizontal plane, gravity has been set to zero in this calculation. Gravity was incorporated in the corresponding theoretical framework in [17] and was found to impart less than 20% of the magnitude of the magnetic torque (in a vertically aligned demonstration).

To construct the stiffness matrix for each identical 3 DoF joint, we assume linear elasticity such that

$$K = \mathrm{diag}(E_x I_x \ E_y I_y \ E_z I_z) \tag{5.3}$$

where $E_x$, $E_y$ and $E_z$ are the Young modulus in the three directions (equal to E for an isotropic continuous medium, Section 6.2.5 gives details on anisotropic characterization), $I_x$ and $I_y$ second moment of area for bending and $I_z$ second moment of area for twisting

[20].

By summing the errors ($\lambda$) across all rigid links and all insertion time steps a single function to be minimized is defined with the 5x3 arrays $\mathbf{m}$ and $\mathbf{B}$ as objective variables. This was solved as in [17] using the Genetic Algorithm (GA, Global Optimization Toolbox, Matlab version R2021b, the MathWorks, Natick, MA, USA) to generate suites of magnetizations and actuating fields specifically for each set of joint angles and stiffness matrices.

### 5.2.2 Fabrication

In order to test our MCRs we developed a fabrication process, outlined in Figure 6.2. Nylon braid of external diameter 1 mm (Everlasto - James Lever 1856 Ltd, Manchester, UK) was held in axial alignment within a 2 mm internal diameter perspex tube using 3D printed end-caps ((RS-F2-GPGR-04, Formlabs, USA). The tube was pre-drilled with 0.5 mm diameter holes at 5 mm center spacings to give a clear indication of which side is the ‘front’ of each catheter - this welted effect can be clearly seen in Figure 6.1b. The elastomer (Ecoflex-0030, Smooth-On Inc, USA) was mixed with neodymium-iron-boron (NdFeB) microparticles with an average diameter of 5 µm (MQFP-B+, Magnequench GmbH, Germany) in a 1:1 mass ratio. This composite was mixed and degassed in a high vacuum mixer (ARV-310, THINKYMIXER, Japan) at 1400 rpm, 20.0 kPa for 90 seconds. The mixture was injected into the tubing and cured at room temperature for four hours before removal giving specimens such as that shown in Figure 6.2c.

Upon removal from the mold, the specimens were secured into a bespoke 3D printed magnetizing tray (Figure 6.2d) before being subjected to a saturating uniform field of 4.644 T (ASC IM-10-30, ASC Scientific, USA). The specific geometry of the magnetizing tray is determined according to the algorithm described in Section 5.2.1 and in [17].

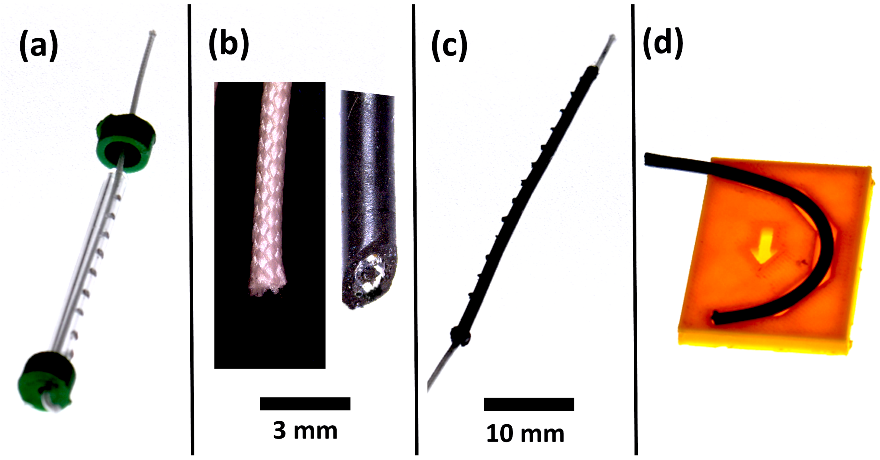

Figure 5.2: (a) The 1 mm diameter nylon braid is secured in a 2 mm internal diameter perspex tube. This is injected with NdFeB doped Ecoflex-0030 and time cured. (b) Magnified images of the 1 mm diameter braid (white on a black background) and a diagonal cut of the 2 mm diameter MCR after casting (black on a white background with the embedded braid seen as a white circle). (c) The reinforced MCR is delaminated and trimmed to size. (c) This can then be magnetized in any direction desired. In the example shown it is being prepared for the demonstration in Section 5.2.4.

### 5.2.3 Elastomeric Characterization

In order to optimize the rigid link model and determine the required magnetizations and actuating fields we must populate the stiffness matrix, K (Equation 6.3). As stated in Section 5.2.1, in the case of the unreinforced MCR, this material response is exclusively generated by the isotropic bulk elasticity of the doped silicone. However, for a braid-reinforced MCR we must allow for deliberately inbuilt anisotropy in the response to actuation. The braid is constructed of multiple interwoven helical threads, which interact to constrain shear deformations at the local level whilst permitting normal deformations. Being positioned at (or near) the radial extremities of the MCR, these local constraints translate into globally constrained twisting whilst globally permitting bending [18] [22]. Pure bending and pure twisting characterization experiments were therefore performed, as illustrated in Figure 5.3.

Samples were prepared in accordance with the method introduced in Section 6.2.4 with radial magnetization for the twisting samples and axial magnetization for the bending samples [18]. Three identical versions of each sample were hung vertically and exposed to an orthogonal 1-D field ramped from -25 mT to 25 mT for three repetitions each.

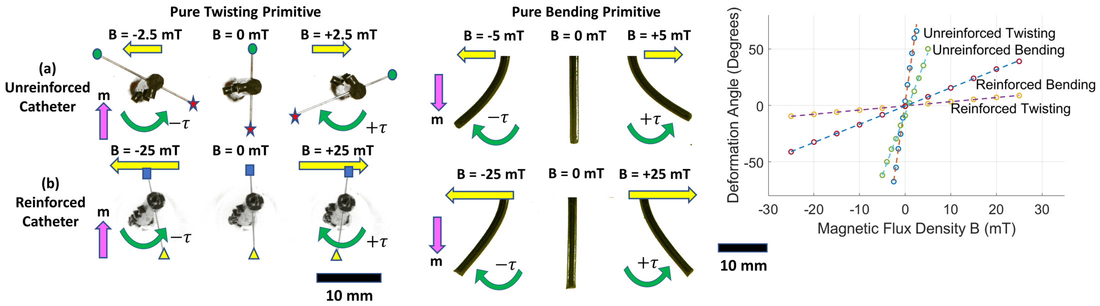

Figure 5.3: Testing of primitive deformations for elastomeric characterization. Under pure twisting (left), radially magnetized 20 mm specimens are hung vertically and exposed to an orthogonal homogeneous field. The view shown is from below of (a) unreinforced catheter and (b) reinforced catheter (the tip has been pierced with a 0.25 mm diameter nitinol wire to aid visualisation and postprocessing). Under pure bending (centre), similar but axially magnetized specimens are hung vertically and the view shown is from the side. The graph (right) shows the curves of actuating field against angle of deformation. The reinforcing increases bending stiffness by around 5 times and twisting stiffness by around 100 times. The difference in curve gradient between twisting and bending for the isotropic, unreinforced specimen is due to the difference in second moment of area for the two deformations.

Table 5.1: Linearized pseudo elastic moduli for unreinforced and reinforced specimens of doped Ecoflex-0030. Note the torsionally constraining effect of the braid (20:1, twisting:bending stiffness) and the five-fold increase in MCR bending stiffness due to addition of the braid.

| | $E_x$ | $E_y$ | $E_z$ | $E_z/E_x$ |
|---|---|---|---|---|
| Unreinforced Sample (kPa) | 100 | 100 | 100 | 1 |
| Reinforced Sample (kPa) | 500 | 500 | 10,000 | 20 |

Primitive deformations were analyzed using the MATLAB imtool functionality giving the graph shown in Figure 5.3 relating applied field (**B**) to tip deformation angle (q) for a 20 mm specimen length (L). From the relationship

$$K\frac{q}{L} = |\mathbf{m} \times \mathbf{B}| \tag{5.4}$$

we established the stiffness parameters in Table 5.1. Despite the obvious increase in bending stiffness our MCR is still flexible compared with other soft magnetic catheters in the literature, for example, the PDMS (Polydimethylsiloxane) + NdFeB (20 % volume fraction) as prepared and employed in [7] has an effective elastic modulus of E = 1,400 kPa.

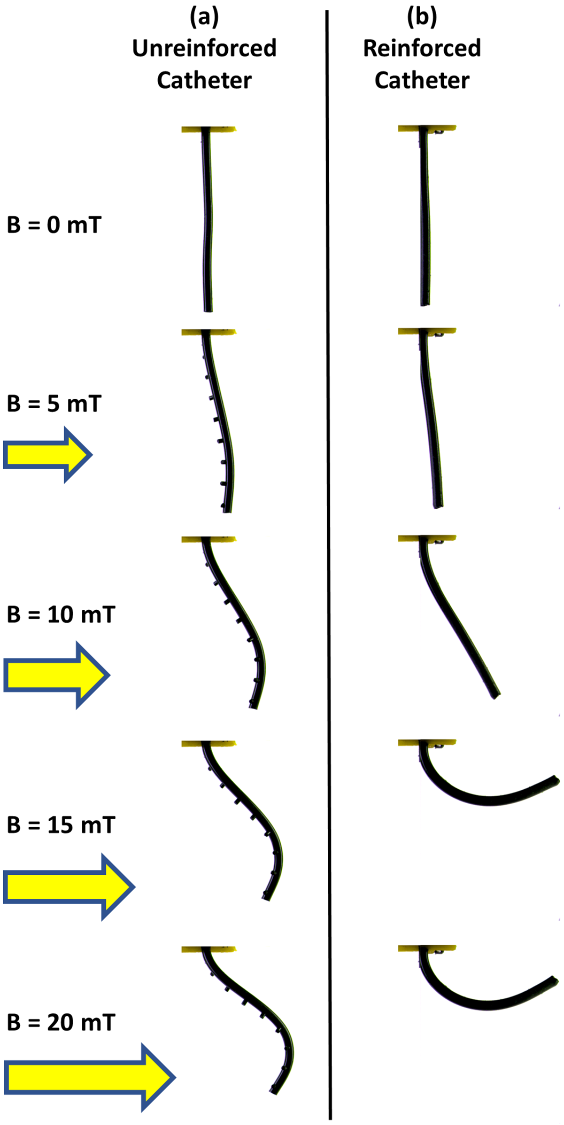

Figure 5.4: Elastomeric deformation under 1-D homogeneous actuation. Magnetization is as depicted in Figure 6.1 (purple arrows) and Actuating Field $B_x$ (yellow arrows) is ramped from 0 to 20 mT. (a) The twisted response of the unreinforced MCR. (b) The stable, constrained, and large deformation response of the braided MCR. These results are further demonstrated in the supporting video

### 5.2.4 Shape Forming in Free Space

To illustrate the impact of the inclusion of the braid on torsional stability and resulting deformation angle, two otherwise identical 40 mm samples (unreinforced and braid-reinforced) were fabricated and magnetized with the planar sinusoidal magnetization shown in Figure 6.1 (purple arrows). This magnetization was derived using the optimization algorithm described in Section 5.2.1, but constrained to only the final time-step of insertion and a 1-D field $B_x = +20$ mT. The joint angle array was simply specified as the largest possible angle of bending about the Y axis, zero about the X and Z axes. The sinusoidal magnetization which emerged from this process reconciles with intuition.

When exposed to a 1-D field $B_x = +20$ mT (yellow arrows) both prototypes *should* produce large in plane deformation. Figure 5.4 shows the expanded time stepping view of the result shown in Figure 6.1 and in the supporting video. The braid is clearly needed in order to stabilize the actuation and effectively convert this magnetic torque into large (greater than 100°) elastic deformation. As can be clearly seen the impact of anisotropic reinforcement is so profound as to be difficult to quantify - a maximal difference in tip orientation of $\approx 150°$.

This result allows the incorporation of previously unstable opposing field-magnetization combinations within the optimization solution. This in turn permits the possibility of higher bending angles and therefore successful low contact navigation through more tortuous pathways than previously possible.

## 5.3 Demonstration of Clinical Application

The ability to achieve large deformation shape forming may be useful in a large variety of clinical applications. One such application is catheterization of the notoriously soft and delicate pancreas [23]. To illustrate the potential for clinical relevance of our innovation, we performed navigations into the bile and pancreatic ducts of a planar, ultrasoft pancreas phantom. We compare these navigations with mechanically similar attempts using a tip driven MCR and an unreinforced length-wise magnetized MCR.

Current surgical catheters for pancreatic intervention have a minimum elastic modulus in the region of 2 GPa [24] in order to transfer longitudinal driving forces around the necessary internal corners at an appropriate scale and without buckling. This is 500,000 times stiffer than pancreatic tissue [9] and more than 4000 times stiffer than the catheter we have developed.

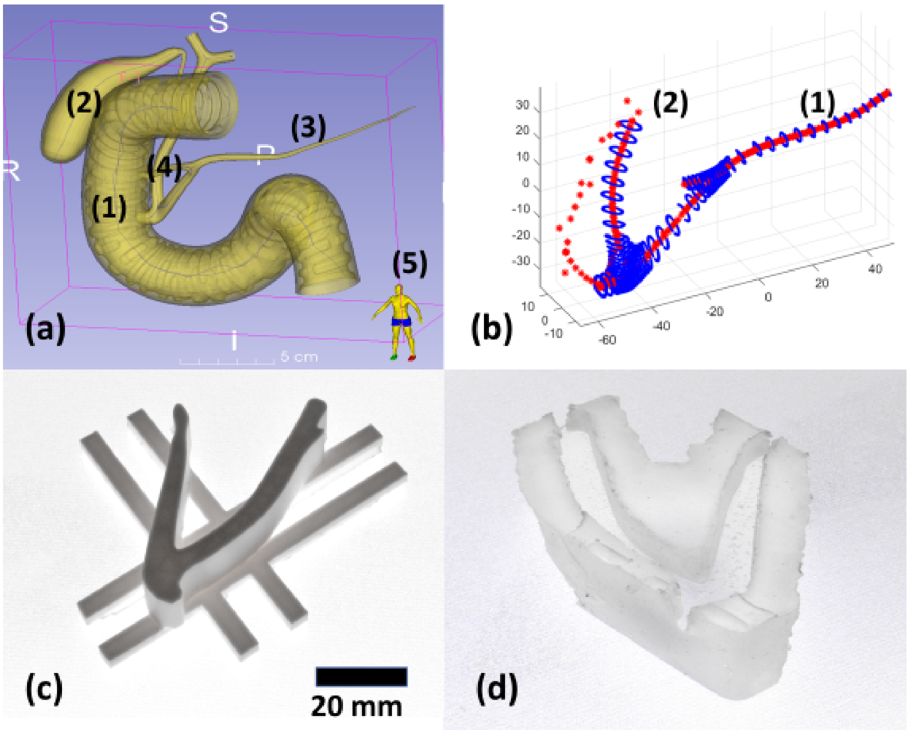

Figure 5.5: (a) The initial 3-D geometry of (1) duodenum, (2) gall bladder, (3) pancreatic and (4) bile ducts. The character at (5) shows the relative orientation of this anatomy. (b) The point-cloud (blue) of the area of interest: (1) pancreatic and (2) bile ducts. Center lines for path planning are shown in red. (c) The 3-D printed PLA imprint prior to casting - this is shown upside down for the sake of visibility. (d) The 5 kPa soft silicone phantom running from the major papilla into the ducts.

### 5.3.1 Path Planning

Utilizing anatomical data from the turbosquid dataset (www.turbosquid.com) (Figure 5.5a) we extracted center lines of the pancreatic and bile ducts (Figure 5.5b) using 3DSlicer (www.slicer.org). These center lines give desired pathways from a start point in the duodenum to a location 50 mm distal in either duct. These point cloud trajectories can be characterized as 5 x 3 arrays of joint angles ($Q$) in accordance with the rigid link assumptions described in Section 5.2.1. The redundancy in the mapping between trajectory and joint angles arising due to the lack of orientation about the local Z axis in the trajectory data is managed by minimizing deformed strain energy. This calculation is a function of the stiffness matrix (Equation 6.3) and, due to the deliberately isotropic design (Section 6.2.5), results in near zero twist. Consequently, a unique, minimum strain energy joint angle array can be used to supply the optimization described in Section 5.2.1. During navigation these links were sequentially inserted over five discrete time steps under the quasi-static assumption.

### 5.3.2 Soft Phantom

The soft phantom used for demonstration of our method utilizes anatomical data from the aforementioned turbosquid dataset. This provides accurate external geometry of the bile duct, pancreatic duct and common duct. The internal geometry of the duct network (Figure 5.5b) was scaled according to [25] which gives a bile duct maximal internal diameter of 7 mm. This scaling compensates for any inaccuracies in wall thicknesses of the original imaging. Furthermore, we have included a major papilla at the outlet of the drainage duct with a minimum diameter of 2.6 mm [26]. These combined dimensions were projected onto a sketch plane, extruded 20 mm, 3D printed (RS-F2-GPGR-04, Formlabs, USA) (Figure 5.5c) and then open-cast in silicone: 2 parts SoftGel A-341C to 3 parts DC200 silicone oil (50 cst) (www.dow.com/en-us) for 4 hours in accordance with [27] (Figure 5.5d). This gives an approximate linearized elastic modulus of E $\approx$ 5 kPa for strains of less than 10% which reconciles with the E $\approx$ 3 kPa for healthy pancreatic tissue given in [9]. During navigation the channel was lubricated with dyed water to reduce friction and aid visualization. We consider this approach an effective demonstrative environment and the open channel approach also allows for maximum visibility.

### 5.3.3 Actuation

A 3-D Helmholtz coil (3DXHC12.5-300, Dexing Magnet Tech. Co., Ltd, Xiamen, China) was used with a 60 mm cubed homogeneous workspace which can generate 3 linearly independent uniform magnetic fields up to 30 mT (Figure 5.6). These electromagnetic coils are connected to three independent power supplies (DXKDP, Dexing Magnet Tech. Co., Ltd, Xiamen, China) for each of the spatial axes. Power supplies connect to a PC from an RS232 serial communication port allowing control via MATLAB serial commands. A code is thus implemented to autonomously operate power supply output generating the desired 3D homogeneous magnetic fields.

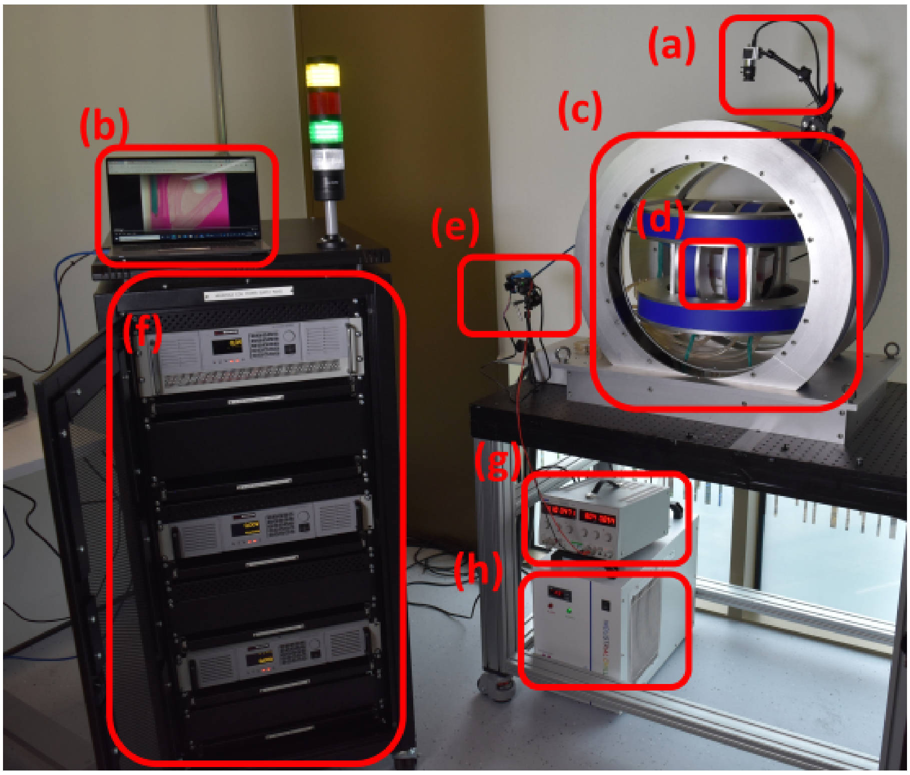

Figure 5.6: The 3D Helmholtz coil based actuation platform as described in Section 5.3.3. (a) Basler camera, (b) cpu (c) 3D Helmholtz coil, (d) 3D work space - site of experimental arrangement, (e) stepper motor, (f) 3 power supplies for Helmholtz coils, (g) power supply for stepper motor, (h) coolant tank for Helmholtz coils.

The insertion motor consists of a Nema 17 stepper motor (Micromech, UK), a 3D printer extrusion head minus the nozzle and is controlled using a UStepper S (http: //ustepper.com) stepper motor driver. This drives a 1.75 mm diameter PLA filament through a 2.5 mm internal diameter bowden cable sleeve to the insertion origin (as in Figure 5.7). The proximal end of the MCR is attached to the distal end of the filament using 2.5 mm diameter thermal shrink fitting sleeve. The stepper driver receives directional commands via a fourth serial port again operated from the same MATLAB code. Step count is proportional to the advance length of the inserter which was reconciled offline. Therefore, by controlling the step count and operating frequency, the inserter can extend and retract the MCR autonomously with known length and speed. In this case the inserter was programmed to extend the MCR with 1 mm increments synchronized to changes in actuating magnetic field. The entire system is capable of operating at a frequency of 2 Hz meaning a 50 mm navigation takes 25 seconds.

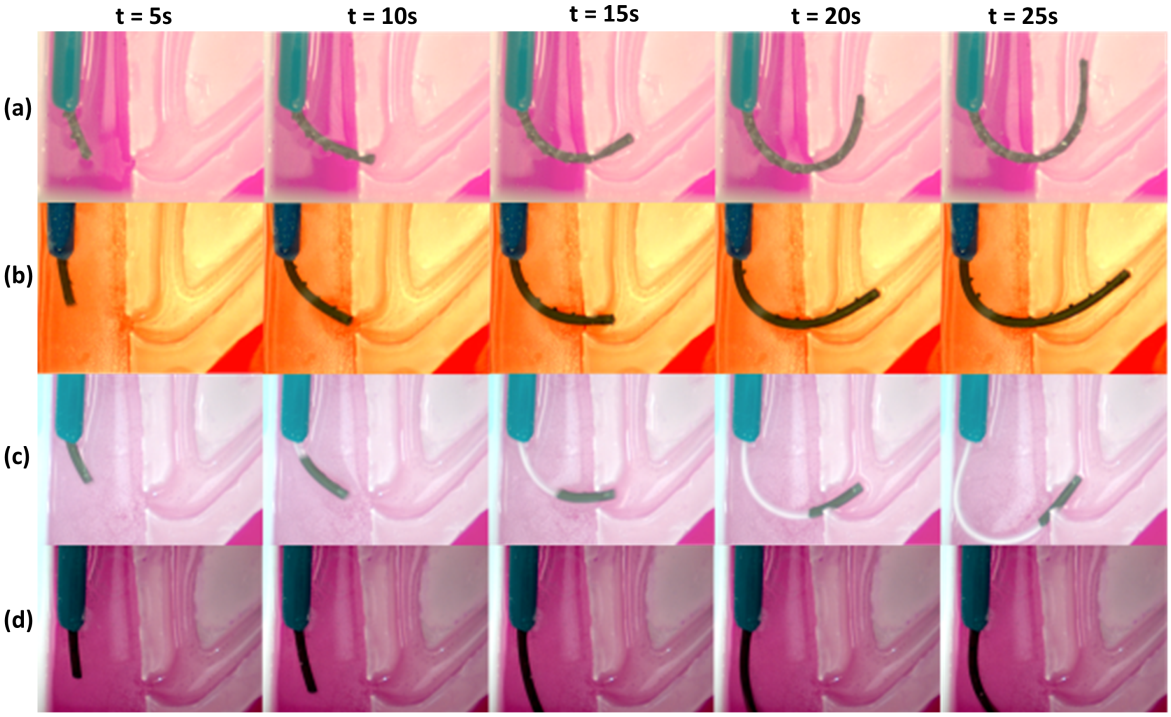

Figure 5.7: Navigation into the bile and pancreatic ducts - stills taken from the supporting video. Magnetizations and actuating fields are shown in the supporting video. (a) An optimized, reinforced MCR navigating into the bile duct. (b) An independently magnetized, reinforced MCR navigating into the pancreatic duct. (c) A tip driven MCR attempting to navigate into the pancreatic duct (d) An optimized, unreinforced MCR attempting to navigate into the pancreatic duct.

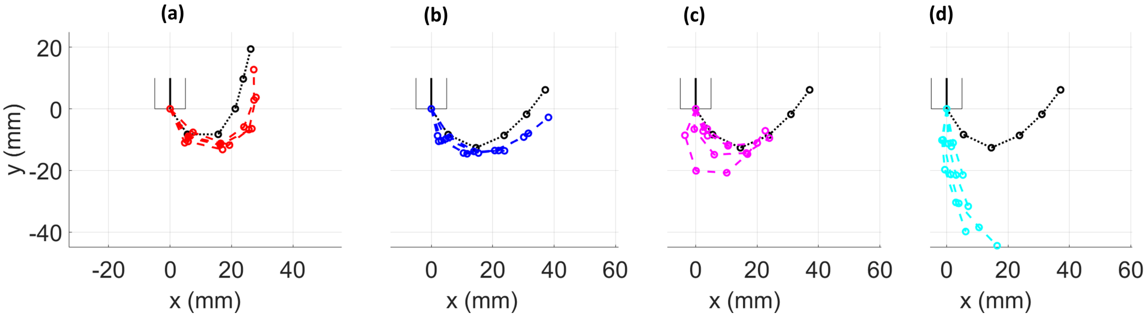

Figure 5.8: Desired path (black hatchings) against experimental data for (a) optimized navigation into the bile duct (red hatchings), (b) optimized navigation into the pancreatic duct (blue hatchings), (c) tip driven navigation into the bile duct (purple hatchings), (d) optimized but *unreinforced* navigation into the bile duct (turquoise hatchings). Position after each of five time increments for one experimental repetition are shown. Mean absolute spatial error calculated across all time steps and across all three experimental repetitions are (a) 4.7 mm, (b) 4.2 mm, (c) 9.1 mm and (d) 21.3 mm.

Experiments in the 3D coil were recorded using a top-view Basler Ace camera (acA2040-120uc Basler AG, Ahrensburg, Germany) with a Basler C23-3518-5M-P f35mm lens. Images and videos in the 1D trial were recorded similarly using a side-view camera.

## 5.4 Results

Figure 5.7 shows the five time steps of insertion into the pancreatic and bile ducts. These are all also shown in the supporting video. Figure 5.7a shows an optimized, reinforced MCR navigating 50 mm into the pancreatic duct. Figure 5.7b shows an independently optimized and therefore differently magnetized, reinforced MCR navigating 50 mm into the bile duct. Figure 5.7c shows a mechanically equivalent tip driven MCR attempting to navigate into the pancreatic duct. Actuating fields for this navigation were derived in exactly the manner described in Section 5.2.1 but with magnetization constrained to the tip driven arrangement. Figure 5.7d shows an unreinforced MCR, independently optimized to account for variation in material properties, attempting to navigate into the pancreatic duct. All insertions ran at 2 mm/s which represents an operating frequency of 2 Hz. All experiments were repeated three times under identical conditions.

Figure 5.8 shows the graphical representation of the same results. Desired path (black hatchings) against experimental data for Figure 5.8a optimized navigation into the bile duct (red hatchings), Figure 5.8b optimized navigation into the pancreatic duct (blue hatchings), Figure 5.8c tip driven navigation into the bile duct (purple hatchings), Figure 5.8d optimized but *unreinforced* navigation into the bile duct (turquoise hatchings). Mean absolute spatial error calculated across all time steps and across all three experimental repetitions are (a) 4.7 mm, (b) 4.2 mm, (c) 9.1 mm and (d) 21.3 mm.

## 5.5 Discussions and Future Work

For any scenario where the anatomy through which we are attempting to navigate is narrow and significantly softer than the catheter, and where deformation angles of greater than 90° are required, conventional mechanical and tip driven systems will be either ineffective or traumatic (or both). Here we show that a 2 mm diameter, length-wise optimally magnetized MCR, with braided reinforcement, can reach otherwise inaccessible locations.

There is still spatial error in the two successful navigations which can be attributed to the imprecise positioning of the origin of the MCR - the insertion point. This error affects the joint angle array and thus the required actuating fields. In order to minimize this error we intend to incorporate a shape based closed loop control algorithm in our future work which can recalculate required joint angles based on strain sensor feedback such as Fiber Bragg gratings.

We are aware that the NdFeB used in our demonstration is potentially cytotoxic. This is a problem which can be readily solved by coating the magnetic continuum robot with biocompatible materials such as silica, parylene [28] or hydrogel [7] and has been widely demonstrated in the literature.

The manner of failure of the tip driven MCR is interesting. By pushing from the base of a manipulator, forward motion in the opposite direction can only *ever* be achieved if (1) interactive forces are present and (2) the manipulator is sufficiently rigid to transmit these forces to the tip. In our demonstration, the ultrasoft phantom will not permit interactive forces of any significance, as pancreatic or brain tissue would not, and the MCR is too soft to transfer them even if it would.

The unreinforced MCR is also unsuccessful in its navigation. Whilst it is imperceptible to the naked eye (due to the speed at which this failure occurs), this is entirely attributable to the twist detailed in Section 5.2.4, in Figure 6.1 and in the supporting video. Mechanically unconstrained torque about the long Z axis induced by the unstable combination of magnetic fields causes the MCR to twist. This near 180° rotation of the plane of magnetization changes the profile of cross products and therefore magnetic body torques along the MCR. Deformation is thus reduced but also, the equilibrium calculations detailed in Section 5.2.1 are undermined. This results in a loss of correspondence, for the desired joint angles, in the elastic-magnetic torque balance of the MCR. The failures of both the tip driven and the unreinforced MCRs corroborate our claim that a torsionally reinforced catheter enables otherwise impossible shape-controlled, magnetic navigations.

The authors assumed, due to the successful implementation of the quasi-static assumption under insertion, that at a sufficiently low frequency, the operational code could simply be run backwards to give contact free *retraction*. As can be observed in the supporting video, for the larger deformation bile duct navigation, this is not true and significant phantom deformation occurs. The quasi-static assumption does not consider any driving force at the base of the MCR (as this would generate time dependency) which, for the retraction phase is clearly (and unexpectedly) critical. To address this interesting research question we believe the answer is to implement 'gradient pulling' - tangential pulling forces associated with magnetic field gradients.

We also anticipate developing a fabrication technique to produce narrower and more malleable braids to reduce bending stiffness $E_x$, $E_y$. Incorporated into this is the desire to better understand the theoretical role of the braid and its design parameters: material, helix angle, number and thickness of threads. We currently have a nylon braid wound at an angle of 35° from the longitudinal axis, but an unknown number and thickness of threads. Optimization of these parameters was explored in our earlier work on helical fiber support [18], but here we have utilized a commercial braid. As previously noted, this option offers a significant advantage in terms of miniaturization and reliability of fabrication but also exhibits major drawbacks in terms of control over these braid design parameters. By developing our own sub-millimetre scale braid fabrication we can optimize design parameters to further improve performance towards our target clinical application.

Finally, we also want to extend our demonstration into three dimensions to enable navigation through more convoluted routes such as those in the neurovascular network and deeper into the pancreas.

We have demonstrated a successful constraining of the twisting instability of MCRs under certain necessary configurations of magnetization and applied field. This has allowed us to achieve magnetically actuated, follow-the-leader navigation into an ultrasoft pancreatic phantom. This combination of large deformation and minimal reactive force has not previously been shown. With this contribution we have taken a significant step towards fulfilling the potential of shape forming MCRs for navigation through sensitive and convoluted anatomies in a safe, stable and repeatable manner.

## Bibliography

[1] J. Burgner-Kahrs, D. C. Rucker, and H. Choset, “Continuum robots for medical applications: A survey,” *IEEE Transactions on Robotics*, vol. 31, no. 6, pp. 1261–1280, 2015.

[2] P. E. Dupont, B. J. Nelson, M. Goldfarb, B. Hannaford, A. Menciassi, M. K. O’Malley, N. Simaan, P. Valdastri, and G.-Z. Yang, “A decade retrospective of medical robotics research from 2010 to 2020,” *Science Robotics*, vol. 6, no. 60, p. eabi8017, 2021. [Online]. Available: https://www.science.org/doi/abs/10.1126/scirobotics.abi8017

[3] Y. Kim and X. Zhao, “Magnetic soft materials and robots,” *Chemical Reviews*, vol. 0, no. 0, p. null, 0, pMID: 35104403. [Online]. Available: https://doi.org/10.1021/acs.chemrev.1c00481

[4] T. da Veiga, J. H. Chandler, P. Lloyd, G. Pittiglio, N. J. Wilkinson, A. K. Hoshiar, R. A. Harris, and P. Valdastri, “Challenges of continuum robots in clinical context: a review,” *Progress in Biomedical Engineering*, vol. 2, no. 3, p. 032003, aug 2020.

[5] L. Pancaldi, L. Noseda, A. Dolev, A. Fanelli, D. Ghezzi, A. J. Petruska, and M. S. Sakar, “Locomotion of sensor-integrated soft robotic devices inside sub-millimeter arteries with impaired flow conditions,” *Advanced Intelligent Systems*, vol. n/a, no. n/a, p. 2100247. [Online]. Available: https://onlinelibrary.wiley.com/doi/abs/10.1002/aisy.202100247

[6] J. Edelmann, A. J. Petruska, and B. J. Nelson, “Magnetic control of continuum devices,” *The International Journal of Robotics Research*, vol. 36, no. 1, pp. 68–85, 2017.

[7] Y. Kim, G. A. Parada, S. Liu, and X. Zhao, “Ferromagnetic soft continuum robots,” *Science Robotics*, vol. 4, no. 33, p. eaax7329, 2019.

[8] M. Hidalgo, S. Cascinu, J. Kleeff, R. Labianca, J.-M. Löhr, J. Neoptolemos, F. X. Real, J.-L. Van Laethem, and V. Heinemann, “Addressing the challenges of pancreatic cancer: future directions for improving outcomes,” *Pancreatology*, vol. 15, no. 1, pp. 8–18, 2015.

[9] M. Sugimoto, S. Takahashi, M. Kojima, N. Gotohda, Y. Kato, S. Kawano, A. Ochiai, and M. Konishi, “What is the nature of pancreatic consistency? assessment of the elastic modulus of the pancreas and comparison with tactile sensation, histology, and occurrence of postoperative pancreatic fistula after pancreaticoduodenectomy.” *Surgery*, vol. 156(5), p. 1204–1211, 2014.

[10] I. Levental, P. C. Georges, and P. A. Janmey, “Soft biological materials and their impact on cell function,” *Soft Matter*, vol. 3, pp. 299–306, 2007. [Online]. Available: http://dx.doi.org/10.1039/B610522J

[11] Y. Chitalia, S. Jeong, J. Bok, V. Nguyen, S. Melkote, J. J. Chern, and J. P. Desai, “Towards the design and development of a pediatric neuroendoscope tool,” in *2019 IEEE/RSJ International Conference on Intelligent Robots and Systems (IROS)*, 2019, pp. 2998–3004.

[12] E. Diller, J. Zhuang, G. Zhan Lum, M. R. Edwards, and M. Sitti, “Continuously distributed magnetization profile for millimeter-scale elastomeric undulatory swimming,” *Applied Physics Letters*, vol. 104, no. 17, p. 174101, 2014.

[13] G. Z. Lum, Z. Ye, X. Dong, H. Marvi, O. Erin, W. Hu, and M. Sitti, “Shape-programmable magnetic soft matter,” *Proceedings of the National Academy of Sciences*, vol. 113, no. 41, pp. E6007–E6015, 2016.

[14] P. Lloyd, A. K. Hoshiar, T. da Veiga, A. Attanasio, N. Marahrens, J. H. Chandler, and P. Valdastri, “A learnt approach for the design of magnetically actuated shape forming soft tentacle robots,” *IEEE Robotics and Automation Letters*, vol. 5, no. 3, pp. 3937–3944, 2020.

[15] M. Richter, V. K. Venkiteswaran, and S. Misra, “Multi-point orientation control

of discretely-magnetized continuum manipulators," *IEEE Robotics and Automation Letters*, vol. 6, no. 2, pp. 3607–3614, 2021.

[16] G. Pittiglio, P. Lloyd, T. da Veiga, O. Onaizah, C. Pompili, J. Chandler, and P. Valdastri, "Patient-specific magnetic catheters for atraumatic autonomous endoscopy," *Soft Robotics*, vol. ahead of print, no. ahead of print, p. ahead of print, 2022.

[17] P. Lloyd, G. Pittiglio, J. H. Chandler, and P. Valdastri, "Optimal design of soft continuum magnetic robots under follow-the-leader shape forming actuation," in *2020 International Symposium on Medical Robotics (ISMR)*, 2020, pp. 111–117.

[18] P. Lloyd, Z. Koszowska, M. Di Lecce, O. Onaizah, J. H. Chandler, and P. Valdastri, "Feasibility of fiber reinforcement within magnetically actuated soft continuum robots," *Frontiers in Robotics and AI*, vol. 8, 2021. [Online]. Available: https://www.frontiersin.org/article/10.3389/frobt.2021.715662

[19] L. Barducci, G. Pittiglio, J. C. Norton, K. L. Obstein, and P. Valdastri, "Adaptive dynamic control for magnetically actuated medical robots," *IEEE robotics and automation letters*, vol. 4, no. 4, pp. 3633–3640, 2019.

[20] R. J. Webster and B. A. Jones, "Design and kinematic modeling of constant curvature continuum robots: A review," *International Journal of Robotics Research*, vol. 29, no. 13, pp. 1661–1683, 2010.

[21] B. Siciliano, L. Sciavicco, L. Villani, and G. Oriolo, *Robotics: Modelling, Planning and Control.* Springer Publishing Company, Incorporated, 2010.

[22] F. Connolly, P. Polygerinos, C. J. Walsh, and K. Bertoldi, "Mechanical programming of soft actuators by varying fiber angle," *Soft Robotics*, vol. 2, no. 1, pp. 26–32, 2015.

[23] O. Strobel, J. Neoptolemos, D. Jäger, and M. Büchler, "Optimizing the outcomes of pancreatic cancer surgery." *Nat Rev Clin Oncol.*, vol. 16(1), pp. 11–26, 2019, pMID: 30341417.

[24] L. Blanc, A. Delchambre, and P. Lambert, "Flexible medical devices: Review of

controllable stiffness solutions," *Actuators*, vol. 6, no. 3, 2017. [Online]. Available: https://www.mdpi.com/2076-0825/6/3/23

[25] D. Teilum, "In vitro measurement of the length of the sphincter of oddi." *Endoscopy*, no. 23(3), p. 114–116, 1991.

[26] S. Horiguchi and T. Kamisawa, "Major duodenal papilla and its normal anatomy." *Dig Surg*, no. 27, pp. 90–93, 2010.

[27] H. Ismail, C. G. Pretty, M. Signal, M. Haggers, C. Zhou, and J. G. Chase, "Mechanical behaviour of tissue mimicking breast phantom materials." *Biomedical Physics & Engineering Express*, vol. 3, p. 045010, 2017.

[28] Z. Liu, M. Li, X. Dong, Z. Ren, W. Hu, and M. Sitti, "Creating three-dimensional magnetic functional microdevices via molding-integrated direct laser writing," *Nature Communications*, vol. 13, p. 2016, 2022.

# Chapter 6

# A Coiling, Variable Stiffness Soft Robot

**Chapter source:** Peter Lloyd, Theodosia Lourdes Thomas, Venkatasubramanian Kalpathy Venkiteswaran, Giovanni Pittiglio, James H Chandler, Pietro Valdastri, and Sarthak Misra, "A Magnetically-Actuated Coiling Soft Robot with Variable Stiffness". Under review. Submitted to IEEE Robotics and Automation Letters, October 2022.

## Abstract

Soft and flexible magnetic robots have gained significant attention in the past decade. These robots are fabricated using magnetically-active elastomers, are capable of large deformations, and are actuated remotely thus allowing for small robot size. This combination of properties is appealing to the minimally invasive surgical community, potentially allowing navigation to regions of the anatomy previously deemed inaccessible. Due to the low forces involved, one particular challenge is functionalizing such magnetic devices. To address this limitation we introduce a variable stiffness robot controlled by remote magnetic actuation, capable of grasping objects of varying sizes. We demonstrate a controlled and reversible high deformation coiling action induced via a transient homogeneous magnetic field and a synchronized sliding nitinol backbone. Our soft magnetic coiling grasper is visually tracked and controlled in closed-loop during three experimental demonstrations. We exhibit a maximum coiling deformation angle of 400°.

## 6.1 Introduction

Soft magnetic robots, due to an inherent reduction in traumatic anatomical forces, display the potential to supersede traditional mechanically-actuated surgical catheters [1] [2] [3]. The ability of these robots to maneuver through delicate and critical anatomy in a minimally invasive manner is key to improving the feasibility and success of many treatments [4]. Magnetic actuation allows devices to be composed of softer materials as forces and torques can be applied directly to embedded magnetic material as opposed to lengthwise force transmission [5] [6]. Furthermore, this class of rapid and clinically safe actuation eliminates the need for on-board power transmission systems (such as electrical or

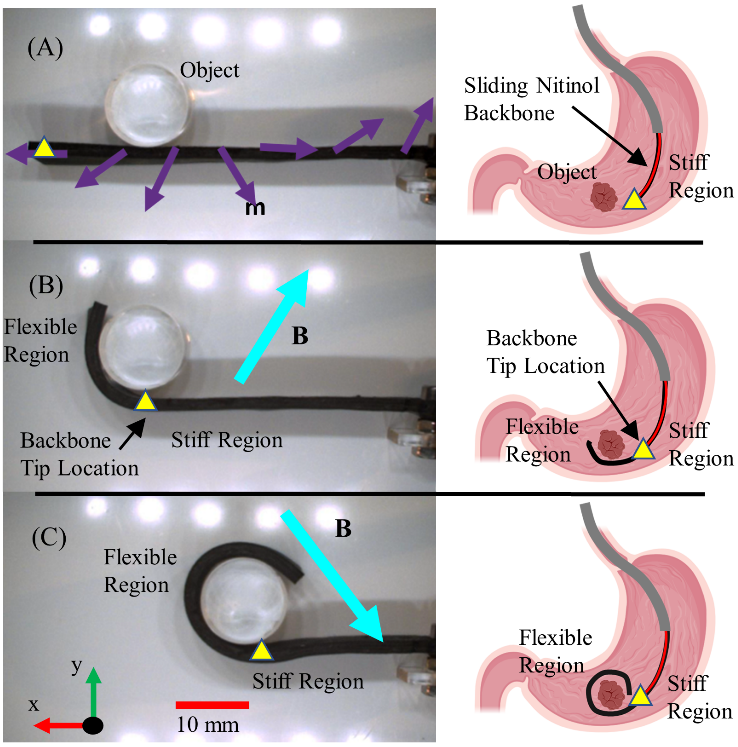

Figure 6.1: Three representative instances taken from the supporting video (left) shown alongside a clinically relevant application - grasping for removal of an excised stomach tumour (right). (A) The sliding nitinol backbone is fully inserted (tip of backbone shown as yellow triangle on the left and red overlay on the right) - the stiff region will not respond to actuation. Magnetization (**m**) is shown here by purple arrows. (B) The wire-frame is partially retracted allowing deformation of the "Flexible Region". This is actuated via a homogeneous magnetic field (**B**) shown as the turquoise arrows. The "Stiff Region" retains its backbone support. (C) The wire-frame is further retracted as the applied field is rotated. This grasping pose would be unachievable without the sliding nitinol backbone.

pneumatic) allowing easy miniaturization [7].

In order to introduce shape-programmability, magnetically-hard particles with high coercivity can be incorporated into mechanically soft materials capable of large deformations [8] [9] [10]. This system is capable of creating complex time varying shapes at small scales as magnetic field control inputs can be specified in magnitude, direction and spatial gradient [11]. Magnetic soft continuum structures can also be fabricated with a continuous lengthwise magnetization profile thus generating spatially resolved deformations [11]. A range of applications have been demonstrated using this approach [7] including, amongst other applications, autonomous navigating catheters [6], cilia-like shape forming structures [11], untethered swimmers [10], shape forming catheters [12] [13], and untethered grippers [14].

Softness represents a clear advantage for medical tools [15], however, this can also be problematic when it comes to performing functional tasks. As such, variable stiffness becomes a highly desirable feature such as the magnetic catheter with conductive shape memory polymer demonstrated in [16]. There are many approaches to achieve stiffening, most commonly; geometric changes such as modifying the cross-sectional profile, elastic changes such as phase transition or jamming and antagonistic actuation [17]. The typical motive for stiffening in continuum robots, however, is to shape-lock after actuation [18].

In this proof-of-concept work, we employ material variable stiffness in the form of a sliding nitinol backbone which offers a stiffness change factor of close to 800. This movement is synchronistically controlled within a closed-loop with a time-varying actuating field (Fig. 6.1) for the novel purpose of constraining some proximal length of our robot against deformation whilst we actuate the remaining distal length (Fig. 6.2). This allows us to apply otherwise unstable combinations of magnetization and actuating field to achieve a forward time marching deformation, fully dependent on the previous pose. Consequentially, we generate a higher strain energy equilibrium and achieve circular deformations greater than one full revolution.

We have applied this concept to the demonstrative example of coiling for cargo grasping or delivery. There is a clinical appetite for soft, miniaturizable retrieval and delivery systems for biopsy or therapeutic use [19] [20] [21], and this innovation moves us towards the development of variable stiffness for greater deformation potential under magnetic actuation.

The significant contribution of this work is the closed-loop actuation of a potentially unstable magnetic robot with variable stiffness. Synchronized actuation and variable stiffness combine to achieve stable, large deformation shape forming. To prove the necessity of the inclusion of the sliding nitinol backbone, we also demonstrate the unsuccessful actuation of the robot without the inclusion of stiffening wires. This system is implemented in an 80 mm long, 10 mm x 2 mm cross-section tongue-like robot which grasps

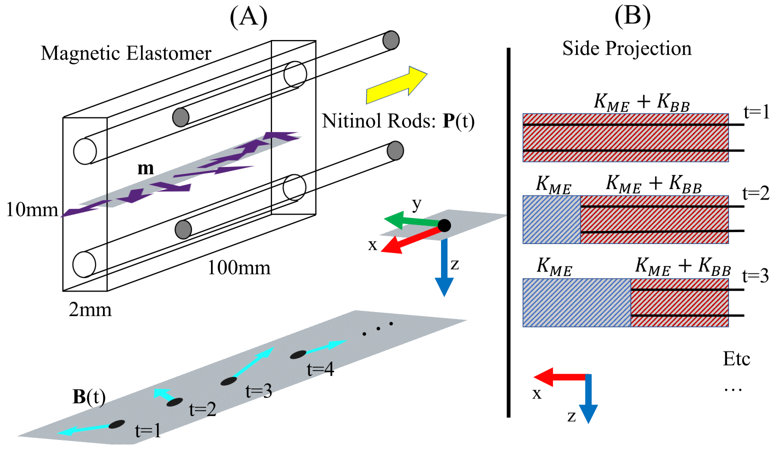

Figure 6.2: Schematic of the underlying design and actuation strategy. (A) The elastomer is magnetized (**m**), shown as purple arrows, in the x-y plane (shown in grey) in a spatially sinusoidal fashion along the length of the x-axis. A temporally sinusoidal actuating field (**B**(t), turquoise arrows) is applied (also in the x-y plane), as the nitinol rod backbone is withdrawn (**P**(t), yellow arrow). (B) This controlled augmentation of the unconstrained, and therefore lower stiffness, length of the VSR allows higher strain energy states to be achieved. $K_{ME}$ and $K_{BB}$ are the elastic stiffness of the magnetic elastomer and the nitinol backbone, respectively.

and releases arbitrary objects via coiling.

## 6.2 The Variable Stiffness Robot

In this section, we detail the analytical design principles, the fabrication technique and the dual material characterization of our tongue-like, variable stiffness robot (VSR).

### 6.2.1 Analytical Design - Elastic Torque

We represent the flexible, unsupported region of the VSR as a serial chain of rigid links connected by planar (1 Degree of Freedom) rotational joints as a simplification of [22] and [23]. Any desired shape can be represented as a vector of joint angles $\mathbf{q}$ where the length of $\mathbf{q}$ is determined by the granularity of discretization (individual link length $l$) and the unconstrained length of the VSR, itself a function of time ($L = L(t)$). Elastic joint torque is given as

$$\boldsymbol{\tau}_{elas} = \frac{K\mathbf{q}}{l}, \tag{6.1}$$

where $l$ is the virtual link length and $K$ is the elastic stiffness given by

$$K = E_{ME}I_{ME} + E_{BB}I_{BB}, \tag{6.2}$$

with $E_{ME}$ and $I_{ME}$ as the Young's modulus and the second moment of area for bending of the rectangular cross-section magnetic elastomer, and $E_{BB}$ and $I_{BB}$ are those of the circular cross-section backbone, respectively (See Fig. 6.2)

$$I_{ME} = \frac{wh^3}{12}, \tag{6.3}$$

$$I_{BB} = \frac{n\pi}{4}r^4, \tag{6.4}$$

with $w$ as the elastomer width, $h$ as the elastomer height, $r$ as the radius of the support rods, and $n$ as the number of support rods. When the nitinol backbone is withdrawn $E_{BB} = 0$ and the mechanical stiffness drops dramatically.

### 6.2.2 Analytical Design - Magnetic Torque

A magnetic dipole with moment $\mathbf{m}$ in a homogeneous field $\mathbf{B}(\mathrm{t})$ will experience a resultant magnetic torque proportional to applied field strength

$$\boldsymbol{\tau}_{mag}(t) = \mathbf{m} \times \mathbf{B}(t), \tag{6.5}$$

where $\mathbf{B}(\mathrm{t})$, $\mathbf{m}$, $\boldsymbol{\tau}_{mag}(t) \in \mathbb{R}^3$ (If $\mathbf{B}$ and $\mathbf{m}$ are constrained to the x-y plane then the cross product becomes *effectively* scalar). The body torque acting on any discretized segment (virtual link) of the VSR as a consequence of the interaction of the actuating magnetic field, and the *deformed* magnetization of that region of doped elastomer will produce deformation, and therefore be counteracted by the elastic properties of the material.

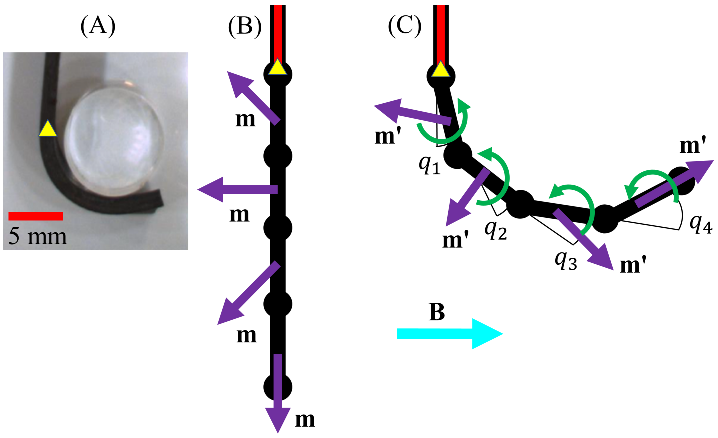

Figure 6.3: (A) A representative pose of the VSR with the tip location of the sliding nitinol backbone indicated by the yellow triangle and the backbone supported region shown as red overlay. (B) Illustratively discretized into four rigid links with referential magnetizations (**m**) shown as purple arrows. (C) Deformed magnetization (**m'**) shown again as purple arrows, resultant magnetic torques as green arrows, applied field (**B**) as turquoise arrow and deformed joint angles as $q_i$, $i \in [1, 4]$.

### 6.2.3 Analytical Design - Torque Balance

Assuming gravity to be zero, we can balance the elastic torque at any given virtual joint ($i$, in a VSR of $N$ virtual joints) with the aggregation of magnetic torques on every distal virtual link in the VSR at any given time step

$$\tau_{i,elas} = \sum_{n=i}^{N} \boldsymbol{\tau}_{n,mag}. \tag{6.6}$$

As illustrated in Fig. 6.3, we can define our desired shape as some proportion of a circle. The joint array $q$ for a full circle of deformation becomes $N$ equal joints of $\frac{360}{N}^{\circ}$, where $q$ increases in length by one entry with each time step from $t = 0$ to $t = N$. Anything proximal to the joint of interest will be constrained by the backbone and is assumed to be rigid (See Section 6.2.5).

Inverting the aggregation of (6.6) over all time steps would give non-unique solutions for **m** and **B** - the necessary combination of fields and magnetizations can be rotated about z whilst still producing feasible outputs. By implementing constraints (which in practice, aid stability) namely, the distal magnetization must be axial and all segment magnetizations must be within 60° of all their neighboring magnetizations, a unique solution exists for any set of joint angle arrays. This solution was determined using the Genetic Algorithm (GA, Global Optimization Toolbox, Matlab version R2021b) to generate discretized magnetization profiles and time-stepping actuating fields.

As can be observed in Fig. 6.2 and Fig. 6.3, these resultant magnetizations and actuating fields are sinusoidal in nature. The magnetization sinusoid running spatially along the long (x) axis of the robot and the actuating field sinusoid rotating as a function of time.

The driving variable here is the *bending radius* ($r$) and is defined as the radius of the circle which is formed by the array of equal desired joint angles, so, taking $q_{des}$ as a scalar from the joint angle array and with $l$ as the virtual link length gives

$$r = \frac{l}{2\sin\left(q_{des}\right)}. \tag{6.7}$$

Consequentially, defining position along the robot length from the tip as $S$, the magnetization ($\mathbf{m}$) at any point along the robot is defined as

$$\mathbf{m} = |\mathbf{m}|\text{rot}_z(\frac{S}{\pi r}180°)\hat{\mathbf{x}}, \tag{6.8}$$

with $\hat{\mathbf{x}}$ the unit vector in the x direction, and $\text{rot}_z(\cdot) \in SO(3)$ the rotation matrix about the z-axis. The resultant rotational speed of the actuating field is a function of the speed

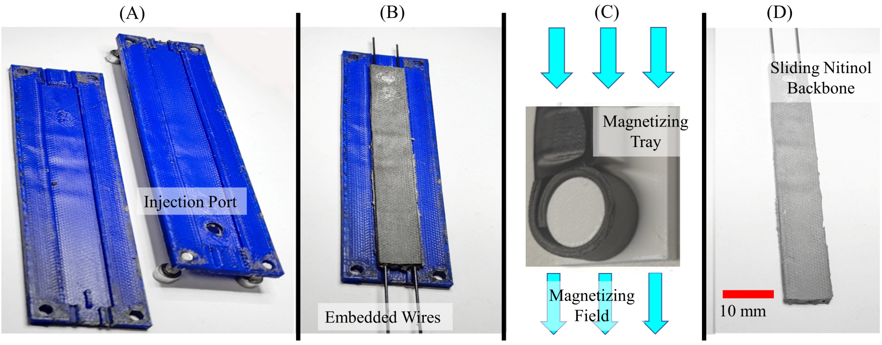

Figure 6.4: The key steps in the process of fabrication. (A) A mold is 3D printed in Polylactic acid. The injection port can be seen here. (B) 0.75 mm diameter nitinol wires are embedded lengthways and doped silicone is injected and cured. (C) The specimen is demolded, wrapped around a magnetizing tray (shown in grey) of specific bending radius and exposed to a saturating magnetizing field, shown here as turquoise arrows. (D) 0.5 mm diameter nitinol wires are inserted to act as the sliding backbone.

of retraction of the backbone.

### 6.2.4 Fabrication

The manual fabrication process is outlined in Fig. 6.4 and is based on [12]. A split mold was 3D printed (RS-F2-GPGR-04, Formlabs, USA) into which 0.75 mm diameter nitinol wires are embedded, and the arrangement is bolted and glued shut. The elastomer (Ecoflex-0030, Smooth-On Inc, USA) was mixed with neodymium-iron-boron (NdFeB) microparticles with an average diameter of 5 µm (MQFP-B+, Magnequench GmbH, Germany) in a 1:1 mass ratio giving a saturated remnance of 120 mT [24]. This composite was mixed and degassed in a high vacuum mixer (ARV-310, THINKYMIXER, Japan) at 1400 rpm, 20.0 kPa for 90 seconds. The mixture was injected into the mold and cured at room temperature for four hours. Upon demolding, the 0.75 mm diameter nitinol rods are removed.

The specimens were then secured in a circular 3D printed magnetizing mold before being subjected to a saturating uniform field of 4.644 T (ASC IM-10-30, ASC Scientific, USA). The bending radius of the circle about which the specimen is wrapped during magnetization is described in Section 6.2.3 and discussed in Section 6.5. For Sample 1 this parameter was 7.5 mm and for Sample 2 it was 5 mm.

Finally, the holes from which the 0.75 mm diameter rods were removed are filled with free sliding 0.5 mm diameter nitinol backbone rods.

### 6.2.5 Variable Stiffness Characterization

Using Ecoflex-0030 (Smooth-On Inc, USA) doped at 100% by weight gives $E_{ME}$ = 100 kPa [24]. $E_{BB}$ = 50 GPa [25] and from (6.3) and (6.4) with $w$ = 2 mm, $h$ = 10 mm, $r$ = 0.25 mm and n = 2 gives the elastic stiffness of the nitinol backbone ($K_{BB}$) and the magnetic elastomer ($K_{ME}$) as

$K_{BB} = 3 \times 10^{-4}$ Nm$^2$,

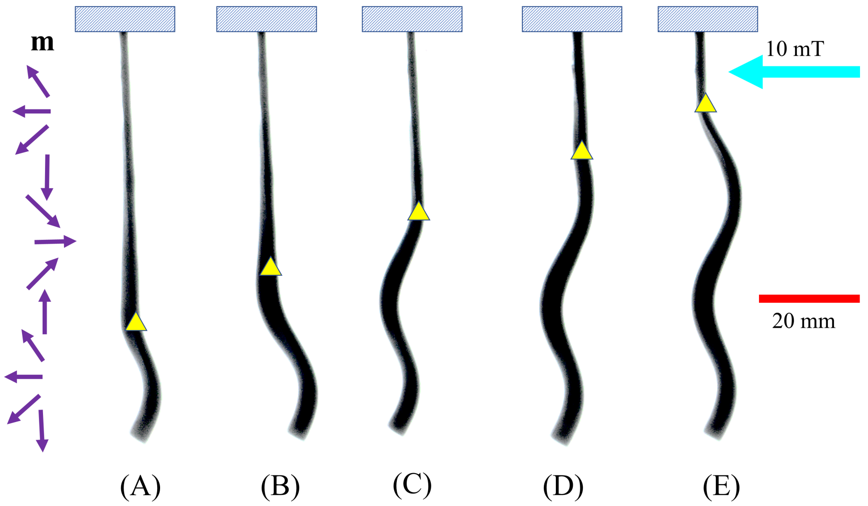

Figure 6.5: The variable stiffness robot (VSR), magnetized according to the purple arrows (**m**) and constrained at the base (blue rectangles), is shown under static one-dimensional magnetic actuation (turquoise arrow) for various insertions of sliding nitinol backbone signified here by yellow triangles. (A) Distal 20 mm unconstrained. (B) Distal 30 mm unconstrained. (C) Distal 40 mm unconstrained. (D) Distal 50 mm unconstrained. (E) Distal 60 mm unconstrained. Due to the stiffness change factor, deformation can only occur in the unconstrained region of the VSR. This shows the lowest energy state of the sinusoidally magnetized VSR.

$K_{ME} = 7 \times 10^{-7}$ Nm$^2$.

This gives an analytical stiffness change factor of 765. In practice, no amount of actuating field could be imparted in order to generate a measurable bending deformation in the backbone supported region of the VSR. Fig. 6.5 shows the VSR in a static actuating field with incrementally adjusted support positions - the point at which the backbone reaches is marked with a yellow triangle. This clearly demonstrates the absence of bending in any of the proximal, supported regions. Furthermore, Fig. 6.5 shows the lowest energy state of the sinusoidally magnetized VSR. Without forcing the robot into the coiled higher energy state using correctly coupled backbone retraction *and* time-varying applied fields we cannot achieve the large deformations with which we functionalize the system. The supporting video: S1 also illustrates the failure of the VSR to coil around an object and uncoil when the actuating field is applied sinusoidally but the sliding nitinol backbone is absent.

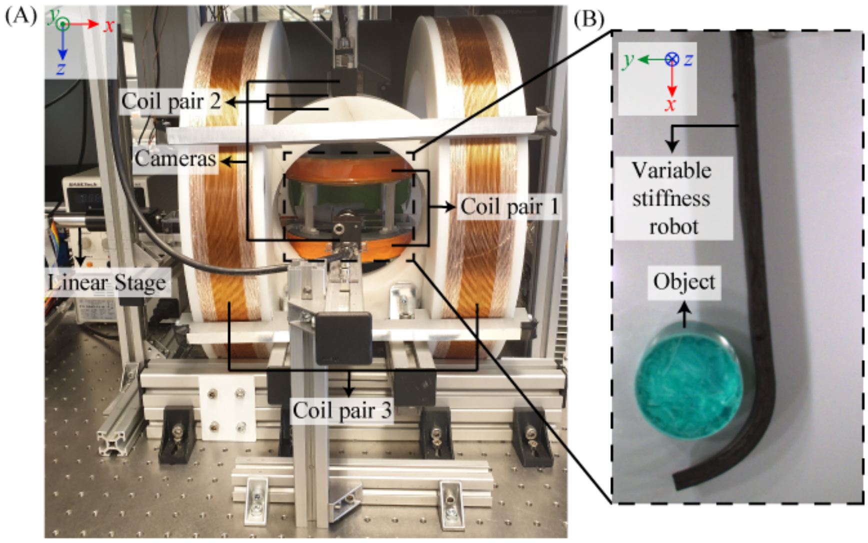

Figure 6.6: The actuation system showing (A) PaCMag - 3D electromagnetic coil setup and the linear stage. (B) Top view of the variable stiffness robot grasping an object in the workspace.

## 6.3 Controlled Actuation

In this section, we demonstrate a proof-of-concept functionalization of our VSR. By synchronizing the withdrawal of the backbone support with the rotation of the actuating field we force the VSR to coil into a higher energy state equilibrium. We use this coiling action to grasp various objects.

### 6.3.1 Actuation Systems

A 3-D electromagnetic coil setup (PaCMag) is used with a cylindrical workspace of equal radius and height of 65 mm as shown in Fig. 6.6 [26]. It has three coil pairs which can generate linearly independent uniform magnetic fields up to 55 mT. Experiments are conducted by supporting the VSR horizontally in the workspace of PaCMag and a linear stage (LX20, Misumi Group Inc., Tokyo, Japan) fixed at the base controls the movement of the nitinol backbone. A camera situated at the top captures the motion of the VSR.

### 6.3.2 Visual Sensory Feedback

An image processing algorithm is developed in OpenCV to track the tip angles of the VSR in 2D using camera images. Firstly, the original image is converted to a grayscale image and a threshold operation is performed to obtain a binary image of the VSR. Secondly, a skeletonization algorithm is performed on the binary image to extract the shape of the VSR. The tip of the VSR is then identified as the end point of the skeleton. Lastly, the slope of the end segment is calculated to find the tip angle of the VSR, this is used as feedback for the closed-loop controller.

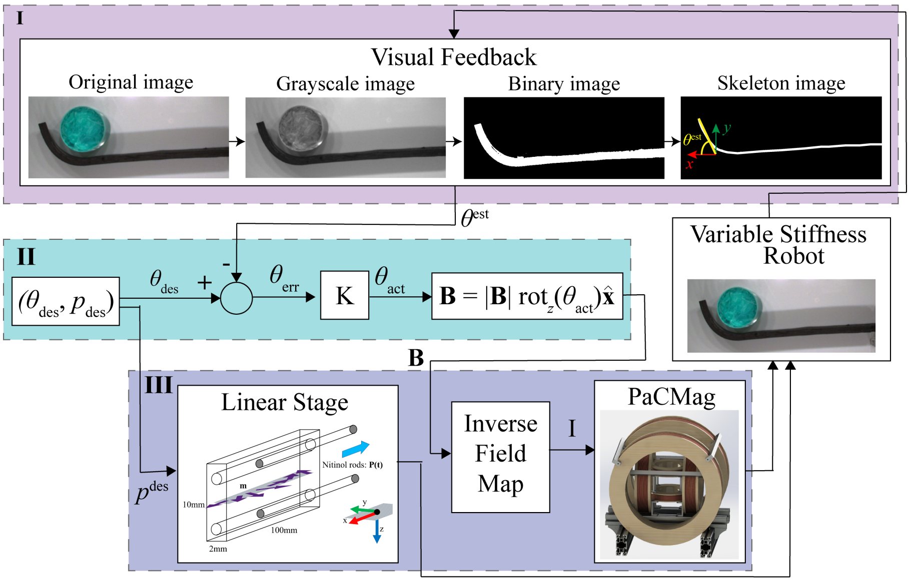

Figure 6.7: Closed-loop control of the variable stiffness robot (VSR) summarized in three blocks: (I) The tip angle ($\theta_{\text{est}}$) of the VSR is estimated from the camera and sent as feedback to the controller. (II) A proportional control calculates the magnetic field ($\mathbf{B}$) and its angle ($\theta_{\text{act}}$) to be applied from the error ($\theta_{\text{err}}$) between the desired ($\theta_{\text{des}}$) and estimated ($\theta_{\text{est}}$) tip angles. (III) PaCMag applies the magnetic field by computing the required current (I) from the inverse field map. The linear stage moves the nitinol backbone to a position ($p_{\text{des}}$) updated based on the current desired tip angle ($\theta_{\text{des}}$).

### 6.3.3 Calculation of Actuating Field

We implemented a linear proportional controller with manually optimized gain parameters. The one dimensional error function is derived as the difference between the estimated tip angle ($\theta_{\text{est}} \in \mathbb{R}^1$) from Section 6.3.2 and the desired tip angle ($\theta_{\text{des}} \in \mathbb{R}^1$). This desired tip angle is predefined as a vector assembled from a circle discretized into small

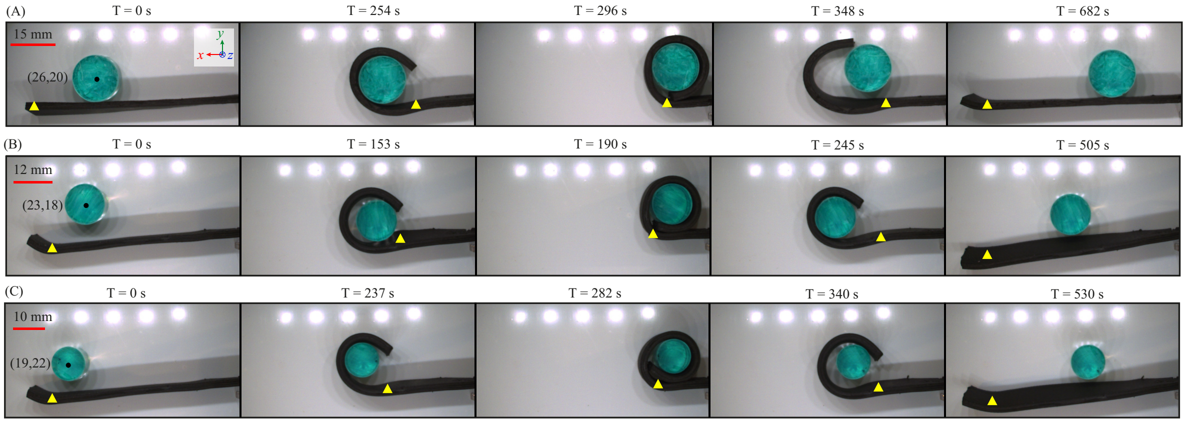

Figure 6.8: Closed-loop control demonstration of grasping and releasing objects placed at arbitrary locations and shown at different time instants ($t$) for three cases: (A) Sample 1 with 15 mm diameter object. (B) Sample 2 with 12 mm object. (C) Sample 2 with 10 mm object. The four stages of the experiment occur between the successive time snippets in the following order: grasping phase; coiling action; uncoiling action; releasing phase. The yellow triangle represents the tip position of the nitinol backbone. Please refer to the supporting video: S3-S5 for the complete demonstration.

increments, for example, $\theta_{\text{des}} = [10, 24, 38, ..., 206, 220]^{\circ}$. The actuating field ($\mathbf{B} \in \mathbb{R}^3$) is set to a constant magnitude ($|\mathbf{B}| = 20$ mT) and the control variable is the angle of the applied field ($\theta_{\text{act}}$) relative to the x-axis (see Fig. 6.7).

$$\mathbf{B} = |\mathbf{B}|\text{rot}_z(\theta_{\text{act}})\hat{\mathbf{x}}. \tag{6.9}$$

The applied field angle at time ($t$) is updated according to the error function ($\theta_{err} = \theta_{\text{des}} - \theta_{\text{est}}$) until the tolerance ($\theta_{err} < 5^{\circ}$) is attained as shown below,

$$\theta_{\text{act}}(t) = \text{K}_{\text{P}}\theta_{\text{err}}(t) + \theta_{\text{act}}(t-1), \tag{6.10}$$

where $\text{K}_{\text{P}}$ is the proportional gain. The system then retracts the nitinol backbone one increment before advancing to the next desired tip angle.

### 6.3.4 Calculation of Retracting Stage Position

The time-varying position of the nitinol backbone $\big(P(t)\big)$ is defined as: $P(t) = L - p_{\text{des}}(t)$, where $L$ is the total robot length and the incremental position ($p_{\text{des}}(t)$) is linearly correlated to the desired angle of deformation ($\theta_{\text{des}}(t)$) via the bending radius ($r$, the

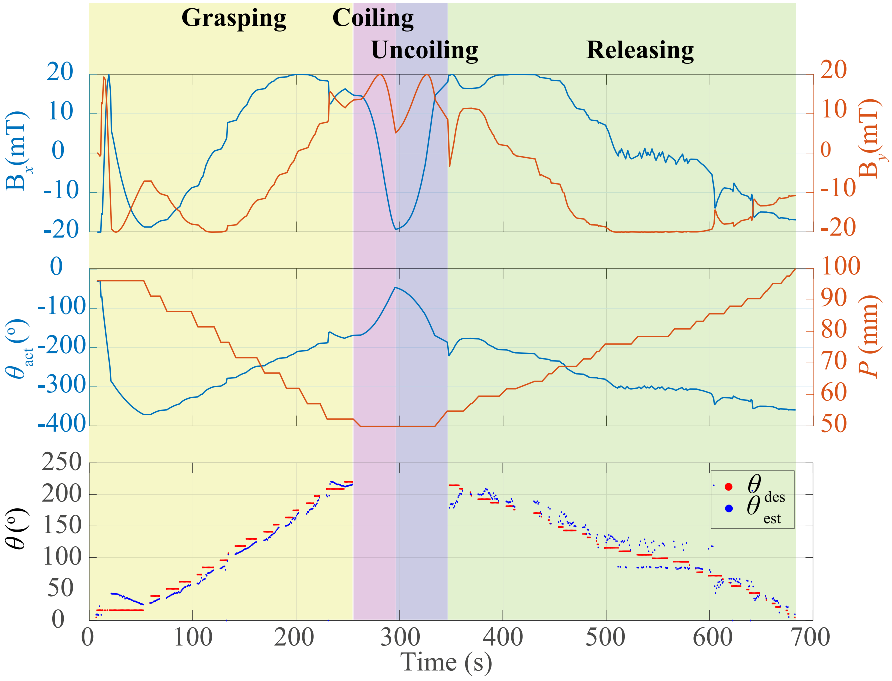

Figure 6.9: Results of closed-loop control experiment of Sample 1 grasping and releasing 15 mm object. Plots show the applied magnetic field ($\mathrm{B}_x$, $\mathrm{B}_y$) and its orientation ($\theta_{\text{act}}$), position of the nitinol backbone ($P$), the desired ($\theta_{\text{des}}$) and estimated ($\theta_{\text{est}}$) tip angles of the VSR during the experiment time ($t$). The four stages of the experiment occur as follows: grasping phase ($t$ = 0-254 s); coiling action ($t$ = 255-296 s); uncoiling action ($t$ = 297-348 s); releasing phase ($t$ = 349-682 s).

radius the VSR coils about during actuation).

Due to the limitation on positioning repeatability of the linear stage, $p_{des}(t)$ is set to a minimum step size of 2.5 mm. The VSR grasps the object placed in the coiling plane as PaCMag applies the magnetic field and the linear stage retracts the nitinol backbone until the set maximum desired tip angle ($\theta_{\text{des}}^{\text{max}} = 220°$) is reached. Beyond this angle as the tip closes the circle, it is not possible to track the tip angle. Hence, the subsequent coiling action is performed by automatically incrementing $\theta_{\text{des}}$ to complete the grasp. This whole system can also be run in reverse to uncoil the VSR and release the entrapped object. Fig. 6.7 illustrates the complete closed-loop control system.

## 6.4 Results

The two VSR samples 1 (7.5 mm bending radius) and 2 (5 mm bending radius) are used to demonstrate the grasping and releasing of printed cylindrical objects in closed-loop as shown in Fig. 6.8. Three objects of diameters 15, 12 and 10 mm are placed at various locations facing the coiling side of the VSR. The VSR, initially in its straight configuration, wraps around the object to grasp it, coils further to move the object along, then releases the object and uncoils itself to return to its original configuration (Refer to the supporting video: S3-S5 for the complete demonstration). Fig. 6.9 shows the plots of applied magnetic field ($B_x, B_y$), resultant field angle ($\theta_{\text{act}}$), position of the nitinol backbone ($P$), desired tip angle ($\theta_{\text{des}}$), and estimated tip angle ($\theta_{\text{est}}$). These variables are plotted for sample 1 grasping and releasing the 15 mm object (Fig. 6.8 A). The overall control frequency across the three experiments is 1 Hz. The PaCMag coils maintained closed-loop control of the VSR via the visual tip tracking system throughout the “Grasping" and “Releasing" phases of the demonstration (Fig. 6.9). Visual contact with the tip was lost during the “Coiling" and “Uncoiling" phases as discussed in Section 6.3.3. Here the controller was operating in open-loop. The observed maximum coiling deformation angle owing to the decreasing size of the objects in the three experiments were $360^o$, $375^o$ and $400^o$, respectively.

## 6.5 Discussions and Future Work

In this work, we have demonstrated the grasping and releasing under closed-loop control of various diameter cylinders using a variable stiffness magnetically-actuated continuum robot. In doing so we have addressed the non-trivial problem of controlling large (up to 400°) deformations which under magnetic actuation are inherently unstable. Please see the supporting video: S1 for the demonstration of a failed grasping and releasing experiment of the VSR without the nitinol backbone. We have introduced the concept of a synchronized sliding nitinol backbone with an applied actuating field and proved its feasibility within our VSR to grasp and release various objects. We have also shown that the VSR is able to coil itself into higher energy state equilibrium without relying on anatomical contact forces or interaction with external environment [27]. Supporting video: S2 shows the coiling of the VSR in free space without the influence of any external object.

In order to simplify the demonstration of our feasibility study, we performed our experiments entirely in the horizontal plane (Fig. 6.8). The VSR is supported in the vertical direction on a smooth acrylic plate thus negating the effects of gravity. Although there are no theoretical issues with the consideration and incorporation of the gravitational force, these simplifications were made on purely practical grounds. Any future study should look to both consider gravity and to control the VSR in unconstrained three dimensional space.

A further simplification worthy of mention pertains to the visual tracking algorithm. Our system locates the tip of the VSR and derives the tip angle to use as a control input. When the VSR wraps into a full circle the tip ceases to be visible, rendering this method of tracking impossible. Any further study should therefore encode a system for tracking the position and size of the circle after a certain deformation angle is achieved. Further ahead, and for a more clinically relevant demonstration, visual tracking is not possible inside the human body so some non-visual sensing method (e.g. medical imaging or strain sensing) should be incorporated.

The bending radius is an interesting parameter worthy of mention here. The radius of the circle around which the robot is magnetized has a profound impact on the achievable radii of the wrapped robot under actuation. If this bending radius is too small the elastic torque will overpower the magnetic torque and the robot will snap open. This can be mitigated to a limited degree with a larger applied field magnitude. Furthermore, if the retraction of the nitinol backbone is not correctly synchronized with the rotation of the applied magnetic field, the actuation descends into the imbalances shown in Fig. 6.5 and the supporting video. Consequentially, the timing of the retraction of the sliding nitinol backbone is a function of the bending radius (the magnetization) and is enabled by having sufficient magnitude of applied field.

The most obvious limitation of this design is that the backbone is always, when present, straight and the base upon which the VSR is mounted is static. As magnetic actuation is an inherently small scale technology with its most likely applications in minimally invasive surgery (and similar) these constraints limit the current clinical relevance of the design. In order to navigate to any area of interest we should be soft, compliant and mobile. This limitations are by no means definitive however, and the imminent next step is to develop miniaturizable backbones with compliant behavior, either fluidically actuated or with phase changing materials. Further to this we must also develop a mobile mounting system, such as a manual endoscope to operate. We also anticipate developing more reliable and miniaturizable automated fabrication techniques. This will allow us to shrink the prototype and potentially incorporate more complex and interesting variable stiffness features.

## 6.6 Conclusion

This paper presents a proof-of-concept of a tongue-like, magnetic variable stiffness coiling robot. This system exploits variable lengthwise mechanical properties to achieve high deformation equilibrium in a way which has not previously been shown. We have demonstrated a closed-loop control strategy to grasp and release objects of varying sizes by synchronizing the sliding nitinol backbone of the robot with the actuating magnetic field. With this contribution we have demonstrated the currently untapped potential of functionalizing variable stiffness magnetically-actuated robots for higher energy state deformations. The variable stiffness grasping robot has potential as a surgical tool for applications in biopsy and grasping.

# Bibliography

[1] P. E. Dupont, B. J. Nelson, M. Goldfarb, B. Hannaford, A. Menciassi, M. K. O'Malley, N. Simaan, P. Valdastri, and G.-Z. Yang, "A decade retrospective of medical robotics research from 2010 to 2020," *Science Robotics*, vol. 6, no. 60, p. eabi8017, 2021.

[2] R. V. Martinez, J. L. Branch, C. R. Fish, L. Jin, R. F. Shepherd, R. M. D. Nunes,

Z. Suo, and G. M. Whitesides, “Robotic tentacles with three-dimensional mobility based on flexible elastomers,” *Advanced materials*, vol. 25, no. 2, pp. 205–212, 2013.

[3] J. C. Norton, P. R. Slawinski, H. S. Lay, J. W. Martin, B. F. Cox, G. Cummins, M. P. Desmulliez, R. E. Clutton, K. L. Obstein, S. Cochran, and P. Valdastri, “Intelligent magnetic manipulation for gastrointestinal ultrasound,” *Science Robotics*, vol. 4, no. 31, pp. 1–14, 2019.

[4] J. Burgner-Kahrs, D. C. Rucker, and H. Choset, “Continuum robots for medical applications: A survey,” *IEEE Transactions on Robotics*, vol. 31, no. 6, pp. 1261–1280, 2015.

[5] J. Edelmann, A. J. Petruska, and B. J. Nelson, “Magnetic control of continuum devices,” *The International Journal of Robotics Research*, vol. 36, no. 1, pp. 68–85, 2017.

[6] Y. Kim, G. A. Parada, S. Liu, and X. Zhao, “Ferromagnetic soft continuum robots,” *Science Robotics*, vol. 4, no. 33, p. eaax7329, 2019.

[7] T. da Veiga, J. H. Chandler, P. Lloyd, G. Pittiglio, N. J. Wilkinson, A. K. Hoshiar, R. A. Harris, and P. Valdastri, “Challenges of continuum robots in clinical context: a review,” *Progress in Biomedical Engineering*, vol. 2, no. 3, p. 032003, aug 2020.

[8] R. Zhao, Y. Kim, S. A. Chester, P. Sharma, and X. Zhao, “Mechanics of hard-magnetic soft materials,” *Journal of the Mechanics and Physics of Solids*, vol. 124, pp. 244–263, 2019.

[9] Y. Kim and X. Zhao, “Magnetic soft materials and robots,” *Chemical Reviews*, vol. 122, no. 5, pp. 5317–5364, 2022.

[10] E. Diller, J. Zhuang, G. Zhan Lum, M. R. Edwards, and M. Sitti, “Continuously distributed magnetization profile for millimeter-scale elastomeric undulatory swimming,” *Applied Physics Letters*, vol. 104, no. 17, p. 174101, 2014.

[11] G. Z. Lum, Z. Ye, X. Dong, H. Marvi, O. Erin, W. Hu, and M. Sitti,

"Shape-programmable magnetic soft matter," *Proceedings of the National Academy of Sciences*, vol. 113, no. 41, pp. E6007 LP – E6015, oct 2016. [Online]. Available: http://www.pnas.org/content/113/41/E6007.abstract

[12] G. Pittiglio, P. Lloyd, T. da Veiga, O. Onaizah, C. Pompili, J. Chandler, and P. Valdastri, "Patient-specific magnetic catheters for atraumatic autonomous endoscopy," *Soft Robotics*, 2022.

[13] P. Lloyd, O. Onaizah, G. Pittiglio, D. K. Vithanage, J. H. Chandler, and P. Valdastri, "Magnetic soft continuum robots with braided reinforcement," *IEEE Robotics and Automation Letters*, vol. 7, no. 4, pp. 9770–9777, 2022.

[14] J. Zhang, O. Onaizah, K. Middleton, L. You, and E. Diller, "Reliable grasping of three-dimensional untethered mobile magnetic microgripper for autonomous pick-and-place," *IEEE Robotics and Automation Letters*, vol. 2, no. 2, pp. 835–840, 2017.

[15] T. L. Thomas, V. Kalpathy Venkiteswaran, G. K. Ananthasuresh, and S. Misra, "Surgical Applications of Compliant Mechanisms: A Review," *Journal of Mechanisms and Robotics*, vol. 13, no. 2, 01 2021.

[16] Y. Piskarev, J. Shintake, C. Chautems, J. Lussi, Q. Boehler, B. Nelson, and D. Floreano, "A variable stiffness magnetic catheter made of a conductive phase-change polymer for minimally invasive surgery," *Advanced Functional Materials*, vol. 32, 05 2022.

[17] L. Blanc, A. Delchambre, and P. Lambert, "Flexible medical devices: Review of controllable stiffness solutions," *Actuators*, vol. 6, no. 3, 2017.

[18] M. Manti, V. Cacucciolo, and M. Cianchetti, "Stiffening in soft robotics: A review of the state of the art," *IEEE Robotics and Automation Magazine*, vol. 23, no. 3, pp. 93–106, 2016.

[19] Y. Dong, L. Wang, N. Xia, Z. Yang, C. Zhang, C. Pan, D. Jin, J. Zhang, C. Majidi, and L. Zhang, "Untethered small-scale magnetic soft robot with programmable

magnetization and integrated multifunctional modules," *Science Advances*, vol. 8, no. 25, p. eabn8932, 2022.

[20] S. Miyashita, S. Guitron, K. Yoshida, S. Li, D. D. Damian, and D. Rus, "Ingestible, controllable, and degradable origami robot for patching stomach wounds," in *2016 IEEE International Conference on Robotics and Automation (ICRA)*, 2016, pp. 909–916.

[21] T. Xu, J. Zhang, M. Salehizadeh, O. Onaizah, and E. Diller, "Millimeter-scale flexible robots with programmable three-dimensional magnetization and motions," *Science Robotics*, vol. 4, no. 29, p. eaav4494, 2019.

[22] "Shape and contact force estimation of continuum manipulators using pseudo rigid body models," *Mechanism and Machine Theory*, vol. 139, pp. 34–45, 2019.

[23] P. Lloyd, G. Pittiglio, J. H. Chandler, and P. Valdastri, "Optimal design of soft continuum magnetic robots under follow-the-leader shape forming actuation," in *2020 International Symposium on Medical Robotics (ISMR)*, 2020, pp. 111–117.

[24] T. Da Veiga, J. H. Chandler, G. Pittiglio, P. Lloyd, M. Holdar, O. Onaizah, A. Alazmani, and P. Valdastri, "Material characterization for magnetic soft robots," in *2021 IEEE 4th International Conference on Soft Robotics (RoboSoft)*, 2021, pp. 335–342.

[25] P. Lee, Y. Chen, J. Hu, and C. Chang, "Comparison of mechanical stability of elastic titanium, nickel-titanium, and stainless steel nails used in the fixation of diaphyseal long bone fractures," *Materials (Basel)*, vol. 11, pp. 1–11, 11 2018.

[26] T. L. Thomas, J. Sikorski, G. Ananthasuresh, V. K. Venkiteswaran, and S. Misra, "Design, sensing, and control of a magnetic compliant continuum manipulator," *IEEE Transactions on Medical Robotics and Bionics*, 2022.

[27] T. L. Bruns, K. E. Riojas, D. S. Ropella, M. S. Cavilla, A. J. Petruska, M. H. Freeman, R. F. Labadie, J. J. Abbott, and R. J. Webster, "Magnetically steered robotic insertion of cochlear-implant electrode arrays: System integration and first-

in-cadaver results," *IEEE robotics and automation letters*, vol. 5, no. 2, pp. 2240–2247, 2020.

# Chapter 7

# Conclusions

## 7.1 Conclusions and Future Work

In the four years since I started my research the tentacle project has traveled from very little existing at all to its current state of development. Being born from the Magnetic Flexible Endoscope project [1] [2] - a successful and well developed tip driven system - gave me access to considerable expertise in the magnetic actuation of surgical robots. The project in 2019 however had no modeling or simulation capability at all and no actuation system on which to perform experimental work. From that early position, fabrication methods to produce prototypes with all manner of geometric and material variation have been developed. I have developed a variety of models and simulations of this inherently complex magneto-elastic material, tailored to the specific project requirements at the time. Optimizations have been devised and refined for both primitive shapes and clinically relevant navigations. Soft and/or transparent phantoms have been produced of a variety of human organs and actuation systems to test and demonstrate all of the above have been developed.

As well as the inevitable volume of unpublished and yet to be published work, I personally have written the five articles included in this thesis and, equally as importantly, I have also collaborated on a further four publications with more being developed as will be outlined below.

As with any interesting project any answers only serve to reveal more questions and this is no exception. Next I will address a list of the major questions which I feel remain outstanding at this stage of the project and discuss any work which is currently ongoing or planned with each. Of course these questions will never all be answered and many more will arise but at this point in time, and notwithstanding any confidentiality issues, I feel this represents a fair summary of the current position and direction of travel of the tentacle project.

### 7.1.1 Magnetic Instability

The revelation of the twisting instability and its profound adverse effect on observed behaviour has led to two of the publications featured in this thesis, the only two such works so far on the subject. This area of investigation, I feel, is only just beginning to be explored. Anybody who tries to magnetize a catheter-like shape in a non-axial direction will experience this instability. There are a variety of ways to negotiate the problem, geometric anisotropy shows potential, material anisotropy has been presented above, adaptive control (e.g. [3]) is also a possibility. Assuming the material anisotropy approach is pursued, and in order that the true target of patient specific, task specific tentacles be achieved. Robust optimization methods followed by miniaturizable fabrication methods for these kinds of designs must be developed.

On a similar theme of magnetic stability, a snapping effect can be caused by an incremental build up of elastic strain. Imagine an axially magnetized, tip driven catheter is subjected to an axial actuating field which is slowly rotated in order to generate bending deformation. This bending will continue to increase as the field rotates, often to a very large deformation, before eventually the elastic restoring forces outweigh the magnetic torque and the catheter “snaps” back into a lower energy state. This characteristic behaviour has been captured by members of our research group. This snapping instability could potentially be harnessed as in [4] to generate significantly increased forces in order to, for example, penetrate tissue.

### 7.1.2 Functionalization

Functionalization of the tentacle is obviously a fundamental end goal of the project which thus far has only been touched upon. As mentioned above, magnetic snapping could be exploited for functional purposes but, perhaps more achievable (as demonstrated in Chapter 6), stiffening systems can also be implemented. Hybrid actuation methods (magnetic actuation plus phase change material or mechanical stiffening) have been demonstrated [5] [6] [7] but are problematic due to the lack of miniaturization potential of the secondary mode of actuation. One potential solution to this problem which is in its infancy here in the STORM lab is the idea of magnetic stiffening in a magnetically actuated manipulator.

Snapping and stiffening are still only steps on the road towards functionalization. The real challenges to come pertain to mounting tools on, or service channels through, the tentacle. Examples of these functional additions could be a biopsy lasso, an ultrasonic probe, an ablation laser, a fluid injection or a balloon stent delivery system. These are all options which would enhance both the practical difficulty and the clinical appeal of any prospective future publications.

### 7.1.3 Miniaturization

The motivation for magnetic actuation over alternative, often simpler or more stable, actuation modes is an innate ability to be miniaturized. In order for this advantage to be realized, manufacturing must improve significantly. It is almost certain that the preferred future manufacturing method will be 3D printing of soft material and already there are many publications in this area (e.g. [8] [9]). We have an ongoing work-stream at Leeds University to address this unmet need however, referring again to the likely need for embedded material anisotropy (Section 7.1.1), this could prove to be a very challenging problem. As such, coherently connecting the needs of the soft robotics community with the capabilities of the manufacturing community will prove to be one of the major challenges facing our area of research in the coming years.

### 7.1.4 Simulation and Modeling

The difficulties associated with simulation and modeling of soft magnetic domains are well documented and have been discussed in this thesis. The trade-off between accuracy of assumptions and computational time will never be eradicated, in fact, as our project moves toward the development of adaptive control models this problem becomes more critical. As we learn more about how and where we can simplify these magnetic domain models without major accuracy losses (and as our computers become faster) we will converge on real-time capability. There is however a workstream within our lab looking at a more radical solution to this problem with the development of a differentiable numerical model. Time will tell if this approach proves effective in closing the current gap between physical realism and real-time optimizability.

### 7.1.5 Magnetic Field Gradient Pulling

It has been suggested to me by a clinician that the top innovation she would like to see in our research area is a magnetic field gradient pulled catheter. This, as opposed to a mechanically pushed system, would permit softer material (as buckling would no longer be relevant) and could potentially eradicate the current risk of tissue perforation during navigation. There have been studies on gradient pulled magnetic catheters [10] as well as studies on the simultaneous and independent actuation of both torque generated via magnetic field and force generated via field gradient [11]. The recurring challenge appears to be the magnitude gap between torques and forces. In general, the effect of field induced magnetic torques will greatly outweigh the effects of any gradient induced magnetic forces. Despite this challenge, it is likely that a gradient force can still contribute materially towards the forward motion of the tentacle. Particularly in the scenario that tangential friction is close to zero due to successful transient shape forming and some kind of hydrophobic, friction minimizing coating (as discussed below).

### 7.1.6 Other Areas

For clinical trials and beyond, the tentacle must be coated. This would address concerns surrounding both the bio-incompatibility of NdFeB and the high friction of silicone. Any coating must be sufficiently thin and flexible to not adversely affect the bulk material behavior of the tentacle whilst durable enough to not rupture during navigation. Protective, low friction coatings have been successfully demonstrated for similar applications [12] and we have an ongoing collaborative investigation into the feasibility of nano-film coatings.

As a robotics research laboratory we always have an interest in autonomy and therefore closed loop control [3]. We are yet to demonstrate closed loop shape forming control with the tentacle. This is attributable to two major factors, the first that we only relatively recently developed a system which navigates in open loop so haven't yet had time to develop a controller. The second being the non-linear behavior and multi-dimensional nature of the feedback makes this a technically challenging problem. Body shape must be reduced into some parametric form and then mapped into actuation parameters. Notwithstanding this, we are currently addressing this problem as a central priority and hope to produce a functional adaptive controller in the near future.

The issue of sensing within the human body has long been of concern. Our demonstrations to date have exploited visual feedback but in order that any closed loop controller can operate in a clinical setting this must change. Magnetic Resonance Imaging (MRI) revolutionized the conversation on sensing but sadly cannot (currently) be exploited in conjunction with magnetic actuation. There is work ongoing looking at alternative methods of sensing - strain gauges, fibre Bragg gratings and ultrasonic sensors - with a view to closing the control loop without visual or potentially carcinogenic X-ray feedback. This is one of the most challenging and potentially rewarding areas of development for the tentacle team. As a long range aspiration it is also worth noting the theoretical possibility of operating the tentacle under magnetic actuation whilst being simultaneously or alternately (at very high frequency) monitored inside a modified MRI machine.

So far, path planning tasks have been performed in a utilitarian manner. In [13] and [14] anatomical data was accessed from open-source datasets. One of the initial ambitions of the project was for tentacles to display bespoke magnetic signatures designed as a function of the pathway from access point to destination of the specific patient in question. This would involve pre-operative imaging feeding into the path planning and magnetic optimization phases of the process. Some research of this nature has taken place in the STORM lab but as yet remains unpublished. Whilst still an ongoing ambition, incorporating pre-operative imaging into a robust, patient specific optimization process remains out of scope for the current workstreams.

The idea that follow-the-leader shape forming motion does indeed reduce patient trauma, whilst instinctively logical, remains as yet, an open question, and one which it would certainly be helpful to answer. Any clarification of this would be complicated by the extremely low (sub milli-Newton-meter torques [15]) forces involved and the enormously complex interrelation between navigational contact forces and the soft, living tissue through which they pass [16]. Notwithstanding this open question, it is the belief of the author, the principal investigator, the grantees and many other relevant specialists that this technology will prove to be of value in the long term. We would all benefit however from a more objective answer to this question.

This PhD thesis lists my achievements to date within the framework of the tentacle project. These achievements are a scratch on the surface of the ever growing list of unanswered questions and potential future contributions within this specific field. Hopefully, with high impact future research efforts from myself and from the rest of the team we can continue to move the project towards its ultimate goal of designing patient specific magnetically actuated tentacle robots for life saving and life improving minimally invasive surgery.

# Bibliography

[1] J. C. Norton, P. R. Slawinski, H. S. Lay, J. W. Martin, B. F. Cox, G. Cummins, M. P. Desmulliez, R. E. Clutton, K. L. Obstein, S. Cochran, and P. Valdastri, "Intelligent magnetic manipulation for gastrointestinal ultrasound," *Science Robotics*, vol. 4, no. 31, pp. 1–14, 2019.

[2] J. W. Martin, B. Scaglioni, J. C. Norton, V. Subramanian, A. Arezzo, K. L. Obstein, and P. Valdastri, "Enabling the future of colonoscopy with intelligent and autonomous magnetic manipulation," *Nature machine intelligence*, vol. 2, no. 10, pp. 595–606, 2020.

[3] L. Barducci, G. Pittiglio, J. C. Norton, K. L. Obstein, and P. Valdastri, "Adap-

tive dynamic control for magnetically actuated medical robots," *IEEE robotics and automation letters*, vol. 4, no. 4, pp. 3633–3640, 2019.

[4] B. Gorissen, D. Melancon, N. Vasios, M. Torbati, and K. Bertoldi, "Inflatable soft jumper inspired by shell snapping," *Science Robotics*, vol. 5, no. 42, p. eabb1967, 2020. [Online]. Available: https://www.science.org/doi/abs/10.1126/scirobotics.abb1967

[5] Y. Piskarev, J. Shintake, C. Chautems, J. Lussi, Q. Boehler, B. Nelson, and D. Floreano, "A variable stiffness magnetic catheter made of a conductive phase-change polymer for minimally invasive surgery," *Advanced Functional Materials*, vol. 32, 05 2022.

[6] L. Blanc, A. Delchambre, and P. Lambert, "Flexible medical devices: Review of controllable stiffness solutions," *Actuators*, vol. 6, no. 3, 2017. [Online]. Available: https://www.mdpi.com/2076-0825/6/3/23

[7] M. Manti, V. Cacucciolo, and M. Cianchetti, "Stiffening in soft robotics: A review of the state of the art," *IEEE Robotics and Automation Magazine*, vol. 23, no. 3, pp. 93–106, 2016.

[8] Y. Kim, H. Yuk, R. Zhao, S. A. Chester, and X. Zhao, "Printing ferromagnetic domains for untethered fast-transforming soft materials," *Nature*, vol. 558, no. 7709, p. 274, 2018.

[9] Z. Liu, M. Li, D. X, Z. Ren, W. Hu, and M. Sitti, "Creating three-dimensional magnetic functional microdevices via molding-integrated direct laser writing," *Nat Commun*, vol. 13, no. 2016, 2022.

[10] B. J. Nelson, S. Gervasoni, P. W. Chiu, L. Zhang, and A. Zemmar, "Magnetically actuated medical robots: An in vivo perspective," *Proceedings of the IEEE*, 2022.

[11] V. K. Venkiteswaran and S. Misra, "Towards gradient-based actuation of magnetic soft robots using a six-coil electromagnetic system," in *2020 IEEE/RSJ International Conference on Intelligent Robots and Systems (IROS)*, 2020, pp. 8633–8639.

[12] Y. Kim, G. A. Parada, S. Liu, and X. Zhao, "Ferromagnetic soft continuum robots," *Science Robotics*, vol. 4, no. 33, p. eaax7329, 2019.

[13] P. Lloyd, O. Onaizah, G. Pittiglio, D. K. Vithanage, J. H. Chandler, and P. Valdastri, "Magnetic soft continuum robots with braided reinforcement," *IEEE Robotics and Automation Letters*, vol. 7, no. 4, pp. 9770–9777, 2022.

[14] G. Pittiglio, P. Lloyd, T. da Veiga, O. Onaizah, C. Pompili, J. Chandler, and P. Valdastri, "Patient-specific magnetic catheters for atraumatic autonomous endoscopy," *Soft Robotics*, 2022.

[15] J. J. Abbott, O. Ergeneman, M. P. Kummer, A. M. Hirt, and B. J. Nelson, "Modeling magnetic torque and force for controlled manipulation of soft-magnetic bodies," *IEEE Transactions on Robotics*, vol. 23, no. 6, pp. 1247–1252, 2007.

[16] V. K. Venkiteswaran, J. Sikorski, and S. Misra, "Shape and contact force estimation of continuum manipulators using pseudo rigid body models," *Mechanism and Machine Theory*, vol. 139, pp. 34–45, 2019. [Online]. Available: https://www.sciencedirect.com/science/article/pii/S0094114X18318706